2017

1-D imaging cytometry: statistical assays for immunotherapy drug screening

BOSTON UNIVERSITY

COLLEGE OF ENGINEERING

Dissertation

1-D IMAGING CYTOMETRY:

STATISTICAL ASSAYS FOR IMMUNOTHERAPY DRUG SCREENING

by

STEVE S. WANG

B.S., Johns Hopkins University, 2010
M.S. Boston University, 2014

Submitted in partial fulfillment of the

requirements for the degree of

Doctor of Philosophy

2017

Approved by

First Reader _____

Daniel J. Ehrlich, Ph.D.
Research Professor of Biomedical Engineering

Second Reader _____

Wilson W. Wong, Ph.D.
Assistant Professor of Biomedical Engineering

Third Reader _____

Darren Roblyer, Ph.D.
Assistant Professor of Biomedical Engineering

Fourth Reader _____

Adrian Whitty, Ph.D.
Associate Professor of Chemistry

Fifth Reader _____

Sandor Vajda, Ph.D.
Professor of Biomedical Engineering
Professor of Systems Engineering
Professor of Chemistry

ACKNOWLEDGMENTS

I would like to thank my advisor, Dr. Daniel Ehrlich, for his immense patience over the past 7 years and his generous guidance throughout the entirely of my PhD candidacy. I would also like to thank the members of my committee, who have all helped me in many ways, both academic and personal: Dr. Wilson Wong, who has given me countless ideas and insights on T cell biology and immunology; Dr. Darren Roblyer, with his great support and joining my committee last minute; Dr. Sandor Vajda, who has provided me with great many conversations about random topics in the hallway; Dr. Adrian Whitty, who has provided solid feedback and helped me think about my research in entirely different ways. I also cannot thank enough the two previous members of our research group, Man Ching Chueng and Brian McKenna. They inspired many of the ideas and motivations for my current thesis direction and were essential to development of the programming behind all of the data analysis.

I also cannot thank enough all my colleagues and peers that I have encountered and befriended in the BU BME department. They have all been essential to my time here, through enlightening conversations about science and many mindless walks to Pavement for that totally-not-addicted-I-swear cup of coffee. I can try to list them all but it is a countless list: Yasha Sharma, Ali Badreddine, Tony Gao, Erika Fong, Athena Shiremeni, Christine Yueh, Bing Xia, Nga Ho, Bobby Liu, Chentain Zhang, Arthur Sun, and Andrea Fernandes are a few off the top of my head in no particular order.

Finally, I have to thank everyone in the BU administration that have made my PhD possible. Without them, I would not have graduated at all. Christen, who has been impeccable with her handling of paperwork and patience every time I forgot to submit my funding contract. Fallon, for being the most efficient and reliable human being I've ever met. And last but not least, Matt Barber, for his endless support, thank you.

1-D IMAGING CYTOMETRY:

STATISTICAL ASSAYS FOR IMMUNOTHERAPY DRUG SCREENING

STEVE S. WANG

Boston University, College of Engineering, 2017

Major Professor: Daniel J. Ehrlich, Ph.D., Research Professor of Biomedical Engineering

ABSTRACT

Modern cancer immunotherapy involves the conditioning of endogenous T cells to fight cancerous bodies that have managed to resist or avoid detection. Recently approved antibody drugs target the immune checkpoint pathway in T cells to prevent their tolerance to cancer antigens. There exists a compelling need, especially in the drug discovery world, to develop better assays for screening and to study the underlying mechanisms of these new antibody drugs.

The core motivation of my work is to develop a primary cell assay for the immune checkpoint pathway using 1-D imaging cytometry. The assay is focused on high throughput and high content screening. It takes advantage of our novel 1-D imaging cytometer platform. The assay is designed to artificially induce anergy in primary human T cells and systemically study their drug response. An automated statistical method quantifies the functional phenotypes of both healthy and anergic T cells into a single descriptive readout. Reducing localization of biomarkers into a single 'activity score' readout has many advantages for drug screening and characterization. Additional assays were developed to study T cell activation

dynamics and other signaling events during the immune checkpoint pathway.

Our 1-D instrument leverages both the high throughput aspects of traditional flow cytometry and the high spatial content of 2-D imaging cytometers. The PMC data analysis emphasizes an unbiased approach to analyze flow cytometry data, which eliminates the subjective manual gating of current cytometric methods. This is crucial to developing more accurate and reliable assays with minimal supervision and need for expert operators. The high-throughput and high-content capabilities presented enable new types of assays previously not possible with human primary T cells. Adoption of physiological relevant primary cell assays has potential to revolutionize large-scale drug screening and future applications in personalized medicine.

TABLE OF CONTENTS

LIST OF FIGURES

LIST OF ABBREVIATIONS

1-D One dimensional

2-D Two dimensional

ADC Analog-to-digital converter

CDF Cumulative distribution function

FACS Fluorescence activated cell sorter

FBS Fetal bovine serum

FCM Flow cytometry microscopy

HCA High content analysis

HCS High content screening

KS Kolmogorov-Smirnov statistic

NFAT Nuclear factor of activated T cells

PBMC Peripheral blood mononuclear cell

PBS Phosphate buffered solution

PD-1 Programmed death receptor

PI Propidium iodide

PMC Parallel microfluidic cytometer

PMT Photon multiplier tube

SD Standard deviation

SNR Signal-to-noise ratio

TCR T cell receptor

TNF Tumor necrosis factor

Chapter 1 - Introduction

1.1 Problem statement

Cancer immunotherapy is one of the fastest-growing areas in cancer research. Much of the recent drug development has been focused specifically on the immune checkpoint pathway (Intlekofer & Thompson 2013; Marincola et al. 2003; Prieto et al. 2012; Robert et al. 2014). Therefore, there exists a need to develop more specific and efficient screening assays to study drug interactions on this pathway. High content assays are well suited for studying the immune checkpoint pathway as they provide intracellular information even with relatively small T cells (Starkuviene & Pepperkok 2007; Zanella et al. 2010; Singh et al. 2014). High throughput is needed in addition to high content to provide the statistical strength that is required for drug discovery screening. Statistical significance and automation becomes even more important when dealing with primary cells with high biological variance (Eglen & Reisine 2011).

The current technologies to study T cells have traditionally been limited to single-stream non-imaging flow cytometers. Traditional flow cytometers are unparalleled in cell throughput. Most modern flow cytometers can measure thousands of cells per second with up to 32 separate colors per cell (Edwards & Sklar 2015). However, these measurements do not yield any spatial information for their corresponding biomarkers. They also traditionally have low well throughput. Similar to non-imaging flow cytometers, the 2-D imaging approach has its own limitations with regards to throughput and cell type. Plate readers can only image

single wells one at a time which limits sample-to-sample turnover. At high magnifications, images may contain low cell counts that limit statistical power. Most 2-D imaging cytometers are strictly limited to adherent cells, and the one commercial 2-D imaging cytometer has very limited well throughput (Millipore 2017).

1.1.1 Hypothesis

As a result of the limitations of traditional flow and 2-D imaging cytometry, we chose to develop high content imaging in flow. Our main objective is to develop a new type of 1-D imaging methodology that is optimized for the study of antibody therapeutics.

The goal of this work is to design and optimize the parallel microfluidic 1-D cytometer (PMC) platform. We argue that this new approach is highly suited for studying dynamic T cell pathways at high throughput in flow. Its particular strength is quantitatively higher well throughput than has been previously possible for flow imaging. These advantages stem from parallel fluidics and statistical data analysis. We use statistical thresholding and regression modeling to build an automated pipeline that streamlines the entire process of data reduction.

The secondary goal of this work is to use the new 1-D imaging system to develop a novel assay to probe drug response in immuno-compromised T cells. Immune checkpoint drugs reverse and prevent tolerance of a patient's endogenous T cells against existing cancer antigens. To study the efficacy of these drugs, one

needs an assay that can probe compromised T cells in a systematic way. In addition, using primary human T cells increases the physiological relevance in measuring the drug response. Primary human T cells are rarely used in drug screening applications because of the many research challenges they pose, the least of which, is that most assays consume large volumes of cell sample, rendering them impractical for primary human cells. Our application has the advantage of requiring minimal volumes and cell numbers, allowing thousands of conditions to be probed from a single clinical sample.

1.2 Aims

1.2.1 Aim 1 - Optimize PMC instrumentation

The parallel microfluidic cytometer (PMC) collects 1-D fluorescence images from individual cells at high speeds. The main purpose of this aim was to advance the engineering development of this instrument design. This requires optimization of the optical/electronic components and high throughput sample collection. The current PMC design uses a galvanometer to scan a focused laser. It provides high imaging speeds but at the same time has many trade-offs with regards to spectral overlap, signal to noise, sensitivity, and unwanted variance across lanes. The microfluidics and operating protocols were optimized for better throughput and reproducibility.

1.2.2 Aim 2 - Design statistical framework for 1-D image analysis

High content screening (HCS) involves measuring large numbers of cell images and converting them into a simple readout. Correlating 1-D images from our optical system to their 2-D analogues was one of the goals of this work. Validation with traditional 2-D microscopy was used to confirm drug responses. One of the biggest challenges in HCS is the large amount of data that is generated from each cell. The main goal of this aim was to develop an automated streamlined statistical workflow to reduce multi-dimensional imaging data into a single drug response activity score by means of regression modeling. The single readout score is a reduced measure of how well a drug performs. Finally, it is important to have high sensitivity for any assay, so much of the work was maintaining high separation between positive and negative controls.

1.2.3 Aim 3 – Develop immunotherapy assay based on functional T cell response

The last aim was to develop an assay to measure the anergy and recovery of primary human T cells. The general approach involved inducing an anergic state in purified human T cells and then adding various drug candidates to measure the resulting response. Drugs that are successful in preventing or recovering cells from anergy should return the cells to a more responsive state. We decided to use T cell activation and nuclear translocation of NFAT to measure this functional state. Before the final assay was constructed in full, many of the individual components of the assay were tested first in a cell line.

Although there are other ways to measure anergy (such as surface markers or cytokines), measuring the functional state of internal signaling pathways is more useful in studying the exact mechanisms of action. Immune checkpoint blockade drugs inhibit many signaling pathways related to T cell activation. In addition, drugs can have unwanted or nonspecific effects that can affect multiple signaling networks within a cell.

Many of our methods are adapted from 2-D HCS, so we conducted additional validation assays to compare our approach with existing HCS. Dose response, drug inhibition, and kinetic curves were generated. Also, we show the high throughput capabilities of our technology by scaling up to a 96-well plate.

1.3 Structure of thesis

In summary, this work involves development of a platform to study the mechanisms and efficacy of T cell immunotherapy. Chapter 2 introduces all the relevant background information regarding current flow cytometry approaches, T cell signaling pathways, and current immunotherapy approaches. Chapter 3 introduces the full design of the PMC. It covers the development of the instrumentation and fabrication methods for the PMC hardware. Testing and validation are shown in appropriate sections. Chapter 4 presents the full statistical pipeline and its development. Chapter 5 presents the anergy assay and the preliminary steps building up to the final design. Multiple translocation pathways were tested in a

Jurkat cell line. Chapter 6 concludes the major findings of the work and discusses future directions.

Chapter 2 - Background

2.1 Flow cytometry

2.1.1 Traditional flow cytometry

Flow cytometry (FCM) has been used for decades in the measurement of surface and intracellular antigens (Shapiro 2003). Qualitative and quantitative differences are measured to characterize cellular function and differentiation. Applications include, but are not limited to, immuno-phenotyping, cell sorting, rare cell detection, small particle analysis, signaling pathway analysis, kinetics, and DNA/RNA measurement (Shapiro 2003). Some of the most common commercial systems are the BD Accuri, BD LSRFortessa, BD FACSAria, Miltenyi MACSQuant, Thermo Fisher Attune. Cell sorting is also available in many flow cytometer instruments, and is based primarily on charge droplet or magnetic droplet separation (Richardson et al. 2015). This is a relatively simple task in single stream flow cytometers, as the stream can be diverted when a specified fluorescence threshold is detected.

A classical flow cytometer involves a single cell suspension flow channel, which is illuminated by a fixed laser. Emitted fluorescence is collected via an optical path that filters out unwanted laser wavelengths, while preserving the relevant emission wavelengths. Photomultiplier tubes (PMTs) are usually used to collect the emitted fluorescence. A simplified diagram is shown in Figure 2-1.

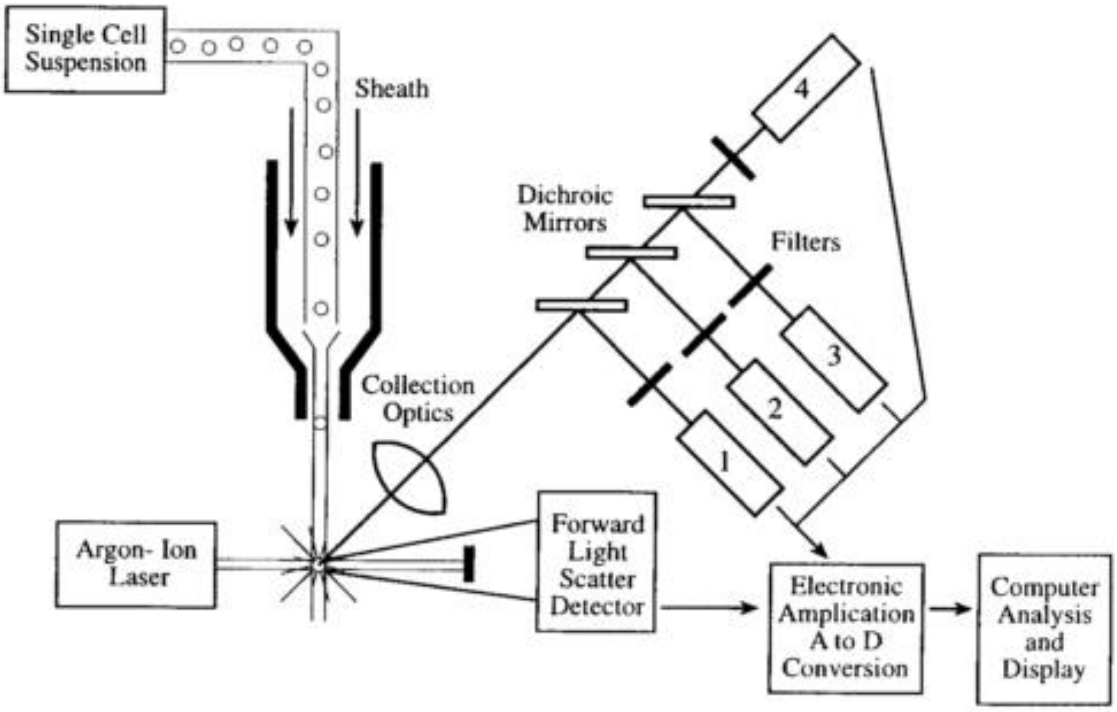

Figure 2-1. Diagram of single stream flow cytometer.

A single stream cell suspension is brought into contact with a fixed laser, typically an Argon-Ion laser. The labeled cells are excited and emitted fluorescence is collected by a series of photodiodes (scattering) and photomultiplier tubes (PMTs). Dichroic mirrors serve as bandpass filters to isolate each color into its corresponding PMT. Collection optics are varied but typically involve telescoping and objective lenses to focus the emission path onto the PMT cathodes. Image taken from (Brown & Wittwer 2000).

The setup of a traditional single stream flow cytometer is highly serialized yet extremely efficient at analyzing single cell suspensions. A typical system is capable of analyzing cells at speeds of 10,000 cells/s with low coefficient-of-variance (CV) and high sensitivity. Single cell suspensions are hydrodynamically focused with sheath fluid for accurate alignment with the excitation laser beam. The cytometer in Figure 2-1 has 4 color channels (one for each PMT) and a single argon-ion laser.

However, many commercial cytometers have multiple lasers and up to 32 color channels.

Flow cytometers are typically limited to suspension cells. Although adherent cells can be detached from growth vessels or de-aggregated, there is a penalty that the detachment process can cleave surface proteins and affect internal biology. FCM is unparalleled in its cell throughput, but in turn, is limited in sample throughput. A single stream input requires samples to be scanned one at a time, so the sample throughput is limited by how fast the loading apparatus can be cycled. Some companies have attempted to overcome this limitation by using a pulsatile pump to deliver an 'air gap delimited stream' (Intellicyt iQue Screener Plus) with a fast robotic handler. This particular system claims a sampling throughput of 96 wells in 5 min.

One of the fundamental limitations to FCM is that the laser spot is designed to be much larger than a cell, thereby foregoing intracellular information. Each cell is labeled with multiple fluorescent labels, which can produce up to 32 separate data points per cell. However, each fluorescent data point is an indication of the summed fluorescent coming from the cell. This can be regarded as a zero-dimensional (0-D) image/point. Cell assays are designed accordingly to this spatial limitation. There is another practical constraint, particularly if too many fluorescent labels are used. Crosstalk and interference can result from spectral overlap of fluorophore emission profiles (Roederer 2001). Compensation and spectral demixing is a required step in many protocols.

For data analysis, histograms and scatter plots are used to differentiate individual populations and quantify changes. A highly trained operator will gate populations by manually drawing boundaries around the relevant populations. An example of this process is shown in Figure 2-2.

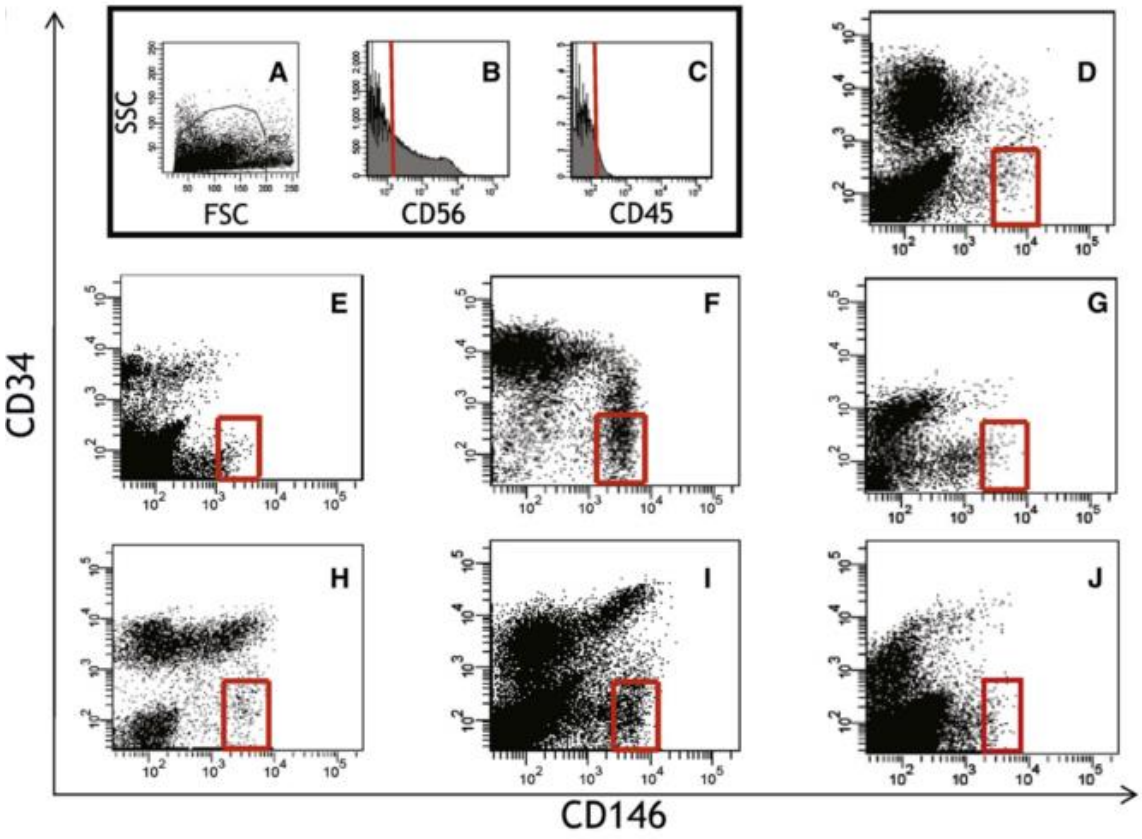

Figure 2-2. Example of flow cytometry panel: scatter plots for differentiating perivascular cell populations.

An example of the typical scattering plot approach for gating subpopulations to differentiate cells. Cells are labeled with two separate surface markers and plotted against one another. Populations are gated (indicated with red boxes) by manually drawing thresholds around cells using expert operators. (Crisan et al. 2008)

An important aspect of this gating process is the use of manually drawn boundaries. Automated data clustering algorithms do exist but they are not reliable or practical

(Abraham et al. 2014). To fully separate subpopulations usually requires three standard deviations (SD) of separation for reliable analysis. If the subpopulations are noisy or too closely overlapping, an operator must make a qualitative and subjective judgement to determine the correct gating boundaries. For complete and unbiased gating, each subpopulation must have an identifying subset of surface markers and/or must be as dissimilar from each other to make a determination.

2.1.2 Imaging cytometry

Another approach, that adds 2-D intracellular marker localization, is termed imaging cytometry. Compared to FCM, the underlying concept is the same, however, instead of a single stream flow channel, most imaging cytometers use microtiter plates and CCD cameras or laser scanning microscopes to image the cells. Imaging cytometry that is related to drug discovery and high throughput methods is called high-content analysis (HCA) (Freeley et al. 2010). Similar to FCM, HCA uses a wide range of fluorescence excitation and emission detectors for multiplexed cytometry. Common imaging cytometers on the market include BioTek Cytation, Thermo Fisher ArrayScan, and the PerkinElmer Operetta. The instrumentation varies across imaging platforms. One of the greatest advantages of HCA is that 2-D images can provide information on the intracellular localization of biomarkers. Assays include signaling transduction pathways, co-localization, cell-cell interactions, live cell kinetics, morphology/cytoskeleton tracking, spot counting, and many more (Singh et al. 2014).

Most HCA systems are confined to use with adherent cell cultures. Although not completely impossible, in practice, suspension cells floating in wells are nearly incompatible with a fixed focal plane imaging system. Well throughput of HCA systems is also limited. Throughput depends on multiple factors such seeding density of the cells and robotic systems. The cell and sample throughput are typically much slower than FCM, but can be improved with robotic handling and automated systems. Many modern HCA systems can analyze a 96-well plate in 5–10 min. High NA objectives and magnifications are often used and adjusted for diffraction limited imaging for submicron resolution. Due to the complex autofocusing and robotic handling, HCA contains additional imaging artifacts that are not present in FCM. Artifacts such as high background noise from improper washing, cell debris, overlapping cells, overexposure, and inconsistent illumination are common. (Bray et al. 2012; Bray & Carpenter 2004). Temporal artifacts and edge effects are also problems, as wells are imaged serially.

2-D images allow for statistical study of spatial and temporal processes within cell populations (Shariff et al. 2010). Images are first "segmented" to isolate each cellular compartment from the image of the full well. Features, mathematical constructs used to analyze cell images, are calculated from each cell. HCA maximizes information content by measuring hundreds to thousands of features for each labeled biomarker. These features are quantitative measures of cellular features ranging from texture, area, perimeter, morphology, frequency coefficients, cell-cell adjacency, and more (Singh et al. 2014). Thousands of features can be generated

from each cell and a typical well may contain hundreds of cells. Thus, HCA is naturally suited for statistical algorithms as a means to process the data. Phenotypic changes can involve very subtle changes. Without the separate identifiable tags for each marker, algorithms are used to determine the most statistically significant features for population discrimination. These include algorithms adapted from the world of machine learning, classifiers, supervised/unsupervised learning, clustering, and regression modeling to select the most important features (Kozak et al. 2009; Kümmel et al. 2011). For screening applications, a list of a thousand features can be reduced to a single feature depending on the assay. Overall, the general approach of HCA is to reduce highly-dimensional data sets into easily interpretable readouts.

2.1.3 Combination cytometry (imaging & flow)

Due to the success of FCM in the areas of immunology, there has been a recent resurgence in the development of imaging methods that incorporate flow. Imaging flow cytometry (IFC) has the advantage of high content spatial resolution of 2-D imaging. Some current imaging flow instruments include the EMD Millipore ImageStream®X Mark II (Zuba-Surma et al. 2007), multi-field-of-view IFC (Schonbrun et al. 2012), temporal coded excitation (Gorthi et al. 2013), STEAM (Goda et al. 2009), FIRE (Diebold et al. 2013), and others (Han et al. 2016).

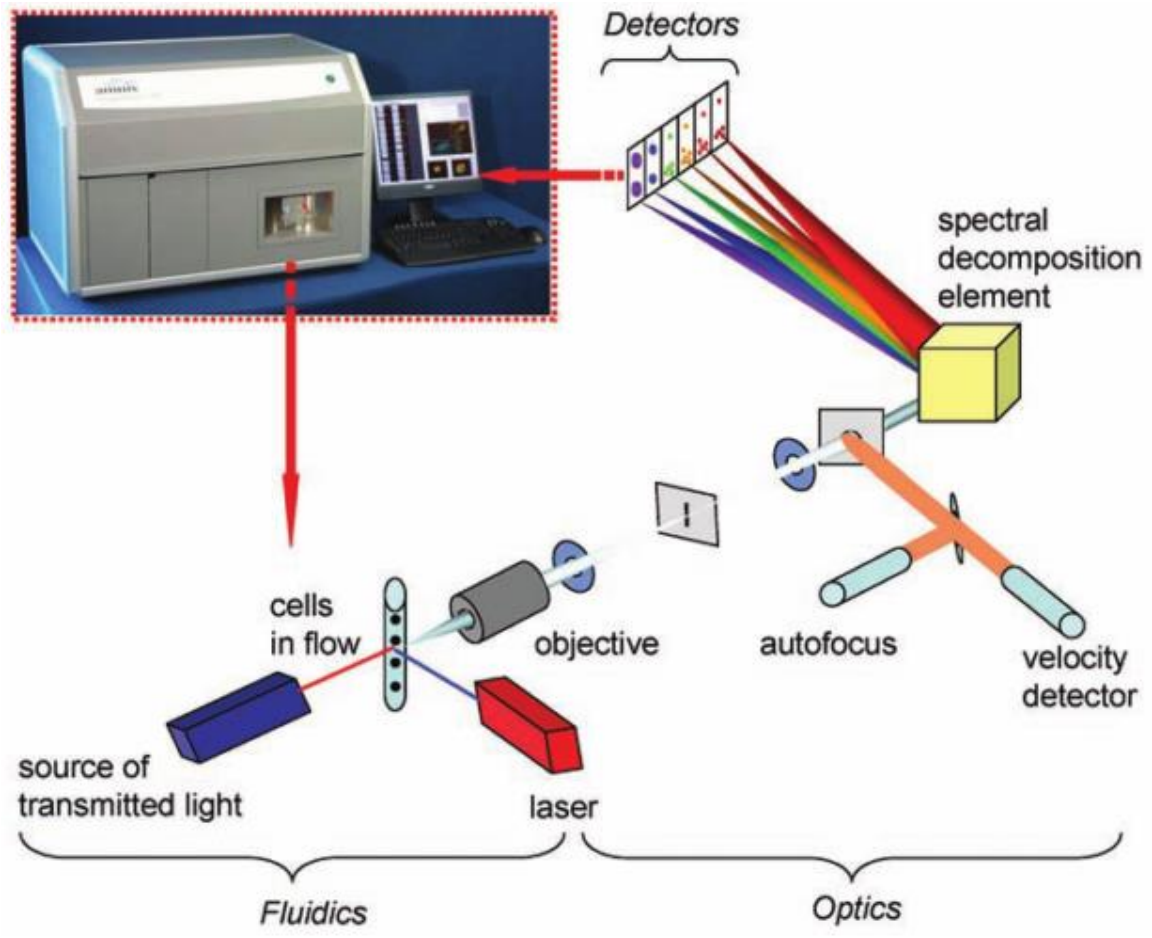

Figure 2-3. Diagram of ImageStream®X imaging cytometer.

One of the only commercial available imaging flow cytometers on the market. A synchronized optical integrator combined with a spectral dichroic filter stack projected onto a CCD array allows 2-D imaging in flow. Image taken from (Zuba-Surma et al. 2007).

Only the first instrument (EMD Millipore ImageStream®X Mark II) is currently commercially available (Figure 2-3). It uses a sensitive time-delay integrator that applies synchronized imaging of cells in a single stream flow channel. The images obtained from the ImageStream®X are high resolution but its throughput is limited by its strict flow stability requirements, CCD detector speed, and serial operation.

Since cells are in flow, as opposed to static conditions in 2-D imaging wells, there is a fundamental limitation in acquisition time, noise, and sensitivity. Many of the previous technologies attempt to solve this issue in different ways. For example, one method, STEAM, converts spectral information into the time domain to achieve higher sensitivity with extreme speeds. Another method FIRE uses radio frequency waves to modulate the light excitation for simultaneously fluorescence imaging.

Despite these improvements in imaging flow cytometry (IFC), there is still a fundamental bottleneck with the data analysis (Giuliano et al. 2003). Similar to HCA, imaging in flow generates an enormous amount of data per cell. The challenges of acquiring, storing, processing massive numbers of cell images is a persistent problem in IFC. However, the silver lining for IFC is that some imaging difficulties with 2-D HCA can be avoided in flow. Segmentation algorithms such as threshold, watershed and edge detection are computationally expensive but is completely unnecessary in flow.

2.1.4 Microfluidic cytometry

The field of microfluidics is readily compatible with the concepts of cytometry, as both aim to manipulate small particles in single or multi stream pathways for imaging analysis (Godin et al. 2008). One of the biggest advantages of microfluidic devices is the ease of adding additional functionality into a compact device. Switches and sorting modalities can easily be introduced. Most commonly, laminar flow is present, with low Reynolds numbers. Microfabrication is highly scalable; devices

made in polydimethylsiloxane (PDMS) or plastic can be reproduced quickly and cheaply. Figure 2-4 presents some current prototypes of cytometry devices that have been built as microfluidics. One of the biggest advantages of microfluidics is that new lane geometries can be exploited, such as parallel flow. However, imaging in flow with microfluidics has many challenges. Surfaces can present scattering and reflection losses. Detection of weak fluorophores and scattering is difficult in these devices, due to typically higher backgrounds.

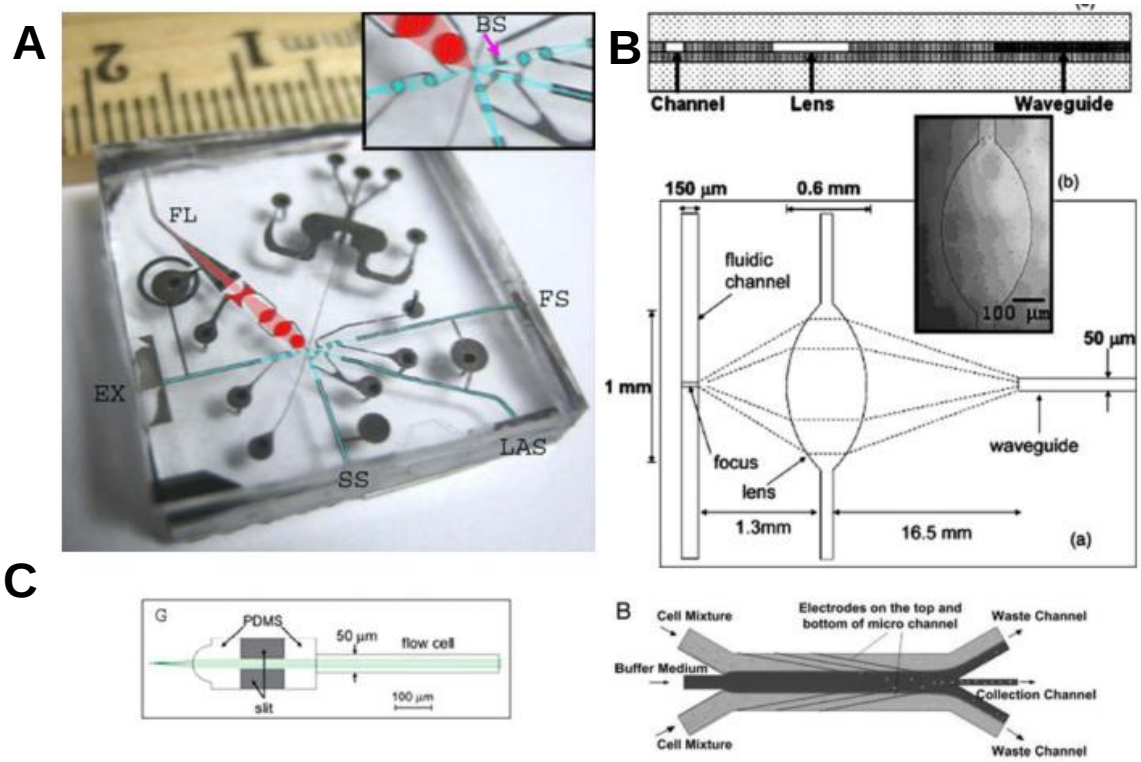

Figure 2-4. Examples of microfluidic technologies used for cytometry.

A) Fully integrated cytometer into a single fluidic chip. Optical wave guides and pump inlets and outlets are multiplexed into a compact system. B) Examples of optical wave guides to focus laser paths into small fluidic channels. C) Example of flow geometries for hydrodynamic focusing and buffer systems. Images taken from (Godin et al. 2008).

2.2 T cell immunology

2.2.1 Introduction

T cells are lymphocytes that mature mainly in the thymus. They compose a large part of the adaptive immune system and include cytotoxic CD8 cells, helper CD4 cells, memory and regulatory T cells (Yamanaka et al. 2013). The main difference is that helper T cells bind to MHC II (related to extracellular pathogens) and cytotoxic T cells bind to MHC I (related to intracellular pathogens/damage). Binding of the MHC complex from antigen presenting cells to the T cell receptor (TCR) triggers an activation cascade that eventually leads to clonal proliferation/recruitment of B cells and macrophages. This eventually results in the creation of antigen specific antibodies and subsequent release of cytokines to destroy foreign or self-antigens. Self-antigen recognition is particularly important to prevent auto-immune diseases and cancer (Anderson et al. 1999).

2.2.2 T cell activation

When a naïve T cell encounters an antigen presenting cell (APC), the TCR binds to the corresponding antigenic epitope and MHC complex (Smith-Garvin 2009). Each TCR has a highly variable region which is specific to one ligand. The TCR will then communicate with a CD3 complex that becomes non-covalently bonded to the TCR. The TCR is then referred to as the TCR:CD3 complex. The CD3 receptor contains an immuno-receptor tyrosine-based activation motif (ITAM) region on its cytoplasmic tail. In vitro, it is possible to bypass the requirement of TCR ligation and directly

bind to the CD3 component to simulate MHC interaction. Costimulatory receptors, such as CD28, can enhance the activation response (Figure 2-5). Directly following litigation of the TCR complex, the remaining TCR complexes on the cell surface will begin to aggregate and localize in a super cluster, a phenomenon known as capping (Kammer et al. 1983; Schreiner & Unanue 2011). The aggregation of TCR complexes is a rapid event that begins seconds after binding of the TCR. Maximal capping, where more than half the cells receptors are aggregated, occurs in around 10–15 min (Kammer et al. 1983).

After the immunological synapse is established, various signaling pathways are triggered as shown in Figure 2-6 (Ilani et al. 2007). Protein tyrosine kinases (PTK), Lck and Fyn are activated by CD4/CD8, CD28 and CD45. These help phosphorylate ITAM on CD3. This leads to recruitment of ZAP-70 and further signaling cascades. PLCγ and DAG dependent pathways are activated. These result in the activation of two major pathways, Ras and PKCϴ, which are involved in the translocation of transcription factors including Extracellular Signal Regulated Kinase (ERK), c-Jun N-terminal Kinase (JNK), Nuclear Factor-KappaB (NF-kB) and Nuclear Factor of Activated T-Cells (NFAT).

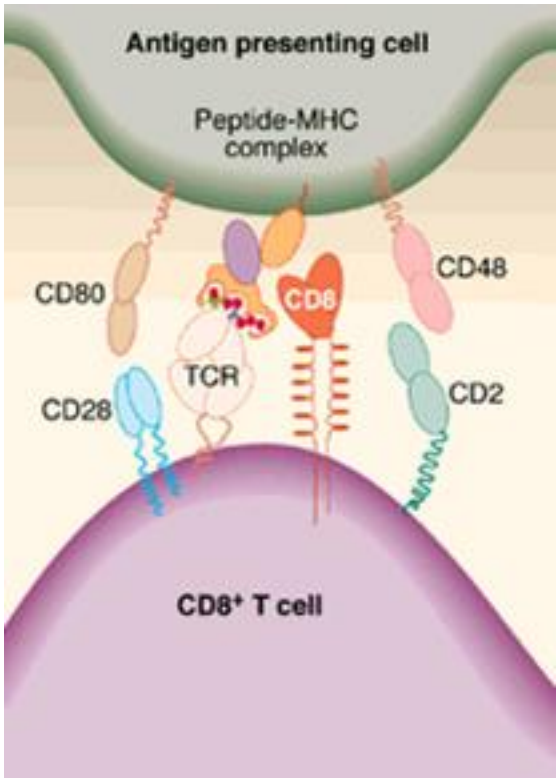

Figure 2-5. Immune synapse of a CD8+ T cell.

Surface receptor organization during T cell activation and ligation. TCR is the main receptor that recognizes MHC complexes on antigen-presenting cells. CD28/CD8/CD2 are co-stimulatory receptors that enhance the immune response. Image taken from (https://med.nyu.edu/skirball-lab/stokeslab/tcell.html).

2.2.3 NF-kB/NFAT translocation

The transcription factors NF-kB and NFAT are both critical components in T cell proliferation (Srivastava et al. 2010; Baine et al. 2009). They both require significant translocation to the nuclear compartment to activate their corresponding genes. The NF-kB factor is bound to an IkB inhibitor at rest. After activation, IKK phosphorylates IkB which then allows the NF-kB to translocate into the nucleus and activate gene expression as a transcription factor. For NFAT translocation, after TCR

activation there is an increase in cytosolic Ca^{2+}. This activates calcineurin which then dephosphorylates pNFAT. An alternate method to trigger calcium release is with small molecules PMA and Ionomycin. This allows NFAT to translocate into the nucleus and form complexes with other transcription factors. The destination for many of these pathways is increased secretion of IL-2, IL-2 receptors (CD25), CD69 (cell surface proliferation glycoproteins) and eventually proliferation. These two pathways are notable, and useful for cellular imaging assays since they involve spatial localization of a biomarker.

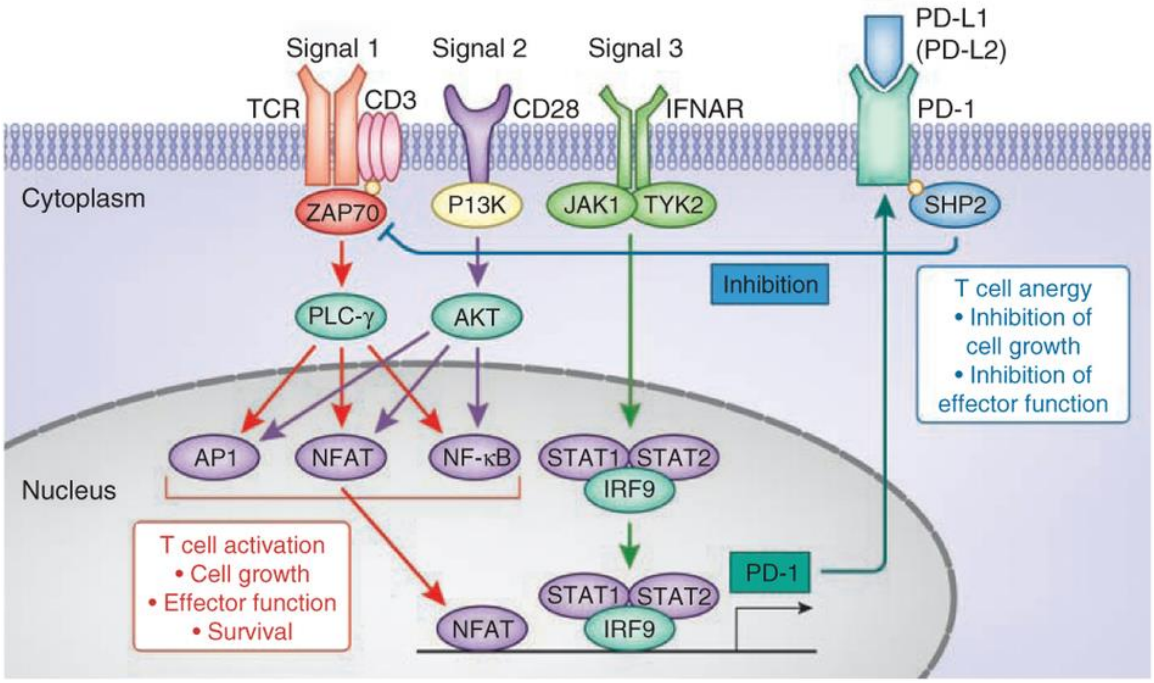

Figure 2-6. Signaling transduction network of T cell activation.

Left hand side shows the normal activation pathway and translocation of relevant transcription factors. The immune checkpoint pathway is displayed on the right. Binding of PD-1 triggers a cascade that results in T cell inhibition, tolerance and anergy. Image taken from (Okazaki et al. 2013).

2.2.4 Immune checkpoint blockade

Cytotoxic T-lymphocyte-associated protein 4 (CTLA-4) and programmed cell death protein 1 (PD-1) are receptors involved in the T cell checkpoint blockade pathway (Parry et al. 2005). These receptors appear much later and peak around 24–48 hours after initial activation (Nirschl & Drake 2013). Both receptors contribute to help regulate self-tolerance and autoimmunity (Intlekofer & Thompson 2013). In this work, we focus solely on the PD-1 pathway for multiple reasons. It has been discovered that many cancer types have shown to express large amounts of PD-L1 to avoid detection by the immune system (Iwai et al. 2002; Andorsky et al. 2011). PD-1 targeting drugs have also shown less side effects than CTLA-4 targeting drugs in clinical trials (Hamid et al. 2013). Both Keytruda (Powles et al. 2014) and Opdivo (Robert et al. 2014) are PD-1 antagonistic antibody drugs (also known as immune checkpoint blockade) that have been recently approved by the FDA. They have shown great potential for use in melanoma treatment and are underlying phase III clinical trials.

When PD-L1 (PD-L1 is the ligand to PD-1, also known as B7-H1) binds to PD-1, SHP2 is recruited and dephosphorylates PI3K (Hapter et al. 2003). This inhibits AKT activation, as well as ZAP70, PLCγ, and CD3 related events, all of which are crucial in T cell activation and proliferation. Both NFAT and NF-kB translocation occur downstream of those signaling events. Therefore, it is safe to assume that both NFAT and NF-kB translocation will be compromised as a result of PD-1 activation. A summary of the PD-1 pathway is shown in Figure 2-6. Immune checkpoint blockade

drugs (ex. Keytruda, Opdivo) are proposed to work by blocking the binding of PD-1 ligands to PD-1 receptors, thereby preventing immune tolerance.

2.3 Cell models

2.3.1 Jurkat

Jurkat (E6.1 clone) is an immortalized lymphoblastic cell line that was extracted from an acute T cell leukemia patient (Abraham & Weiss 2004). Jurkat cells are known for their ability to produce IL-2 after TCR activation. Jurkats have been used extensively to characterize the events involved in TCR signaling pathway, therefore we chose them for the T cell activation studies in this work (Abraham & Weiss 2004). However, there are several limitations of Jurkats. They have large nuclei which makes it difficult to differentiate between cytoplasmic and nuclear compartments. Also, Jurkats are immature lymphoblasts which lack CD4 and CD8 expression. Jurkats also have abnormal PTEN and SHIP phosphatases, the effect on activation is still unknown (Abraham & Weiss 2004). Jurkats are immortal cell lines so they cannot be stopped from proliferating or entering anergy (our results confirm that attempting to stop the cell cycle or activating the PD-1 pathway results in apoptosis). Despite the downsides, Jurkats are useful due to their TCR kinetics, homogeneity, and ease of culture *in vitro*.

2.3.2 Primary cells

Clinical trials are the required standard for drug testing. Obviously due to practical and safety reasons, experimental drugs such as immune checkpoint blockade cannot be tested at early stages, *in vivo*, in humans. Before clinical trials can be conducted, specialized cell lines or animal models are typically used to test and screen for drugs (Hughes et al. 2011). Since most drugs being developed have human targets, maintaining physiological relevance is an important factor when choosing a model. Most of our assays are initially tested in Jurkat cells for the practical reasons above, but transitioning into primary cells is the end goal, as it will allow for better prediction of true immune responses.

Primary cells obtained from peripheral mononuclear cells (PBMCs) from patients have high physiological relevance but also many difficulties in assays (Longo et al. 2012). For example, assays that involve reporter genes can be difficult in primary cells (X. Huang et al. 2017). Transfection using viral methods can cause unwanted immune responses. Also, there is a huge amount of heterogeneity and biological variance between patient PBMC samples. Primary cells obtained from human donors cannot be fully characterized down to every single genomic mutation or alteration. There is always the danger of working with contaminated cell populations, but antibiotics can reduce the risk.

Using primary cells for drug studies has many potential benefits (Eglen & Reisine 2011). Some drugs are only effective on certain people with specific genetic

defects. For example, Keytruda (Pembrolizumab, anti-PD-1 blockade drug developed by Merck) has been shown to be extra effective on patients with the mismatch repair genetic defect (Skora et al. 2015). Pre-screening is a natural step for many clinical trials and personalized medicine to determine individual drug response (Robert et al. 2014). Weekly or monthly check-ups using cytometric analysis on blood samples is common during clinical trials (Red blood cell count, white blood cell count, leukemia panels, CD4/CD8 expression). The methods that will be presented in this work can be easily adapted into existing clinical trial methods. It has been discovered recently that certain tumor states can be reflected in peripheral T cells (Ki67) (A. C. Huang et al. 2017). Although, used sparsely because of practical difficulties, primary peripheral immune cells can provide multiple advantages in both clinical and drug discovery applications.

Chapter 3 – Aim 1 – PMC Instrumentation

3.1 Overview

The PMC is a single axis confocal scanning laser microscope that obtains 1-D fluorescence scans of cells (Cheung et al. 2015; McKenna et al. 2011; Mckenna et al. 2009). The system combines the high cell throughput of flow cytometry with the intracellular localization of imaging cytometry, and the parallelism of microfluidics. The philosophy behind this instrument is to re-allocate detection bandwidth, by compromising on image dimensionality and resolution, to obtain higher throughput for drug screening applications. It has been shown previously that the information stored in low-pixel-count 1-D images is sufficient to differentiate between cellular phenotypes such as nuclear accumulation of NF-kB in Chinese hamster ovary (CHO) cells and many other validated assays (McKenna et al. 2011). The parallel flow geometry allows much higher sample throughput, the current microfluidic uses 16 parallel fluidic lanes. The random sampling of the PMC provides high statistical power even with low hit rates.

3.1.1 Design

The instrument we designed is based on a scanning laser detector with a traditional galvanometer scanner (Cambridge Technology H6240H). Figure 3-1 provides an overall diagram of the PMC system.

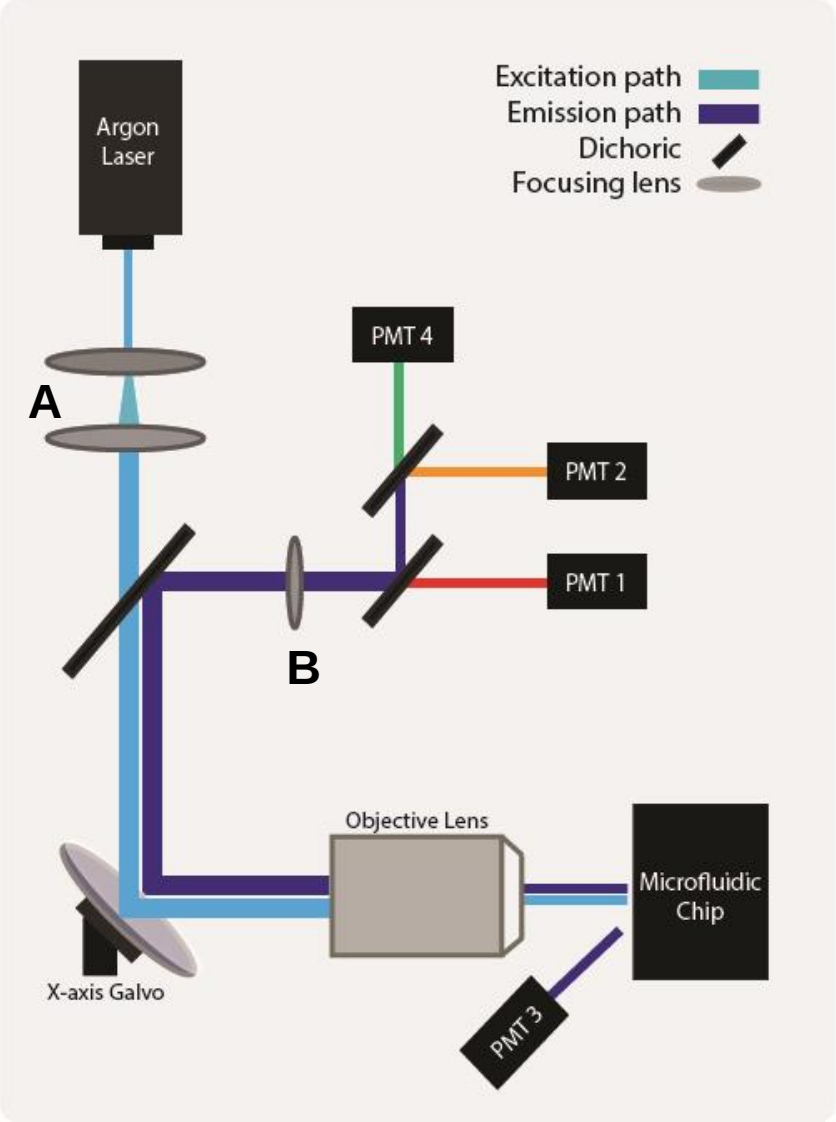

Figure 3-1. Diagram of PMC system.

The PMC resembles a typical confocal imaging setup but with one axis removed. A single argon-ion laser is used for excitation. Telescoping lens (A) and 50mm focal length objective focuses the laser to the parallel microfluidic chip. The galvo scans in a single axis across parallel fluidic lanes in the chip. Emitted fluorescence is collected into a PMT box with dichroic bandpass filters for each color. An optional pinhole (B) eliminates out of focus light. Image from (Wang & Ehrlich 2017).

A single-line 488-nm Argon ion laser is focused to a nominal 2-μm diameter spot through a 50-mm focal length, 0.35-numerical-aperture mesoscopic objective. Similar to a confocal microscope but with one axis removed, a galvanometer scans the laser across the parallel lanes of the microfluidic chip. The scanning frequency of the galvanometer mirror is 12.5 scans/s. 1-D images are acquired simultaneously on 1-4 photomultipliers (Hamamatsu H957-8) with one PMT reserved for scatter light. Images are digitized using a 14-bit analog-to-digital converter (ADC, Vertilon ISQP518, Vertilon Inc., Westfield, MA). The sampling rate is 60 kHz. Emission filters for each photomultiplier tube 660±25 nm (red channel), 570±10 nm (orange channel), 525±20 nm (green channel) and 488±5 nm (scatter detector).

The first prototype designed outside of this work used a rotating servomotor instead of the scanning galvanometer outlined in Figure 3-1 (McKenna et al. 2011). This first generation PMC system provided a proof-of-concept for 1-D imaging cytometry. The second generation system that was built for this work featured a scanning galvanometer and was fully integrated to include automated fluidics and robotic pipetting. A picture of this first iteration is provided in Figure 3-2 (right) and the full documentation in Appendix 1. Unfortunately, it was overly complicated to operate and unnecessary for low-throughput assay development. A second iteration (still using the scanning galvanometer) was built to accommodate easier workflow and faster customization. This was the primary system used for all the assays presented and an image is provided in Figure 3-2 (left).

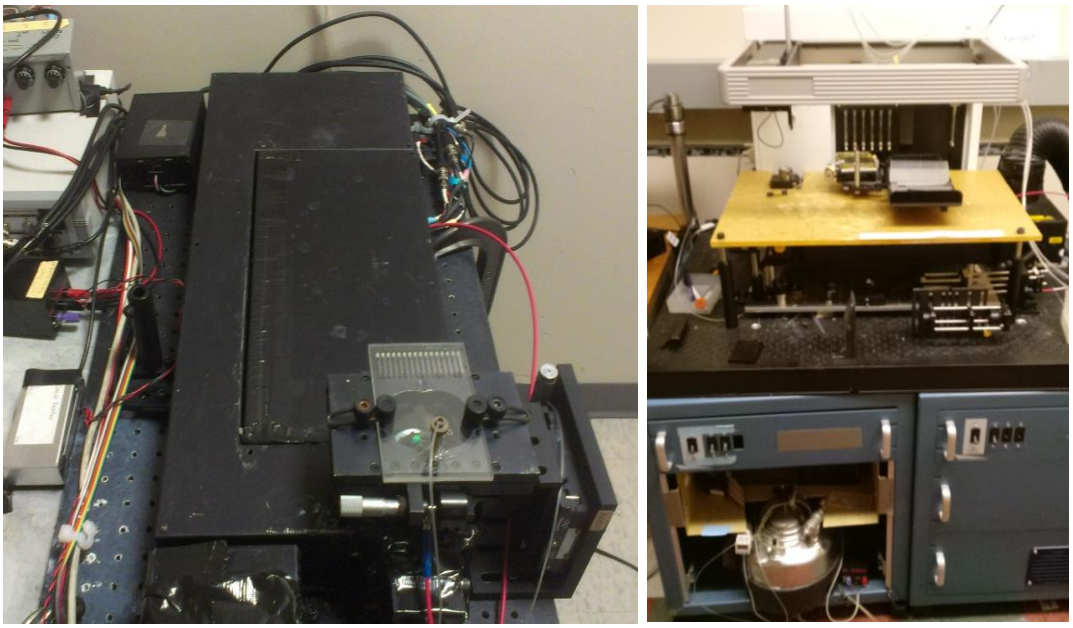

Figure 3-2. Real life images of 2nd generation PMC prototypes.

Left) Primary PMC system. The black metal casing protects the inteneral optics. The objective is directly underneath the microfluidic chip and scans from left to right across the parallal lanes. Power supplies and the ADC are connected externally along with a high processing computer to analyze the data collected. Right) Initial PMC build with fully automated fluidics and robotic pipettor. This first iteration was built to accomadate high throughput capablities and was designed as a complete integrated all-in-one system.

3.1.2 Comparisons to current cytometry approaches

The PMC obtains localization information of fluorescent markers in suspension cells as mentioned in Chapter 2.1.3. However, our instrument is unique in its use of 1-D imaging instead of more standard 2-D imaging. We chose this lower-pixel-count 1-D imaging approach in order to obtain higher sample throughput, particularly when combined with parallel microfluidics. For our assay development and needs, we built a system with 4 PMT color channels. Theoretically, the PMC system can be designed with the same multicolor multi-laser optical complexity as in traditional

FCM. In general, classical cytometers require highly trained operators to analyze the complex data sets (Kümmel et al. 2011). An important part of our work has been to create an automated workflow (Chapter 4) to eliminate subjective data reduction.

Overlapping and out-of-focus cells are common imaging artifacts in 2-D imaging assays. Cells can easily detach during pipetting and/or plate perturbations. Suspension cells are problematic since they float at variable heights in the wells. Centrifuging solves some of these issues, but is ultimately sensitive to vibrations or movement since suspension cells are non-adherent. Out-of-focus images are only partially addressed through power log-log slope (PLLS) histograms, and other post processing methods in classical 2-D cytometry (Bray et al. 2012). In contrast, the PMC uses a scanning confocal detector which has out-of-focus rejection built directly into the hardware and software. A pinhole, or equivalent software, is used to eliminate out of focus light. In software, this is done through thresholding and automated gating. Once the focus is calibrated, it is stable for an entire day. This avoids additional hysteresis or focusing errors from constant dynamic focusing.

Edge effects are another source of well-to-well artifacts in 2-D HCS. These can be minimized through complex plate models, reference plates, longer incubation times, or removing edge wells altogether (Bray et al. 2012). Equivalent effects exist in the PMC in the form of spatial non-uniformity across the fluidic lanes. This is managed through individual calibration of each flow lane and selecting careful controls. As for temporal drift effects, the PMC avoids them as all lanes are scanned simultaneously.

Image segmentation (boundary determination of cell compartments and cell-to-cell separation), is another well-known source of error during reduction of 2-D HCS data. Most segmentation algorithms assume even illumination, high contrast of cytoplasmic/nuclear boundaries, and physically non-overlapping cells (Shariff et al. 2010). For adherent cells that are touching or overlapping, more complicated algorithms are needed such as Voronoi segmentation. Even if everything is ideal, best-fit estimations, kernel filters, clustering, and/or predetermined masking are still needed to achieve optimal segmentation with some amount of noise injected nonetheless. The PMC requires no segmentation step since the nuclear compartment is indicated by a nuclear counterstain. We accept a full line-scan for each color channel and extract features without segmentation or boundary definition.

One of the biggest advantages of using 1-D imaging is that all the data analysis is intensity-normalized as opposed to classical flow cytometry. Our features are insensitive to any overall differences in fluorescence intensity or PMT gain. Normalized features are not dependent on overall intensity and are highly tolerant to variability in sample preparation and artifacts from staining, oversaturation, or contrast.

Data efficiency is an important aspect of 1-D imaging. For a typical 10 μm cell, our system only needs 20 pixels per color to extract all the necessary information at 1 μm resolution (McKenna et al. 2011). In comparison, a 2-D system at 0.5 μm resolution would require a minimum of 400 pixels for the same image. 1-D imaging

is at least an order of magnitude more data efficient than 2-D imaging. This is especially important to many users, who complain of the data storage requirements of 2-D HCA systems. Furthermore, data efficiency is an important aspect of real time data analysis and sorting applications enabled by our sparse 1-D imaging approach.

3.2 Instrumentation

This section will cover the various experiments that were conducted to improve on the instrumentation and hardware of our new cytometer.

3.2.1 Optics

It was determined empirically that 25 nm wide dichroic filters were the optimal balance between signal-to-noise (SNR) and spectral overlap with our relatively modest laser. Polyclonal secondary antibodies were essential to achieve maximum SNR and sensitivity. The main fluorophores used our assays were Alexa 488 and propidium iodide, which naturally have low spectral overlap (Figure 3-3). A third color was attempted but a sufficiently high enough quantum yield fluorophore was not found. CF594 was the closest one tested with an *ex/em* of 488nm/594nm, but the sensitivity was too low to be detected in the PMC.

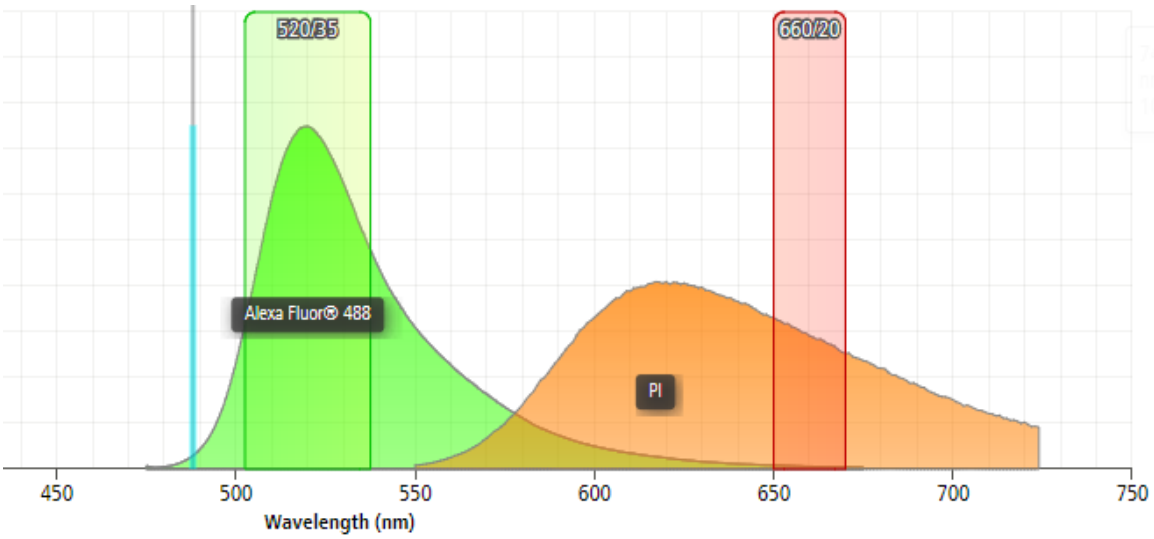

Figure 3-3. Graph of emission wavelengths in the PMC.

All fluorophores and excited by a 488nm Argon-Ion laser. Alexa 488 emits at around 530nm. The green shaded rectangle indicates the bandpass wavelengths for the dichroic emission filter for Alexa 488, around 520nm. The red shaded rectangle indicates the bandpass wavelengths for the emission filter for propidium iodide (PI). Since PI has a much broader emission curve, a bandpass filter near 670nm was chosen. Image is created using BD Fluorescence Viewer (http://www.bdbiosciences.com/us/s/spectrumviewer).

Intensity independence was studied intensively. Each 1-D image is first normalized by subtracting the noise floor background and dividing by the peak intensity of the 1-D curve. As mentioned above, this normalization makes feature metrics resistant to common imaging artifacts present in 2-D imaging (dye aggregation, improper detector settings, debris contamination, and local evaporation). To test the intensity independence of our algorithms, we simulated poor staining protocols by varying the PMT gain of our instrument across an order of magnitude as shown in Figure 3-4. Feature distributions are converted into Z-scores and displayed as a heatmap. Features that deviate from the original population are indicated by the color mapping (more red).

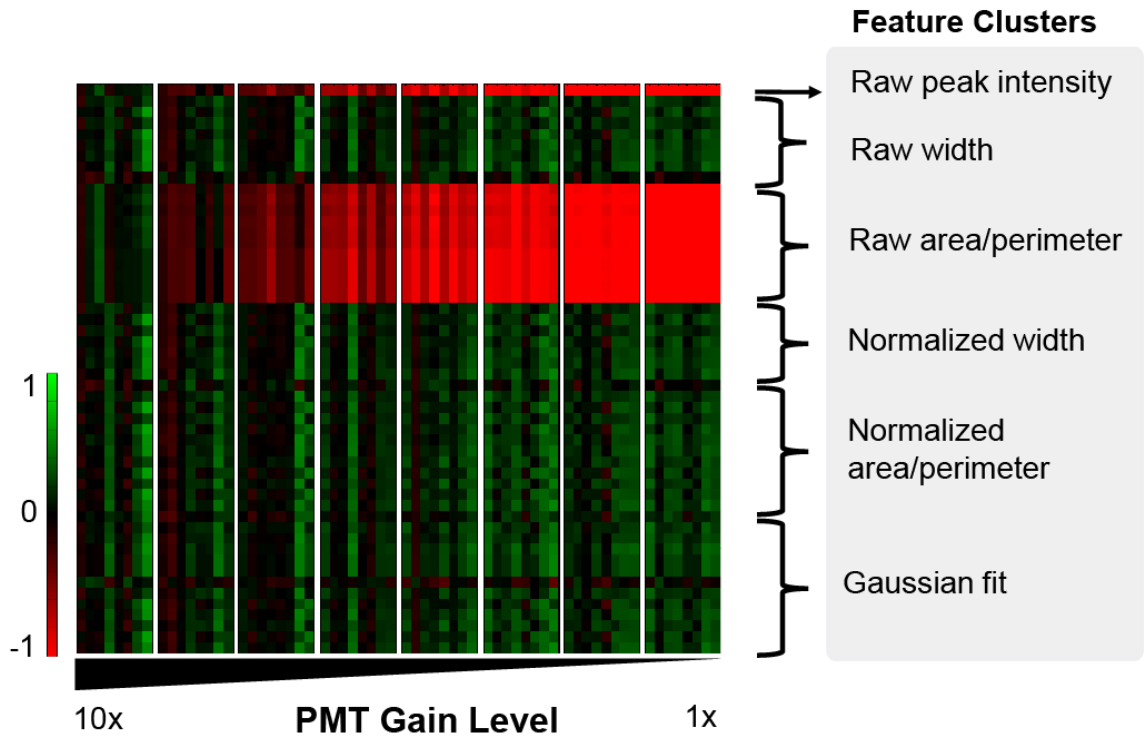

Figure 3-4. Heatmap showing normalized and unnormalized features vs. PMT gain.

Green values represent a positive difference from the mean. Red represents a negative difference from the mean. Eight parallel lanes are imaged simultaneously with 8 separate reductions in PMT gain from 10x down to 1x (relative gain). Each column is an individual lane. The gap between columns represents the separate gain reductions and experimental conditions. Each row is an individual feature but is grouped into general clusters as listed on the right. Image from (Wang & Ehrlich 2017).

As expected, the raw (intensity dependent) features scale directly with PMT gain. Decreasing the gain of fluorescent intensity (from left to right) should result in decreased values for intensity-dependent features. Raw peak intensity, width, area, and perimeter all show significant shifts in feature distributions as indicated by the heatmap. Intensity independence is also confirmed, as normalized features show minimal change when PMT gain is varied across an order of magnitude. Although

there are small differences between parallel lanes, the maximum deviation from the mean across all normalized features is ±10%.

To address the spatial lane-to-lane variance of the optical system, mainly due to field aberrations in the optics, we collected data using uniform 2.5-µm-diameter fluorescent polystyrene beads (Invitrogen Align Flow #A7302) (Figure 3-5). Beads are suspended at 2 million beads/mL density and flowed through 14 parallel lanes in the microfluidic chip. Fluorescent excitation is captured by the PMC and features are calculated based on each individual scan described in Chapter 4. Selected features are plotted and show in Figure 3-5 for analysis of variance across all 14 lanes.

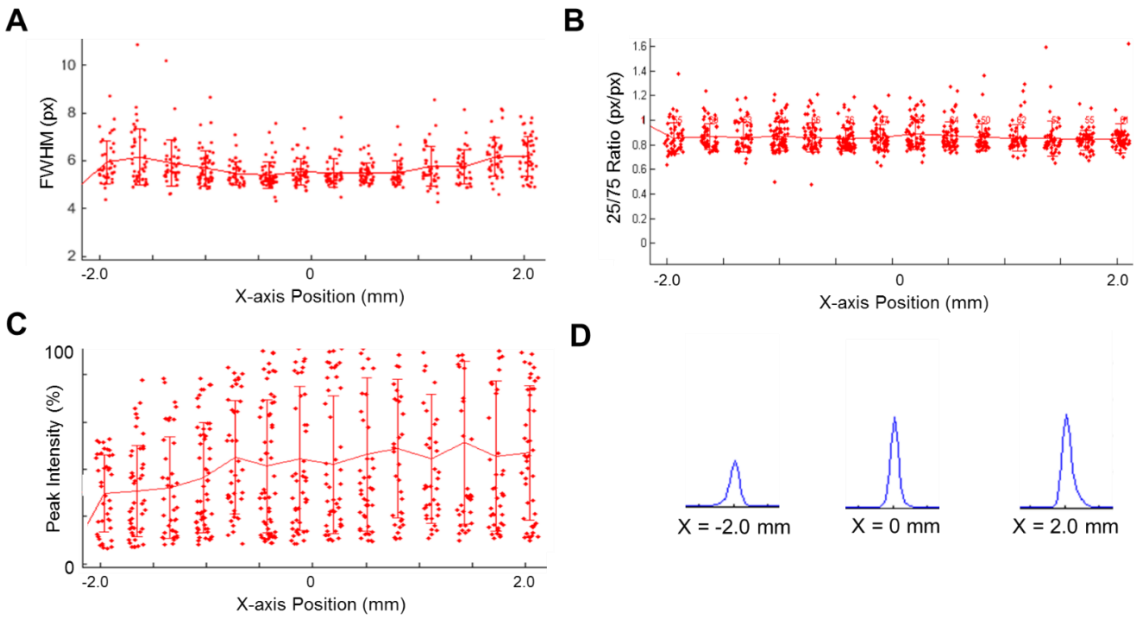

Figure 3-5. Lane variance across parallel lanes using new galvo scanning optics.

Features plotted for 2.5-µm-diameter fluorescent polystyrene beads. Beads are imaged across 14 parallel fluidic lanes. A) Raw feature calculations across entire 4mm scanning region. Means in each lane have a typical U shape profile. X-position represents the axis parallel to the laser scanning path which scans

periodically across parallel fluidic lanes. B) Normalized feature that uses a ratio between widths. Much less variance. C) Peak intensity across lanes shows that features are largely independent of intensity. D) Representative 1-D images taken from 3 extreme locations within the chip. The difference in shape show an average profile of each lane. Image from (Wang & Ehrlich 2017).

For unnormalized intensity dependent feature (FWHM), the coefficient-of-variance (CV) was 19% for edge lanes and 7% for center lanes (Figure 3-5A). The maximum deviation from the mean was +8% for edge lanes and -6% for center lanes. This showed the initial problems that we had with spatial variance across lanes. These features are a sensitive measure of the laser beam shape factors at the focal plane. In Figure 3-5B, we analyzed a normalized feature summarized as the 25/75 ratio. This feature is the log of the full width at 75% peak divided by the full width at 25% peak for a single cell event and normalized to a control sample of the same beads. The variance for the 25/75 ratio feature is much lower than the previous unnormalized feature. To test if our variance was a function of laser power, we also looked at peak intensity vs. X-position (Figure 5-3C). Peak intensity measures the maximum signal peak from each unnormalized 1-D image. This feature is equivalent to the single point measurement obtained from FCM. The variance in peak intensity did not show any correlation with feature variance. However, peak intensity can be used to measure the slight tilt along the scanning axis and an asymmetric loss of fluorescence strength. Finally, representative 1-D image scans from the left, center, and right fluidic lanes are shown in Figure 3-5D. Each profile is a cumulative average peak intensity of all beads within a single lane. The shape of the bead profiles can serve as useful diagnostics of the optical alignment and residual optical

aberrations in the hardware.

Despite the imperfections in alignment and optical design, accurate scoring is preserved through normalization algorithms. Figure 3-5B shows how typical feature variance is compensated with our algorithms. An alternate method to reduce this variance is to separate each lane into its own separate data analysis. While this removes lane-to-lane variance, it also removes inter-lane comparisons and reduces the well throughput. Another method to reduce spatial edge effects would be to use professional machining methods to perfectly align all the lenses and internal optical components.

3.2.2 Scattering

Side scatter and forward scatter are common channels in many cytometry panels. Scattering information is useful for measuring size and shape/complexity factors of cells. One common assay uses strictly scattering channels to determine multiple subpopulations of T cells (Figure 3-6). Forward scatter indicates size differences and side scatter indicates internal shape complexity (Nicholson et al. 1996).

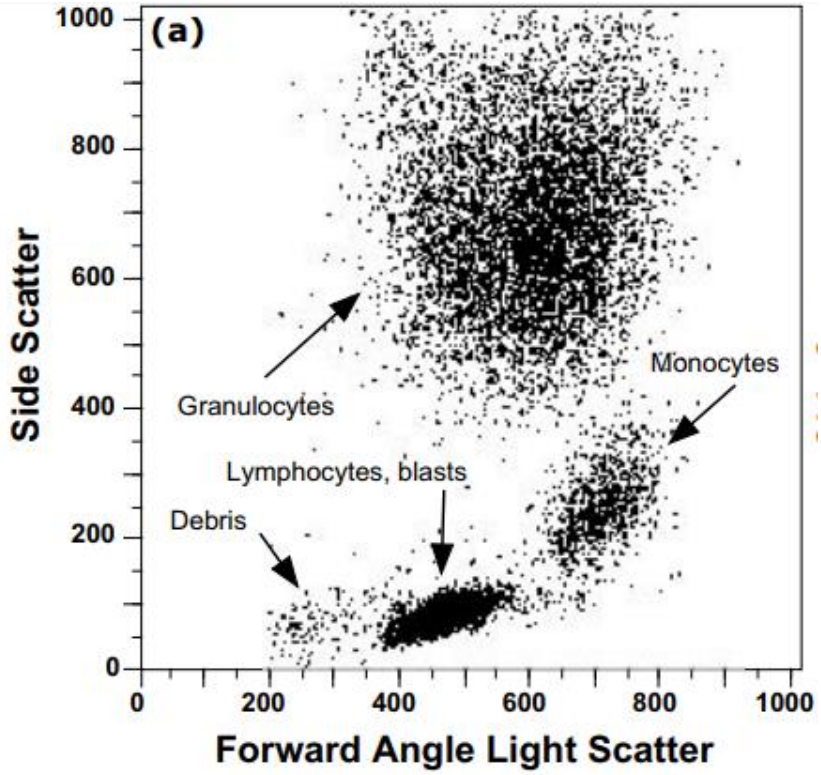

Figure 3-6. Side scatter vs. Forward scatter of T cells.

Clusters of different T cell types are identified without any receptor labeling. High internal complexity is detected using side scatter while overall size is detected using forward scatter. Subpopulations such as monocytes, lymphocytes, and granulocytes can be identified by their corresponding side scatter to forward scatter ratios. Both axes are relative strengths of scattering intensity. Image taken from Principles and Applications of Flow Cytometry (Roger S. Riley n.d.)

Many attempts were made to incorporate a fiber optic cable to pick up side scatter. Methods included micro-machining internal channels inside the poly(methyl methacrylate) PMMA microfluidic chip, using solvents to smooth out internal surfaces, testing various angles to place the fiber optic (direct back scatter to 90˚), and trying different core sizes. We discovered that a constant noise floor was produced in our scattering detector by surface roughness and reflections in the microfluidic.

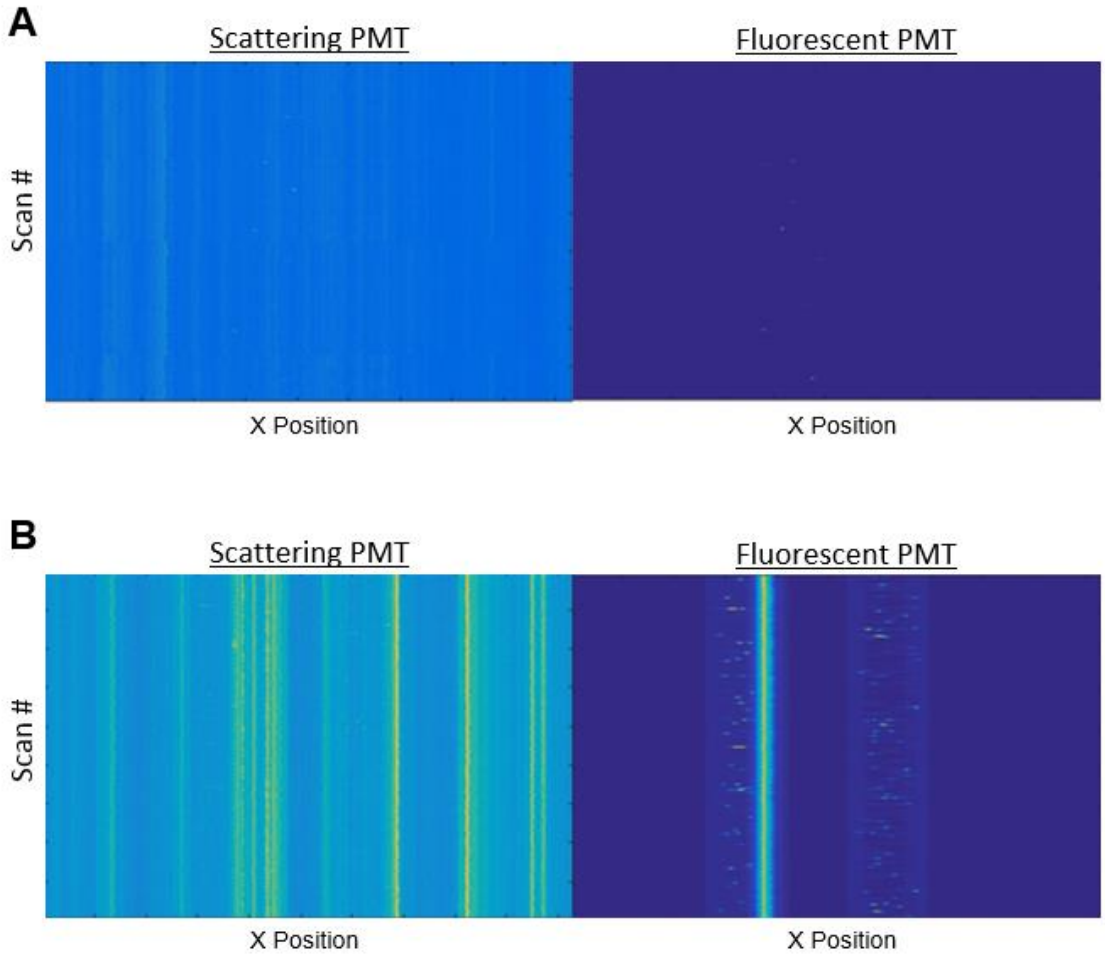

Figure 3-7. Scattering experiments using plastic beads and fiber optic cable.

A) Scattering data obtained from PMMA chip results. Left-hand plot shows the collected 488nm backscatter light using the scattering PMT channel. Each row is a separate scan with the laser. The x-axis represents the position of the laser (4 mm total width). The fiber optic cable is placed underneath the chip at a 45˚ angle. Right hand plot shows the fluorescent PMT channel (Alexa 488) to detect the presence of a cell. B) Methods are replicated using a glass chip. Left is scattering PMT channel. Right is corresponding fluorescent PMT channel (Alexa 488).

One can see on the lefthand side of Figure 3-7A that the scattering signal from the PMMA chip was barely observable above the noise floor. When the PMMA chip was replaced by a glass etched version, the signal-to-noise (SNR) was much higher

(Figure 3-7B). These results confirm observations from the literature. The microfabrication and molding processes that we use lead to micro-defects and roughness in the fluidic walls (Diaz-Quijada et al. 2007; Wang et al. 2011). These caused high optical and electronic noise (PMT gain was near 100%), and resulted in unusable SNR.

3.2.3 Electronics

It was determined empirically that a 60 kHz sampling rate at 12.5 scans/s resulted in a nominal 1 μm resolution. The 1 μm spatial resolution was selected because previous studies indicated that enough information was preserved at this resolution (McKenna et al. 2011). To verify the resolution, the sampling rate was adjusted in the ADC until the pixel width matched 150 pixels for each fluidic lane, each of which is 150 μm wide. Another factor to consider was the integration time of each pixel. To maximize sensitivity and SNR, 17 μs integration time was measured to be a good compromise between speed and signal intensity, for our specific laser power wattage. The Argon-Ion laser has a maximum power output of 50 mW.

Other improvements in the electronics involved the incorporation of custom conditioning circuits to modulate the galvanometer (Appendix 2). This required a combination of high-pass and low-pass filters and integrators using op-amps. A custom Arduino circuit was built to control the PMTs automatically using serial input/output (Appendix 3). Minor electrical components were added to minimize electronic interference (shielded cables, grounding capacitors, etc.).

3.2.4 Microfluidics

The microfluidic chip was fabricated using standard photolithography, electroplating, and polymer embossing into a final poly (methyl methacrylate) (PMMA) mold. The dimensions of each channel measured 150 μm x 40 μm (Figure 3-9). Each fluidic lane was separated by a 150 μm wall. The chip material PMMA was chosen for multiple practical reasons. PMMA is easier to machine input and output wells and can be imprinted quickly using a single master embossing mold. The sealing tape method is replaceable which simplifies cleaning and makes each chip reusable. Compared to laser etched fusion bonded glass chips in the previous iteration, the process is simpler, more scalable, and cost effective. A summary of the microfabrication process is shown in Figure 3-8.

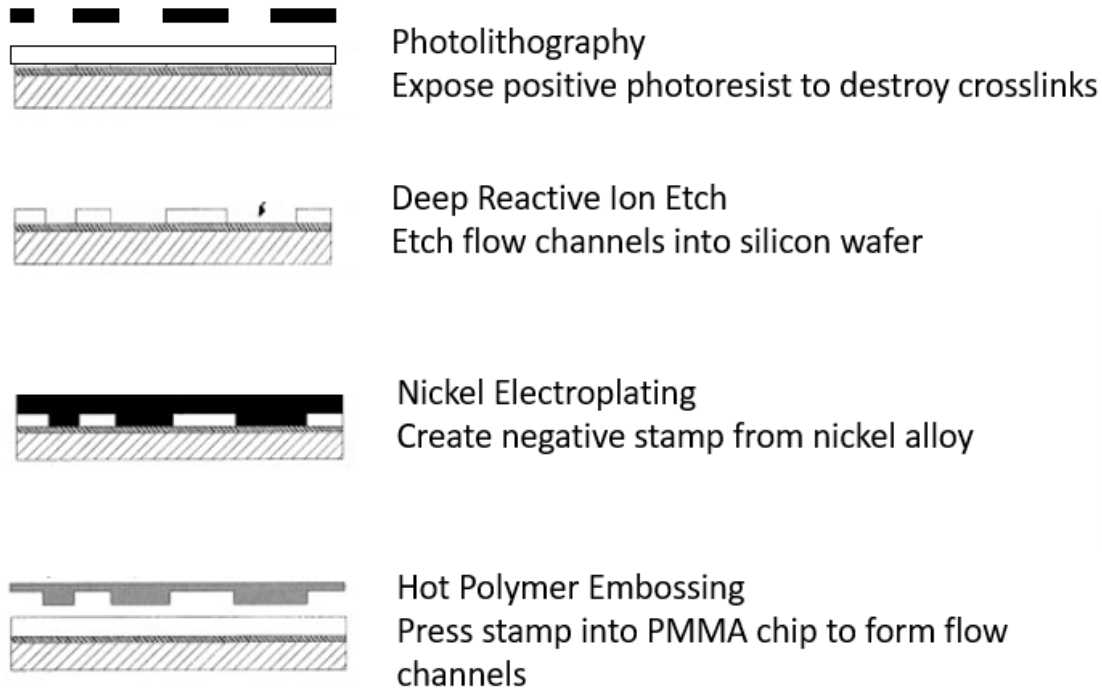

Figure 3-8. Microfabrication overview for the microfluidic chip.

Masks with flow channel geometry were generated in AutoCAD and printed with high quality photomask ink (Output City). A tree geometry was selected over a ladder geometry for negative pressures because of better resistance distribution under steady state (V. Hessel, A., Renken, J.C. Schouten 2009). Silicon wafers (University Wafers, 150 mm SSP Si) were dehydrated at 115˚C for 5 min on a hot plate. Then wafers were spin coated with HDMS at 3000 rpm for 30s. Positive photoresist (Shipley Micro posit S1818) was spun at 2000rpm for 3 µm thickness. Wafers were pre-baked at 120˚C for 120s. Wafers are exposed in a mask aligner (Karl Suss MA6) at 200mJ. Wafers are then developed in photoresist developer solution (MF319) and rinsed with DI and post-baked for 5 min at 120˚C. Deep reactive ion etching (DRIE) was used to etch each wafer to a depth of 50 µm (Bosch process SF6 etch at 7.5s with C4F8 passivation 3.5sec for 60 cycles). We then deposited 500 µm of titanium using a CHA evaporator as seeding layer for electroplating. Wafers were electroplated to a thickness of 700 µm with nickel to create master mold (NiCoForm).

The embossing protocol was adapted from similar embossing techniques in the literature (Chen et al. 2010; Shen et al. 2002; Mathur et al. 2009; Tsao & DeVoe

2008; Narasimhan & Papautsky 2004). Plates were heated to 150˚F and 290˚F. The master mold was aligned with a pre-etched PMMA chip and silicone rubber (1/4" McMaster-Carr 8632K44) sandwich into embossing machine (Carver Model 3912). The mold sandwich was preheated for 10 min, then applied with 900 kPa for 2 min. After cooling for 2 hours under pressure, chips were sealed with silicone adhesive TempPlate RT Optical film (USA Scientific #2921-7800). A 0.25/20 threaded fluidic adapter and 1/16" diameter polyethylene tubing was attached to the vacuum output port. The chip layout is shown in Figure 3-9.

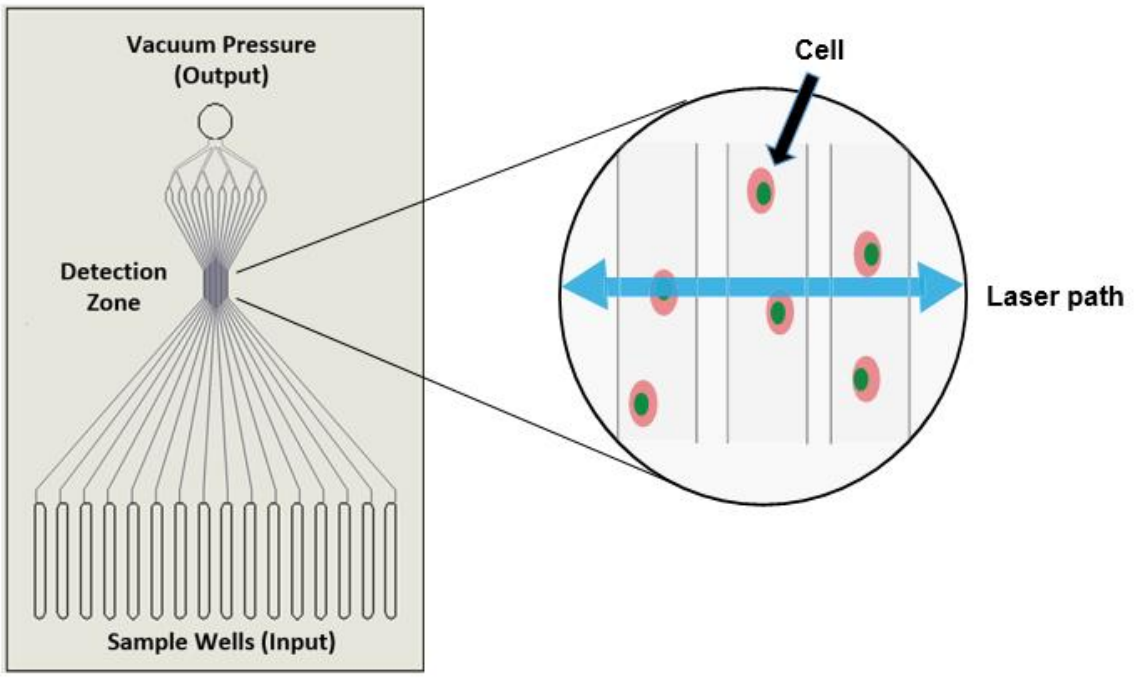

Figure 3-9. Microfluidic chip layout as seen from above.

Samples are loaded into 16 input wells at the bottom and flowed through the chip using negative vacuum pressure (-0.10 PSI). A magnification of the detection zone is on the right which shows the perpendicular laser scanning to the flow direction. Cells flow through the parallel fluidic lanes in the laminar flow regime. The laser intersects the cells at random cross sections.

One of the interesting results learned from the microfabrication process was during the embossing development. Since the input and output wells were pre-drilled into the PMMA and then embossed, we needed to maintain the integrity of the wells, but at the same time, maintain a solid imprint of the mold. Traditional hot embossing is always done with a solid blank chip first, and then holes are cut. Due to the reverse method, we had to carefully adjust the temperature gradients and pressure to determine the optimal conditions for the reverse embossing method. This method may be a new approach to microfluidic embossing since we could not find any literature on this method. It has advantages over the standard method since the reverse embossing technique allows the input wells to maintain structural integrity. Machining input wells into plastic can often destroy small features in microfluidic chips. The structural integrity and shape of the lanes was confirmed with a manual profilometer (data not shown).

Other chip iterations were planned but only partially completed. One of those iterations was a 96-well lane chip. By using 50 μm wide lanes, we could fit 96 wells into a 10 mm scanning region. This would allow for even higher throughput screening but we did not have the time or resources to implement it (Appendix 4).

3.3 PMC Operation

3.3.1 Cell preparation

We developed a standardized protocol for sample preparation. This protocol was used with little variation for all the experiments that follow.

Cells are fixed by adding 10 µl of 37% formalin (Sigma #F8775) for 15 min on ice, and then permeabilized with 0.1% Triton X-100 for 10 min. Cells are centrifuged, aspirated, and re-suspended in our custom flow/staining buffer, which consists of 1% BSA (bovine serum albumin) and 10 mM EDTA in PBS (phosphate buffered solution). Appropriate primary antibody is added and incubated overnight at 4˚C. Cells are washed and re-suspended in flow buffer. For the secondary staining, 10 µg/mL of anti-rabbit Alexa 488 (Invitrogen #A11008), 1:100 propidium iodide, and 10 µg/mL of RNase A are added and incubated for 30 min at 37˚C. Cells are washed twice and fixed a second time for 3 min. After one final wash, cells are filtered with a 40 µm mesh and re-suspended at a density of 2 x 10^6 cells/mL in flow buffer with 30% OptiPrep.

All the above protocols were optimized over a course of 7 years. Each concentration and incubation time of every compound was fully titrated to determine the optimal point. For the staining, fixing, and permeablization protocols, the time intervals and concentrations were chosen to achieve the maximal nuclear fluorescence of the antibody staining but also minimal cell clumping and deterioration of the membranes. Paraformaldehyde was tested to be inferior to

freshly prepared fixing buffers with 37% formalin. Triton X-100 was determined to be better at permeablization than saponin, which is another common detergent. The flow buffer was carefully constructed to reduce the sticking of ions and DNA and cell debris. The concentration of OptiPrep was carefully titrated, too high would reduce flow rates, but too low would increase cell settling and clogging. Concentrations for all antibodies were titrated for maximal fluorescence at saturation. Higher concentrations also allow for lower incubation times, which is crucial for high-throughput processing.

3.3.2 Cell processing

Before imaging cells in the PMC, samples are stored temporarily at room temperature in a closed box to prevent photobleaching. Cells are then manually loaded into the wells using a pipettor. Each lane was loaded with 4 µl of sample volume at a cell density of 2 million cells/mL, roughly 8,000 cells per well.

When using primary cells, sample volume efficiency is especially important as cells are limited in quantity from a single donor. The PMC has very low volume requirements of 4 µl per well. A 96-well plate typically has a working volume of 50-200 µl per well. Even for a 384-well plate, each well usually requires an optimal working volume of 15–150 µl. In our protocols, 50–150 million purified CD3+ T cells were obtained from each individual donor. Even considering 50% cell loss from staining and washing, there are still 25–75 million usable cells, sufficient for 3000–9000 separate wells.

After loading, cells were siphoned through the chip at -0.10 PSI vacuum pressure. After each run, wells were flushed with 1% detergent for 1 min. At the beginning of each day, the PMC was focused to the optimal Z-axis position. Optimal focus was confirmed by measuring the FWHM (full width half max feature) and peak intensity at various Z-axis positions. Figure 3-10 shows the data from 9 different Z-axis positions. It was confirmed that the optimal focal point existed where the FWHM was at a minimum and the peak intensity was at a maximum.

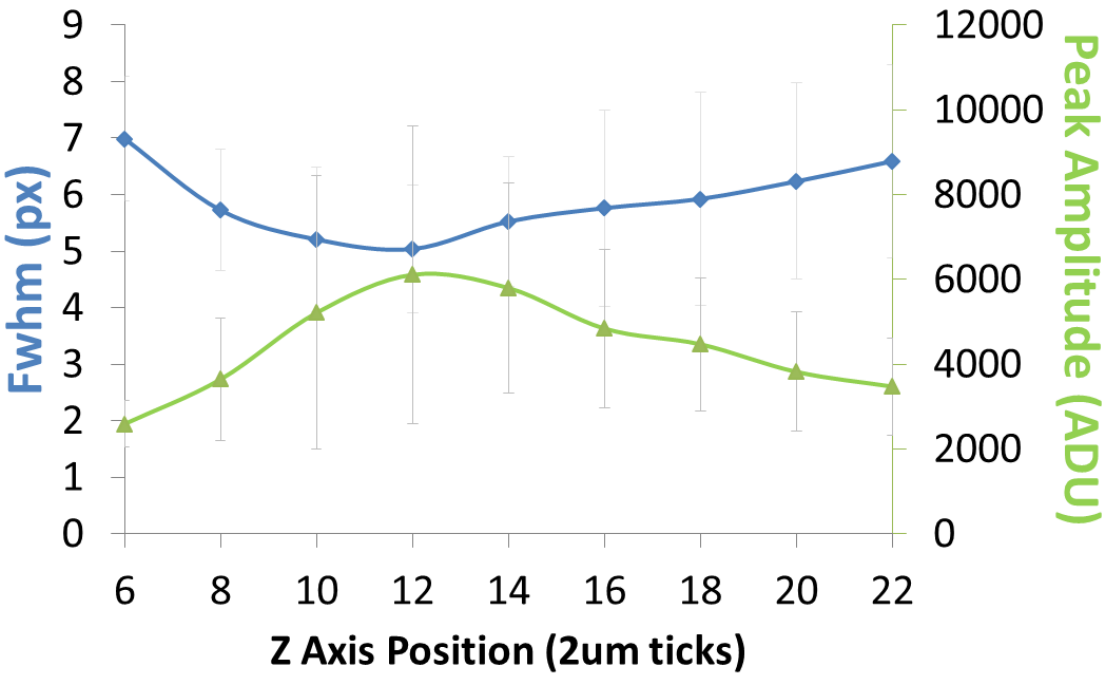

Figure 3-10. Plot of FWHM and Peak intensity vs. Z axis position.

FWHM and Peak amplitude feature means plotted for beads as a function of vertical Z position. The blue curve shows the mean FWHM value in pixels of beads at a certain Z position. The lowest FWHM feature is around a Z position of 12. The green curve shows the mean peak intensity feature of beads vs Z position. The lowest amplitude is also around 12. Vertical bars represent standard deviation across 10 replicates.

3.3.3 Flow modeling

Some work was necessary to get consistent low velocity flow within the microfluidic chip. Negative pressure is more susceptible to inconsistencies in flow, especially with parallel lanes (Yi et al. 2006; V. Hessel, A., Renken, J.C. Schouten 2009). The microfluidic chip was modeled to identify improvements and to calibrate the flow parameters to maintain consistent flow and minimize flow rates for optimal sample imaging. Resistance in a rectangular channel can be estimated using $(12*\eta*L)/(w*h^3)$, where w is width, h is height, η is viscosity of the fluid (0.001 pa*s), L is the length of the lane. Resistances are added in parallel to determine overall flow rate and velocity. Based on the density of the fluid (1100 kg/m^3) and the velocity, length, and viscosity of the fluid, the flow regimen should be completely laminar in our chip, based on Reynolds number, and confirmed with empirical observation. The model was used to predict flow rates as a function of pressure. Actual flow rates were measured using particle tracking and the results are compared with the theoretical model in Figure 3-11. To measure actual flow rate, a camera was placed above the microfluidic lanes and opaque beads were flowed through the chip. Using the frames/second as a reference, the velocities of each individual bead could be tracked and calculated (Appendix 5-6).

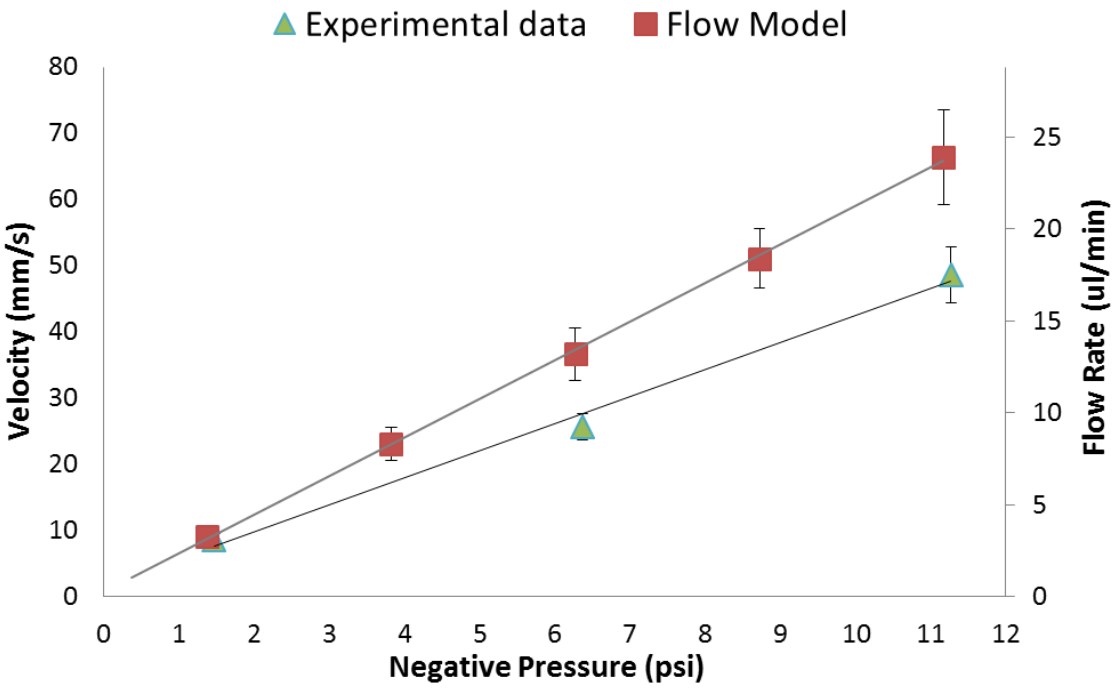

Figure 3-11. Laminar flow model calculated from resistance of microfluidic chip.

Velocity and flow rate measurements obtained from both empirical data and theoretical model. Red indicates the velocity calculated from the theoretical flow resistance model. Green triangles are mean values from experimental bead tracking data. Increasing the negative pressure results in higher flow rates and velocities. There is a direct linear relationship between pressure and velocity as expected from the theoretical model.

3.3.4 Flow issues

Sample handling protocols required extensive optimization to maintain smooth operation of the PMC. For example, we discovered that double fixing cells with formaldehyde is crucial to eliminating sticking of the cells. The permeablization step causes DNA/RNA leakage which causes cells to stick to the silicone tape seal. Bubbles and debris accumulation were also significant problems (Figure 3-12, Lane 3). High negative pressures would result in cavitation and turbulence at channel

bifurcations (Lane 7). Large cell debris would often be trapped at the input port (Lane 8). If the velocity of the fluid was too low, the cells would settle at the bottom of the channel (Lane 4). Surface tension is high within fluidic channels as PMMA is hydrophobic. Although various surface modifications were attempted (Diaz-Quijada et al. 2007), the solution was determined to be a positive pressure flush with 1% Alconox. This is a detergent that lowers surface tension and flushes out cell debris. The use of a flow buffer and filtering the cells through a 40-μm mesh also helped dramatically in reducing clogs and cell sticking. EDTA and bovine serum albumin (BSA) binds to any non-specific 'sticky' epitopes and ions. OptiPrep (Iodixanol, a density gradient medium used for cell isolation) was used to density match the cells to prevent settling. This additive has a density of 1.320 ± 0.001 g/mL and is useful in suspending cells in buffer. The exact concentration was empirically determined. Higher concentrations result in slower velocities and clogged flow, lower concentrations result in cells settling to the bottom of the chip.

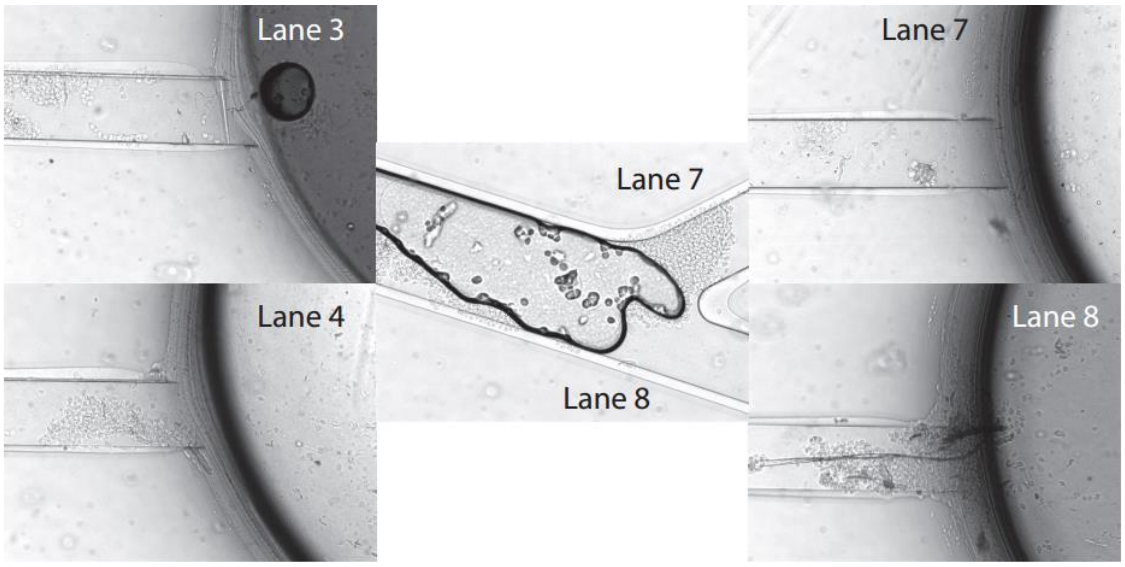

Figure 3-12. Common issues, bubble formation and cell debris.

Various flow issues can be seen in the above images. Images were taken at 40x magnification with widefield phase contrast microscope. Cells can get stuck along the sidewalls, at the initial input port, also at bifurcations. Without proper filtering of the cells, large clumps of debris can also enter the channels and clog them up permanently. Each image is obtained from the input location of separate lanes as indicated by the labels (lanes 3 – 8).

3.3.5 Data storage

The PMC data sampling rate captures images at 14-bit depth at 60 kHz samples/s. Each sample is imaged for 2,500 scans at 12.5 scans/s (200s) resulting in a 22 MB data file for each color. However, much of these data are empty space, which we immediately discard (this includes the return scan of the galvanometer, the walls between the individual lanes, extra space at the outer edges of the lanes). To calculate the actual data that is stored on our hard drives, a single cell event from our method is a 160 pixel vector with a 14-bit depth which is equal to 280 Bytes. Each lane generates 300–400 raw cell images, which is about 110 KB per well. For a

two color assay, the total data is doubled to 220 KB. Including the data from feature calculations, an additional twofold requirement is needed for a total of 440 KB per sample. As such, our method is very efficient with regards to data requirements. The EMD Millipore ImageStream®X Mark II claims a data storage requirement of 500 MB for 10,000 events (Millipore 2017). In comparison, 10,000 events in the PMC would only need approximately 13 MB. This is almost a 40-fold reduction in file size.

Chapter 4 - Aim 2 – Automated statistical workflow

4.1 Introduction

We designed a statistical workflow which is self-normalizing for high sensitivity with minimal cell count. We chose to automate the entire process to produce a single readout 'activity score' for each sample. By selecting the most relevant features from more than 150 image criteria, our algorithm condenses the 1-D image data into a single readout with a regression model. The 'activity score' is ideal for drug screening since assays often involve sifting through thousands or millions of compounds and measuring the drug response from each one. The 'activity score' is a necessity for screening applications to quickly understand the drug response from a single experimental condition. The statistical workflow is data efficient and eliminates subjective operator biases and/or complicated calibration. The algorithms are automatically calibrated to the specific controls being used. This allows for simple operation, rapid assay development, and on-the-fly data scoring. The true strength of our technology, when compared to existing HCS, shines in our speed, simplicity, and objectiveness of well scoring.

4.1.1 Statistical nature of the PMC

The PMC requires statistical algorithms to differentiate and profile cell populations. The way the PMC gathers 1-D data is highly variable by nature. The first source of variability is from flow. Because there is no hydrodynamic focusing in flow channels, cells will pass the laser at different heights and orientations. Each cell will be

scanned through a single random cross section as demonstrated in Figure 4-1.

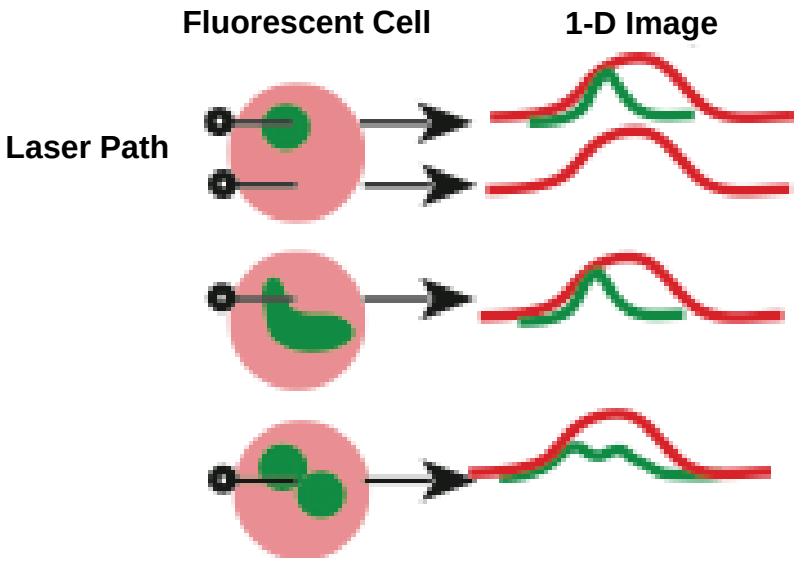

Figure 4-1. Possible scanning cross sections within a cell.

Each cell is scanned by the laser through a random cross section. The colors red and green represent two separate fluorophores. On the left, the cells are intersected by the excitation laser. The righthand side shows the corresponding 1-D image that is generated. Each color will be captured by a separate PMT. Image from (Mckenna et al. 2011).

There is an inherent biological variability within each cell. This variability includes cell clumping, inconsistent staining, heterogeneity of cellular contents, and cell cycle. In addition to biological variance, there is optical noise from the laser, auto-fluorescence of chip and background solution, electromagnetic interference, thermal/readout noise, and optical reflections/scattering.

These factors add to the 'noise' of the 1-D approach which is why statistical analysis is ideal for this platform. Much of this noise can be systemically eliminated by selecting proper controls for each experiment. Normalization is critical in reducing persistent sources of variance. Analyzing distributions instead of

individual cells allows us to measure the characteristics of a cell population despite unknown variances. Changes in cellular phenotypes across a population will result in overall shifts in distribution mean or standard deviation.

4.2 Statistical workflow

4.2.1 Raw data and automatic thresholding

As described in Chapter 3.3, raw 1-D images are collected and stored by the PMC after each run. For a cell to be classified as a successful event, it must have a peak intensity more than 6 standard deviations (SD) above the background. A single run produces about 300–400 events per sample. It has to satisfy a certain range for nuclear width and must contain only one peak. This range is indicative of proper focusing and correct size for a T cell. Any events that are double scanned by the laser are also removed. Each cell is fitted to a Gaussian curve and the R^2 value must be higher than 0.95. The thresholding procedure is summarized in Figure 4-2.

$$\text{Qualified Event} = \begin{cases} \text{Peak} > \mu_{\text{background}} + 6 * \sigma_{\text{background}} \\ R^2 > 0.95 \end{cases}$$

Figure 4-2. Threshold for a qualified event.

Cells must pass certain parameters before being considered as a qualified event for analysis. μ and σ are the mean and standard deviation of the background intensity. R^2 is the coefficient of determination of a Gaussian curve fit to each 1-D cell image. This is to ensure that each cell is properly focused, a singlet, and is the correct shape and size for a T cell.

As mentioned above, each sample is loaded with about 8,000 cells but only 300–400 events are captured from each sample. This is a hit rate of about 5% of the total cells that flow through each fluidic channel. However, we have shown previously that this is more than enough events to reliably characterize a sample (McKenna et al. 2011). The distribution generated from each well is reproducible and mostly normal (additional analysis in further sections). An example of a typical raw output from the PMC is in Figure 4-3.

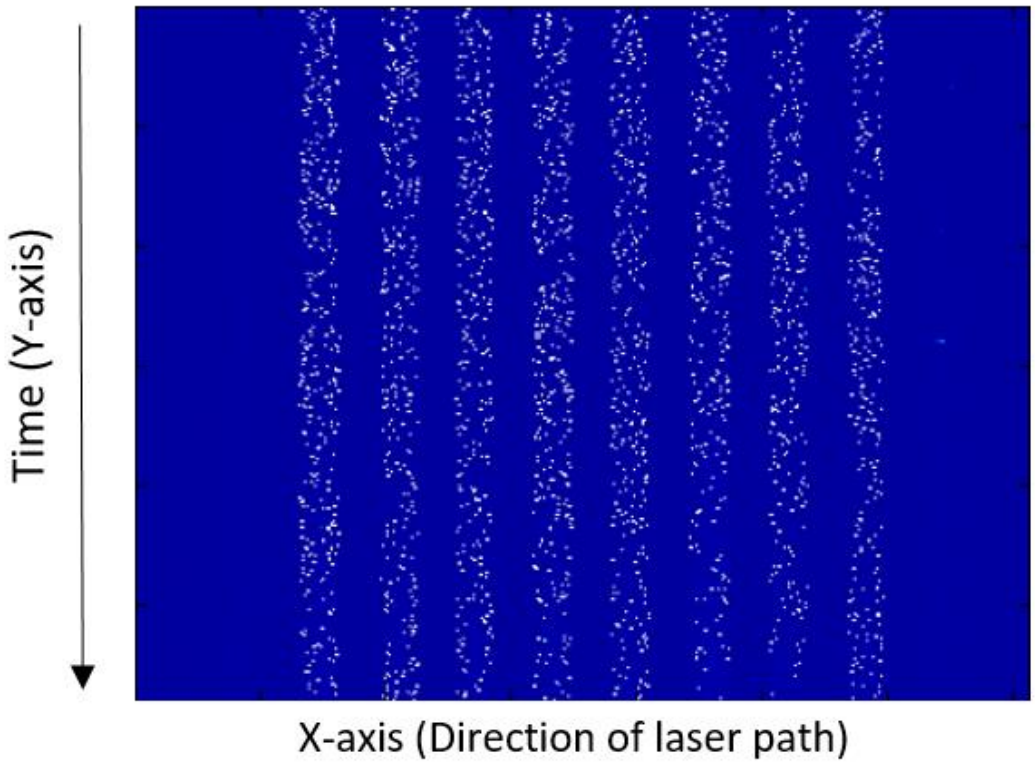

Figure 4-3. Raw data output from a single run.

8 lanes are being scanned for 2,500 scans. Each row of data represents a new scan imaged by the PMC, which is a function of time. The x-axis represents the specific laser location across a 4mm detection zone, which is also a function of time. Each white line indicates a cell that has passed the automatic threshold requirements and will be stored in a database.

4.2.2 Feature generation

For each qualified event, "features" are generated and pre-filtered before further analysis. The background noise floor is subtracted first. Compared to background subtraction from 2-D HCA, 1-D background subtraction is trivial and does not require any complicated edge detection or contrast gradients or averaging. Subtracting the background noise is as simply as subtracting the next row. Each row of pixels directly underneath an event will contain the same electronic, spatial, and fluorescent noise. Each image is also smoothed with a 3 pixel window using the SGO-LAY algorithm in Matlab. Before any feature is calculated, each event is normalized to a unitless height of 1 by dividing by its own peak intensity. Any data below 20% of the peak is discarded. This is because the laser spot size is 2 μm in diameter. Each 1-D image can be thought of as a convolution of the laser spot and the internal fluorescence. As the laser is approaching a cell, there is residual fluorescence that is excited due to the relative size and proximity of the laser spot. As confirmation of this optical effect, each 1-D image is roughly 2–4 μm wider than the actual size of the T cells.

Next, hundreds of morphological features are generated from each 1-D cell event. These features have been adapted from commonly used features in 2-D HCA (Ng et al. 2010; Carpenter et al. 2006). A visual representation of how our features are calculated is shown in Figure 4-4.

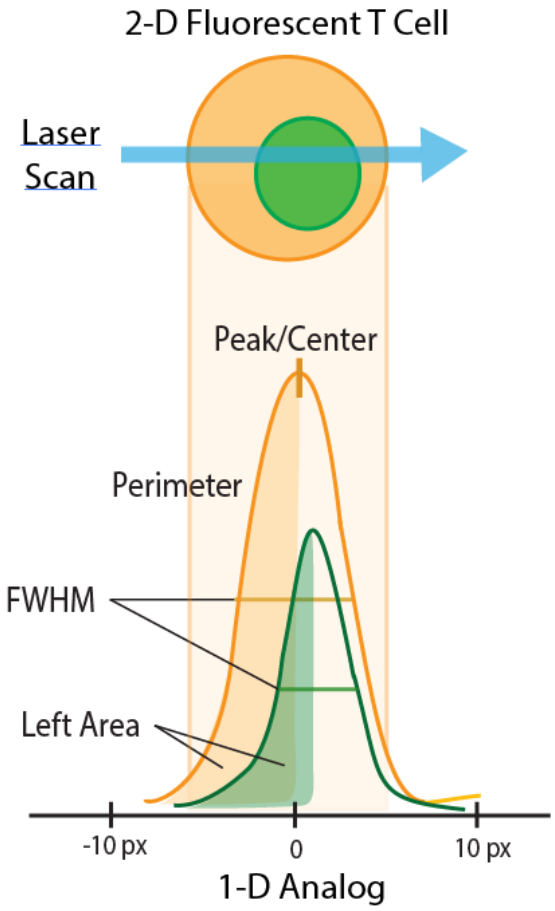

Figure 4-4. Feature calculation for a typical 1-D event.

Features are calculated from each 1-D image that are representative of the underlying localization of biomarkers. The 2-D analogue is shown above the 1-D image. Features such as perimeter, area and full width half max (FWHM) are calculated and similar to their 2-D analogues. Image from (Wang & Ehrlich 2017)

These features include but are not limited to: area, perimeter, full width half max (FWHM), upper and lower $25^{th}/75^{th}$ widths, left/right top/bottom symmetry, smoothness, roundness, slope, inflection point, cytoplasm vs. nuclear regions, and Gaussian fit statistics. Each feature is repeated for each PMT channel as well as

inter-comparisons between PMT channels. These features attempt to provide a full comprehensive characterization of each 1-D curve. In this way, one can preserve the informational content of biomarker localization within each cell. A full list and summary of the features is provided in Appendix 7.

All the features are compiled into histograms and then normalized to a control well. The negative control is run twice, once to generate a control well baseline distribution, and again to generate the actual negative control distribution for the experiment. Normalizing to a control well reduces spatial variance from chip defects or laser/well position. Features are converted into a Z-score by subtracting the mean from the control sample and then dividing by the SD (Figure 4-5). Extreme outliers greater than 4 SD are removed from each distribution. An example of the final normalized distribution for a single feature is in Figure 4-6.

$$Z_{j|sample} = \frac{X_{j|sample} - \mu_{control\ well}}{\sigma_{control\ well}}$$

$$\text{Sample Feature Set} = \{\overline{Z_1}, \overline{Z_2}, \overline{Z_3}, \ldots \overline{Z_i}\}, \text{ where } \overline{Z_i} = \frac{\sum_1^n Z_{j|sample}}{n}$$

Figure 4-5. Normalization to control well to reduce spatial variance.

μ and σ are the mean and standard deviation of the control well. Z represents the mean Z-score for each event *j*. Feature distributions are compiled and a mean statistic is calculated for each feature *i*. *n* is the total number of events per sample.

The mean statistic calculated for each feature distribution to form a set of normalized features for each sample. Initially, the underlying distributions were unknown in the PMC so non-parametric statistics were used to analyze feature

distribution. The Kolmogorov-Smirnov (KS) statistic is a measure of the maximum distance between two cumulative distribution functions (CDF) (Green line depicted on Figure 4-6) (Dragiev et al. 2011). After a certain point, the PMC protocols were optimized to generate normal distributions so the mean statistic was used in place of the KS statistic for the majority of our assays.

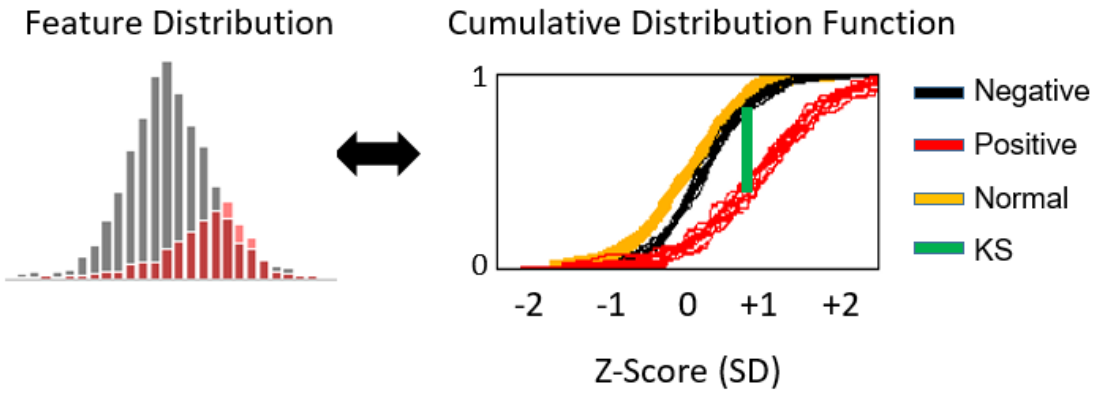

Figure 4-6. Feature distribution for a single feature.

Black represents cells from a negative control. Red represents cells from a positive control. The changes in shape and mean indicate an underlying shift in the phenotype. Left) Typical normal histogram generated from a single well for a single feature. Right) The same distribution but represented as a cumulative distribution function (CDF) and KS statistic (green). Each line in the CDF is a separate replicate. All features are normalized to a Z-score (SD) so that features can be compared with each other.

4.2.3 Post filtering

After the mean statistic is calculated for each feature, the set of features is filtered to eliminate those that fail two separate statistical significance tests. Since we only use the mean statistic from each feature distribution, we have to confirm our assumption of a normal distribution. The first test is a normality test (one-sided

Kolmogorov–Smirnov test) to remove all non-normal features at $\alpha = 0.05$. The second test applies a paired student t-test between each negative control feature and its corresponding control well at $\alpha = 0.05$. A control well is just the negative control run a second time. Any feature that fails the null hypothesis is removed from consideration since any significant difference would imply an operational failure.

4.2.4 Feature selection

After invalid features are removed, the next step is to select a subset of the remaining features for regression modeling. Each feature can be thought of as a separate dimension or degree of freedom. Dimensionality reduction is one of the core principles of HCA since enormous amounts of data can be generated from every image. To reduce the complexity and size of the data set, we begin by eliminating features that are least 'important'. Each feature is ranked according to the difference between the mean statistic of the positive and negative samples. Feature selection is implemented based on minimal redundancy maximum relevance model (mRMR). Many other feature selection algorithms (such as principle component analysis, factor analysis, support vector machine, linear discriminant analysis) were considered but the mRMR model was the least computationally expensive. The mRMR has been used successfully in other HCS assays and shown to maintain high statistical power (Peng et al. 2005). A flow chart showing the feature elimination process is shown in Figure 4-7. The mRMR algorithm iteratively selects the highest-ranking feature, and removes all other correlated features with a Pearson's

correlation coefficient r > 0.5. This is repeated until all features are exhausted or the number of features exceeds the logistic regression over-fitting limits.

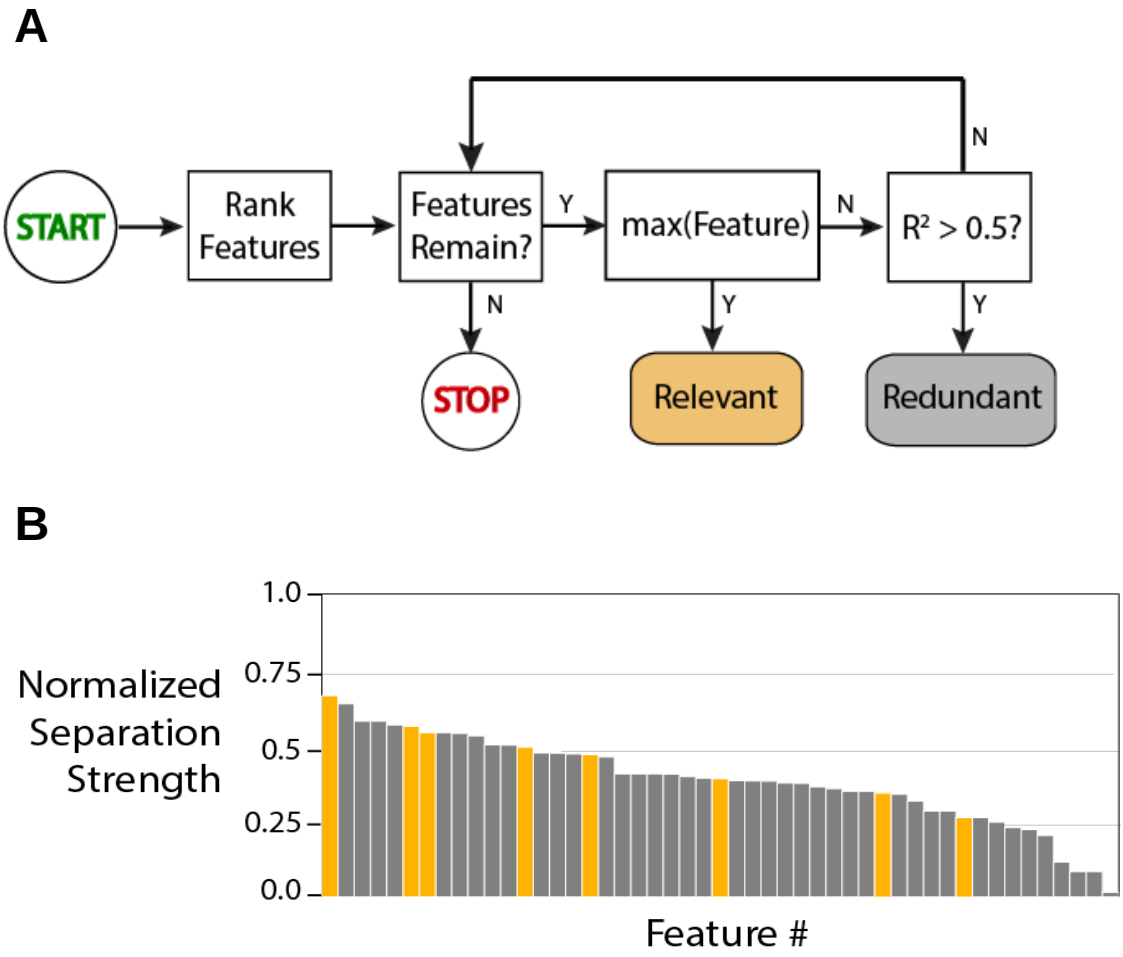

Figure 4-7. mRMR model for feature selection.

A) Flow diagram showing the feature elimination process of the mRMR model. Features are ranked from highest ranking feature to lowest ranking feature. The top feature is selected and removed (yellow). Features that are correlated to previous chosen features are removed to reduce collinearity (grey). The loop is continued until there are no more features. B) Graph that shows the remaining selected features (yellow) from part A. Images from (Wang & Ehrlich 2017).

4.2.5 Logistic regression model

In the final step, the most relevant features that remain are used to generate a binomial logistic regression weighted "classifier". Logistic regression estimates the probability that a set of features belongs to a single binary dependent variable (a positive or negative control sample) based on the weights of multiple independent predictors (these would be the relevant features). We use this probability to represent the 'activity score'/drug response from a sample. The activity score is the linear combination of the features multiplied by their corresponding weighted coefficients (Figure 4-8).

$$Activity\ Score = \frac{1}{1+ e^{-(\beta_0+\beta_1 x_1+\beta_2 x_2 \ldots \beta_n x_n)}}$$

Figure 4-8. Activity score readout defined in terms of logistic regression.

The equation on the right is the probability function of logistic regression. Coefficients are found by using the maximum likelihood estimation which entails finding the set of parameters for which the probability of the observed data is the greatest.

Logistic regression is well suited to simulate an "activity score". In our assays, we always have a positive and negative control sample, and are attempting to understand the drug response with respect to these two populations in a probabilistic framework. The logistic regression also generates a continuous output variable so it can help differentiate between intermediate phenotypes. This is useful for temporal or dose response studies.

A complex phenotypic response from a population of cells can be defined by a simple quantitative readout using our modified logistic regression model. This is useful for screening due to the single continuous output. It is also completely hands-off. The only supervised operation is labeling each sample as a positive, negative, or drug response. The algorithm runs through the entire statistical workflow without any intervention. Since it is does not require previous knowledge of any phenotypes from the control samples, the model is essentially 'sample-blind'. This allows the model to adapt to any new assay effortlessly, as long as the proper positive and negative control samples are selected. A 'sample-blind' approach does not need manual analysis which allows for rapid assay development.

We performed a detailed analysis for algorithmic performance of our initial classifier in a previous paper (Cheung et al. 2015). Using separate training and test sets to construct confusion matrices and calculating common metrics such as accuracy and specificity, we determined that all metrics were near 100% or 0%. A Z' > 0.5 indicates a 12 SD separation which is essentially error free. A Z' = 0.0 indicates a 6 SD separation which is equivalent to a false positive rate of 0.15%. To minimize overfitting, we collected at least 5 events per explanatory variable (EPV). For logistic regression, it is typically assumed that a minimum of 10 EPV is required for a stable model. However, there are sources that have used 5–9 EPV with minimum Type I error rates (Vittinghoff & Mcculloch 2007). Our 5 EPV was chosen mainly due to practical reasons. Since our model generally picks 4–6 features, this would require 40–60 replicates for each control.

4.3 Quality control metrics

The separation strength between positive and negative controls is evaluated using Z' and strictly standardized mean difference (SSMD) as shown in Figure 4-9 (Zhang et al. 1999; Zhang 2007).

$$Z' = 1 - \frac{3(\sigma_p + \sigma_n)}{|\mu_p - \mu_n|}$$

$$SSMD = \frac{\mu_p - \mu_n}{\sigma_p^2 + \sigma_n^2}$$

Figure 4-9. Equations for Z' and SSMD.

Z' and SSMD are commonly accepted quality control metrics for large screening assays. μ and σ are the mean and standard deviation for either positive (p) or negative (n) control.

A Z' > 0.5 is generally used in assays with very strong positive and negative controls such as ELISAs, binding assays, and other similar chemical assays (Bray & Carpenter 2004). However, for imaging assays where the results are much more complex and closer in phenotype separation, SSMD is preferred (Bray & Carpenter 2004). In this case, for medium to strong controls, a SSMD > 6 is considered sufficient. For weak controls with minimal separation, SSMD > 3 is considered sufficient. With respect to T cell activation, high separation values imply a large shift in biomarker spatial localization. This can be construed as a 'healthier' cell population with a strong T cell activation response. Low separation values would imply a more 'anergic' non-responsive cell population, with respect to T cell activation.

Chapter 5 - Aim 3 – Assays

5.1 Introduction

The first sections have focused mainly on the instrumentation and data analysis for the PMC. This section progresses to the assays we developed by utilizing the PMC platform. One target application of this work is to construct an anergy assay in primary T cells to study the immune checkpoint pathway, so a series of preliminary validation assays were designed with that goal in mind. In order to study and screen for immunotherapy drugs, we needed to design an assay to systematically probe drug responses from immuno-compromised cells. One of the main difficulties in probing immuno-compromised cells, is that compromised cells naturally have a negative phenotype and lack of drug response. Therefore, we needed a method to induce immuno-compromised cells alongside healthy responsive cells, and to compare the relative drug response from both phenotypes.

5.1.1 Motivation

The goal of immunotherapy is to restore immuno-compromised/anergic T cells (Marincola et al. 2003). Any assay that attempts to study anergic T cells must be able to differentiate between strong and weak immune responses. Traditional methods of measuring immune response include surface marker analysis (ki67/CD25/CD69), cytokine analysis (IFN/IL-2), CFSE, and cell cycle count (Suni et al. 2005). While these are effective at measuring proliferation status, they do not directly measure the functional/dynamic state of an immune cell. Measuring the functional immune

response of a T cell can provide useful information about internal signaling or transcriptional events. In this work, the translocation of certain transcription factors will be used to measure a functional immune response. There are many studies that show correlation between strong TCR activation and proliferation status (Smith-Garvin 2009). On the other hand, immuno-compromised T cells can contain many defects in TCR signaling markers and activation (Schwartz 2003; Blackman et al. 1991; Poltorak et al. 2013). Cells can encode various analog parameters to modulate their own activation, which can include factors such as intensity of nuclear translocation, response time, duration, and number of oscillations (Covert 2011). Nuclear import is regulated by the phosphorylation of various proteins (Nardozzi et al. 2010).

All the above are reasons why functional information about a cell state is more informative than static measurements of overall gene/receptor expression. Knowledge of the internal signaling pathways of a cell can provide crucial information in understanding new drug interactions. In the pursuit of developing a better type of screening assay, our approach focused on measuring dynamic localization of transcription factors during drug responses. A high content screening assay based on biomarker localization should result in more accurate drug discovery, better understanding of underlying mechanisms, and fewer false positives and wasted effort on ineffective drugs.

5.1.2 Overview

We present the following assays in order of biological importance with respect to the immune checkpoint pathway. Initial assays focused on the events immediately preceding and following TCR ligation/activation (0–40 min after activation). This is important as a test of feasibility in differentiating between subtle phenotypes using the PMC. More importantly, the translocation of transcription factors NF-kB and NFAT occur during this 0–40 min time frame. After confirming successful detection in a Jurkat cell line, assays were repeated using primary T cells. Many difficulties had to be addressed due to the issues mentioned previously in Chapter 2.3. After validating our methods in primary cells and adjusting them accordingly, we created a protocol to systematically test multiple drug responses of immuno-compromised cells. We started by artificially inducing PD-1 expression in primary T cells. Then, we created separate positive and negative control populations in order to compare relative drug responses from multiple drug candidates. The primary drug we wanted to investigate was anti-PD-1, an immune checkpoint blockade drug that has shown potential in recent clinical trials. Immune checkpoint blockade treatment should partially or fully restore cells from an immuno-compromised state. A successful drug response would be expected to resemble cells from a healthy population (negative control), instead of an anergic population (positive control).

5.2 T cell activation/capping

In general, T cell activation events occur during every immune response so we decided early on that this should be the first pathway to investigate. In addition, we hypothesized that the functional state of the activation pathway should indicate proliferation status (healthy vs. anergic).

Although our final goal was to probe drug responses from primary human cells, it is standard to first validate an assay in a relevant cell line or animal model. Jurkats are naturally suited for this task. Much of what we know about T cell activation signaling is the work of Arthur Weiss on Jurkat cell lines. Also, detecting the capping phenotype would validate the ability of the PMC to measure spatial localization. In a standard non-imaging flow cytometer, capping is undetectable as the overall number of TCRs do not change, only the spatial phenotype changes.

5.2.1 Methods

Cells were labeled with primary antibodies against CD3 (eBioscience #14-0037, OKT3 clone, 5 μg/mL) and CD28 (eBioscience #16-0289, CD28.2 clone, 2.5 μg/mL), on ice; secondary antibodies are added to crosslink primary antibodies (Invitrogen anti-mouse IgG #A16074, 20 μg/mL). Capping was induced by submerging samples in 37˚C water bath for 0 to 20 min. The negative control (0 min) remained on ice and was fixed immediately without any induction. Cells were removed from the water bath at 2 min, 5 min, and 20 min time points. The reaction was stopped and fixed by addition of 1 mL of ice-cold PBS with 100 μl of 37% formaldehyde (10 min at 25˚C).

Secondary antibodies were conjugated with a single dye, Alexa 488, so only one PMT channel (features are represented with PMT2 suffix) was used. Cells are imaged as described in Chapter 3. Features are calculated as described in Chapter 4 and are compiled into histograms below. KS-statistics are generated between positive and negative controls and visualized as a heatmap for easier analysis. For validation, cells are imaged using standard 2-D widefield microscopy.

5.2.2 Results

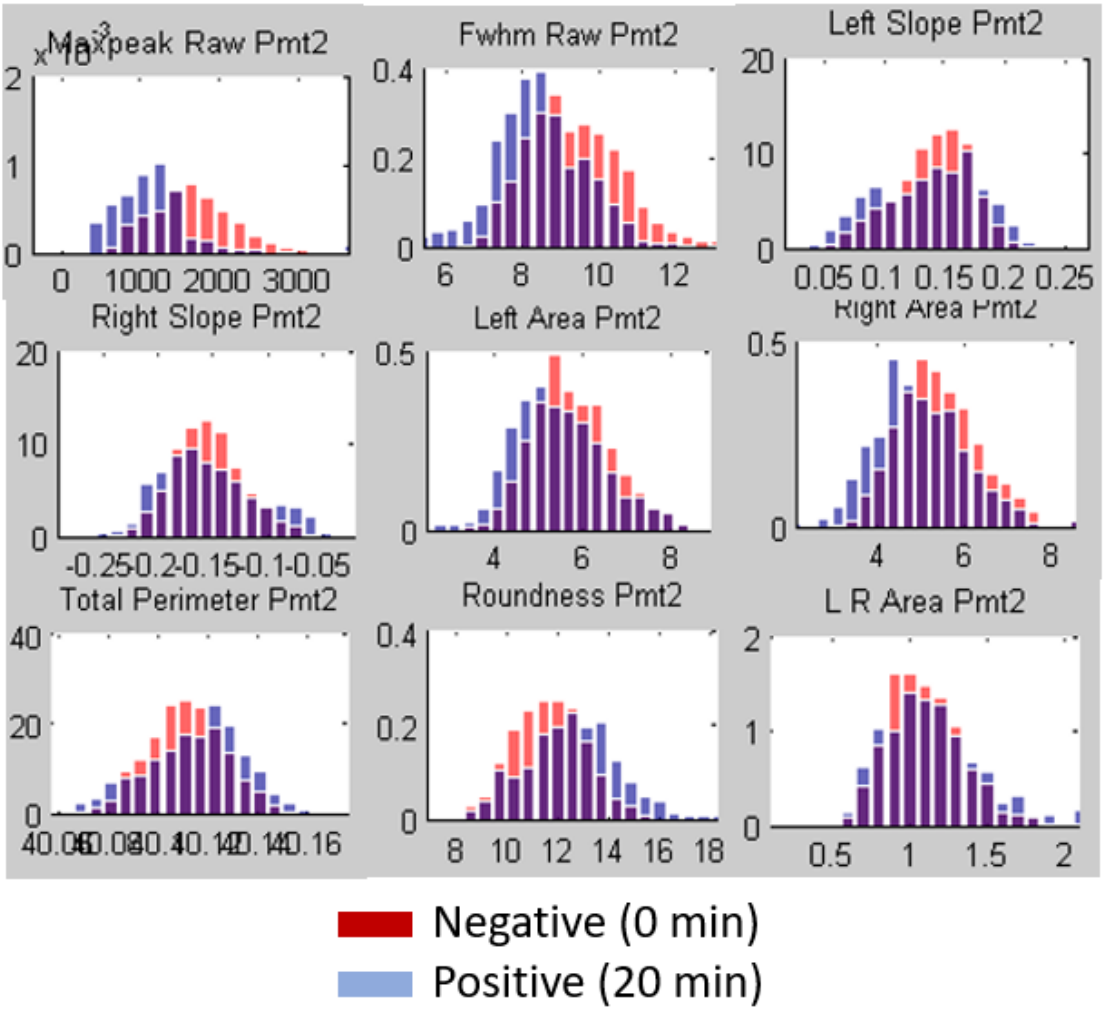

Figure 5-1. Histograms for selected features from Jurkat capping experiments.

Red is negative control (0 min induction), Blue is the positive control (20 min after induction). Nine features are chosen as a representative set to demonstrate the overall shift in features. X-axis for each feature is unique for each feature as none of the features are normalized. Y-axis is the total cell counts for the histogram. PMT 2 is the green PMT channel that indicates CD3 spatial location (Alexa 488). The shift in distributions are indicative of underlying spatial changes in phenotype.

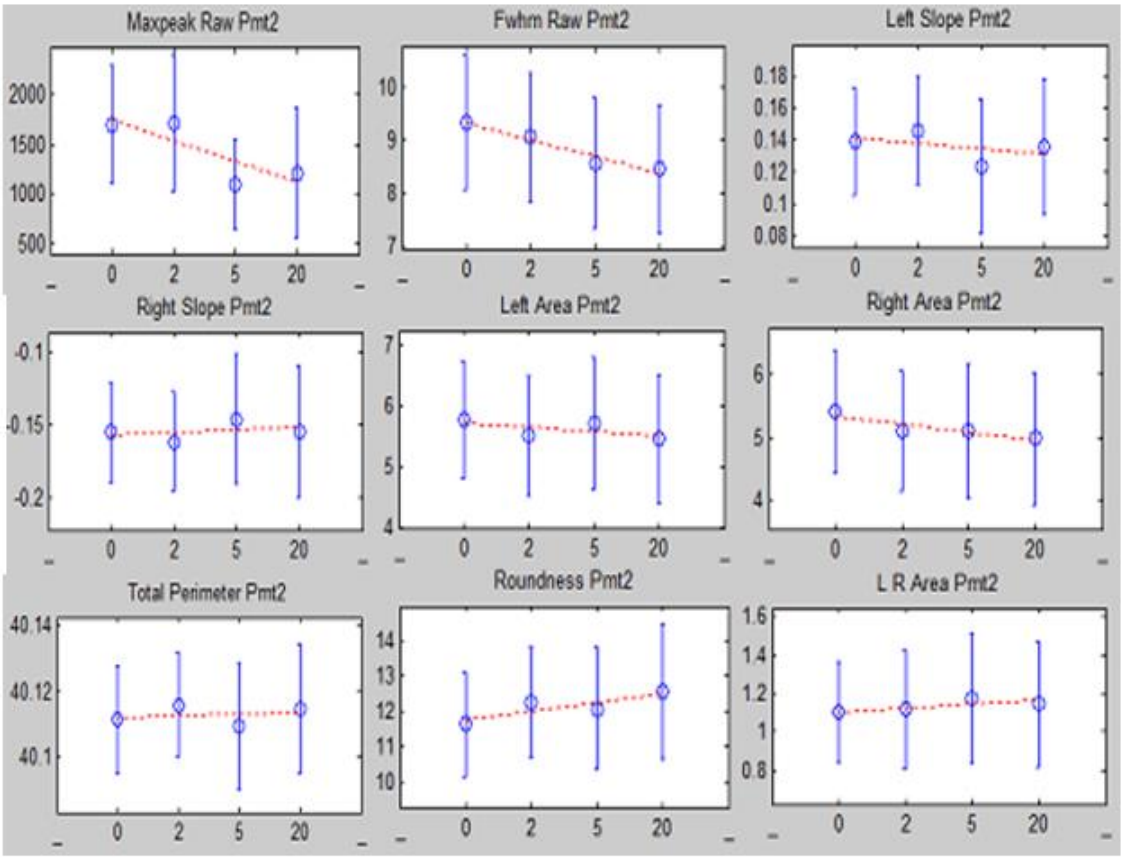

Figure 5-2. Temporal plot for selected features during capping.

Each plot shows the shift in feature means over time, 0–20 min. All features are the same as in Figure 5-1 to show the relative temporal shifts. A linear regression line is fitted to each set of feature means. The trend line shows the general trend of how the features are evolving over time and are consistent with the trends in Figure 5-1. Vertical bars represent the SD from each feature histogram (200–300 cells).

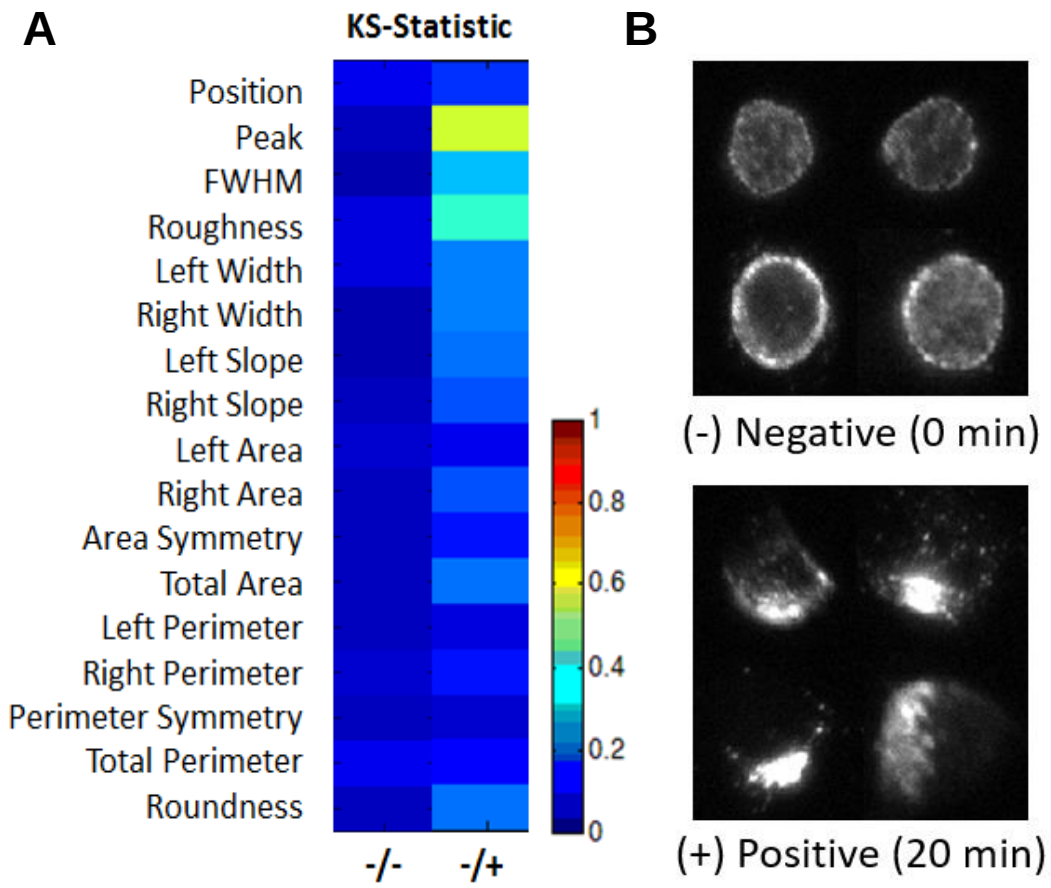

Figure 5-3. PMC data for TCR capping response in Jurkats.

A) KS values from representative features indicate the strength of separation between the positive and negative controls, in this case, (-/-) is the distance between negative and negative. As expected, there should be little to no separation between negative controls. For the (-/+), the negative control at 0 min is compared to the capping phenotype at 20 min. Higher KS for peak, FWHM, roughness, area, and roundness indicate higher separation. B) Representative 2-D fluorescent images taken at 1000ms exposure, 40x magnification, 488nm/530nm ex/em filters. Top image shows diffuse distribution of T cell receptors. Bottom image shows aggregated TCR complexes, the phenotype associated with capping.

The 2-D microscopy images from Figure 5-3B show surface redistribution of TCR complex at both cell rest and 20 min after induction. Histograms from selected features are shown in Figure 5-1. Shifts in the feature distributions indirectly

represent changes in the underlying capping phenotype. Both peak intensity and full width at half maximum (FWHM) decreased slightly. The reduction in overall intensity was unexpected. Since the aggregated of TCR complexes contain the same number of receptors but in a smaller area, it was expected that the average intensity should have increased. This discrepancy may be due to the size of the laser spot. The laser is a 2 μm wide beam that scans only a small portion of the whole T cell. If the fluorescence is localized to smaller areas on the surface, it can be missed or only partially scanned in the case of diffuse receptor distribution. Another possibility could be endocytosis of TCR receptors. After the initial immune synapse, the TCR is downregulated and sequestered within the cytoplasm, this may lead to a reduction in overall fluorescence.

On the other hand, width and area features behaved as expected. Capping of the TCR should result in smaller pockets of fluorescence, and therefore should lead to statistically 'thinner' 1-D images. For both slope and perimeter, there were subtle changes in the overall shape of the distributions but the connection to actual biology is difficult to explain. Also noticeable was that most of the symmetry based features showed little to no changes in distribution. This is reasonable due to the randomness of the cell orientation during imaging. Any features related to the internal symmetry within a cell would be lost when summed across an entire population. In Figure 5-2, the means from each feature were plotted as a function of time. These plots confirm the same trends within the data as compared to Figure 5.1.

Because of the lack of normality in the feature distributions, the KS statistic was used to quantify the separation between negative and positive samples. The KS statistic was calculated from both negative vs. negative and negative vs. positive. The results are plotted as a heatmap for better visualization in Figure 5-3A. In the negative vs. negative column (-/-), features showed no significant differences between samples (p-value data not shown). However, for the negative vs. positive capping response (-/+), many of the features showed highly significant differences (p-values are not shown). Even though early algorithms did not use normalized features, the results from the capping experiments was a strong indication that the PMC could detect changes in spatial localization with high statistical significance.

5.3 NF-kB Translocation

Next we chose to measure NF-kB translocation in Jurkat cells. NF-kB is a critical transcription factor that translocates to the nucleus shortly after T cell activation/capping. It is involved in many signaling pathways that are crucial to T cell regulation and proliferation (Gerondakis & Siebenlist 2010). TCR activation, Toll-like receptors, cytokine receptors can all trigger NF-kB translocation. Measuring the spatial phenotype of a transcription factor is more informative of immune state than measuring surface receptor distribution. Since our primarily goal is to test the functional response of T cells, it makes sense to directly track the movement of important signaling molecules after initial T cell activation. Compared to TCR capping, translocation of NF-kB should be harder to detect as the nuclear

compartment is relatively large in T cells. This should help validate the ability of the PMC to detect more subtle changes in spatial localization within small suspension cells.

5.3.1 Methods

The protocol to induce NF-kB translocation is very similar to capping. The main difference is the duration of the stimulus and the proteins being labeled. Cells were resuspended in 1.5-mL tubes in 100 μL of C10 media for 30 min on ice. C10 media is RPMI 1640 (Invitrogen #12633-012) supplemented with HEPES, Glutamax, antibiotic/antimycotic, and 10% fetal bovine serum (FBS). For the positive control, a two-step TCR crosslinking was used, 5 μg/mL mouse anti-CD3 OKT3 (eBioscience #16-0037) and 2.5 μg/mL mouse anti-CD28 (eBioscience #16-0289) were added and incubated with the chilled cells for 30 min on ice. Negative controls used unlabeled mouse IgG isotype control in place of primary antibodies. Goat anti-mouse IgG (20 μg/mL, Invitrogen #A16074) was added to both controls and allowed to crosslink for another 30 min on ice. Both conditions were incubated in a 37˚C water bath for 0–30 min. To stop the translocation response, cells are removed and fixed by adding 10ul of ice-cold 37% formaldehyde. Cells are stained with a polyclonal anti-NFkB p65 (Abcam #ab16502, 1 μg/mL) overnight. Secondary staining was completed with a single color, anti-rabbit IgG Alexa 488 (Invitrogen #A11008) and imaged as described in Chapter 3. Similar to capping, features are generated and presented as histograms. KS-statistics are generated between

positive and negative controls and cells are imaged using standard 2-D widefield microscopy.

5.3.2 Results

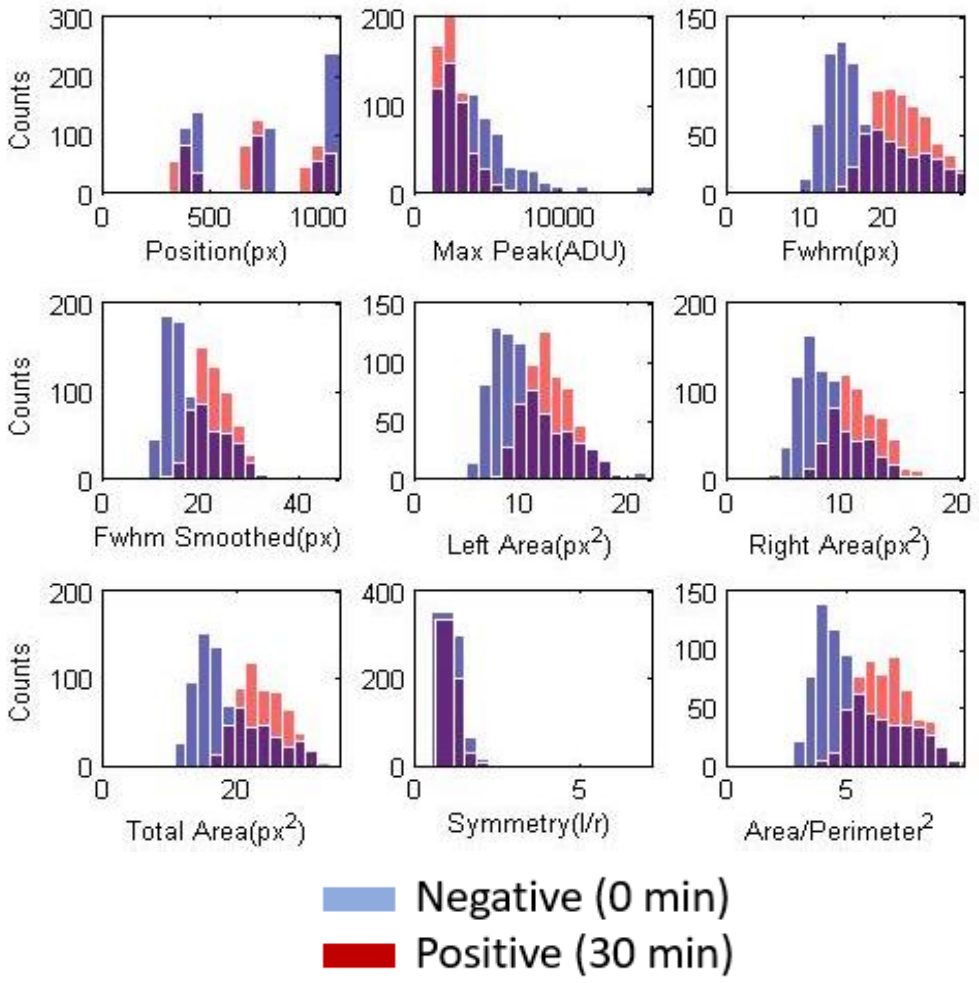

Figure 5-4. Histograms for selected features from NF-kB translocation.

Blue is the negative control which represents resting NF-kB. At rest, NF-kB is contained in the cytoplasm as it is inhibited by IkB. Red is the positive control which represents NF-kB localization after 30 min of induction with CD3/CD28 antibodies. Nine features are chosen as a representative set to demonstrate the overall shift in features. X-axis for each feature is unique for each feature as none of the features are normalized. Y-axis is the total cell counts for the histogram. All features are calculated from the green PMT channel that indicates NF-kB spatial localization (Alexa 488).

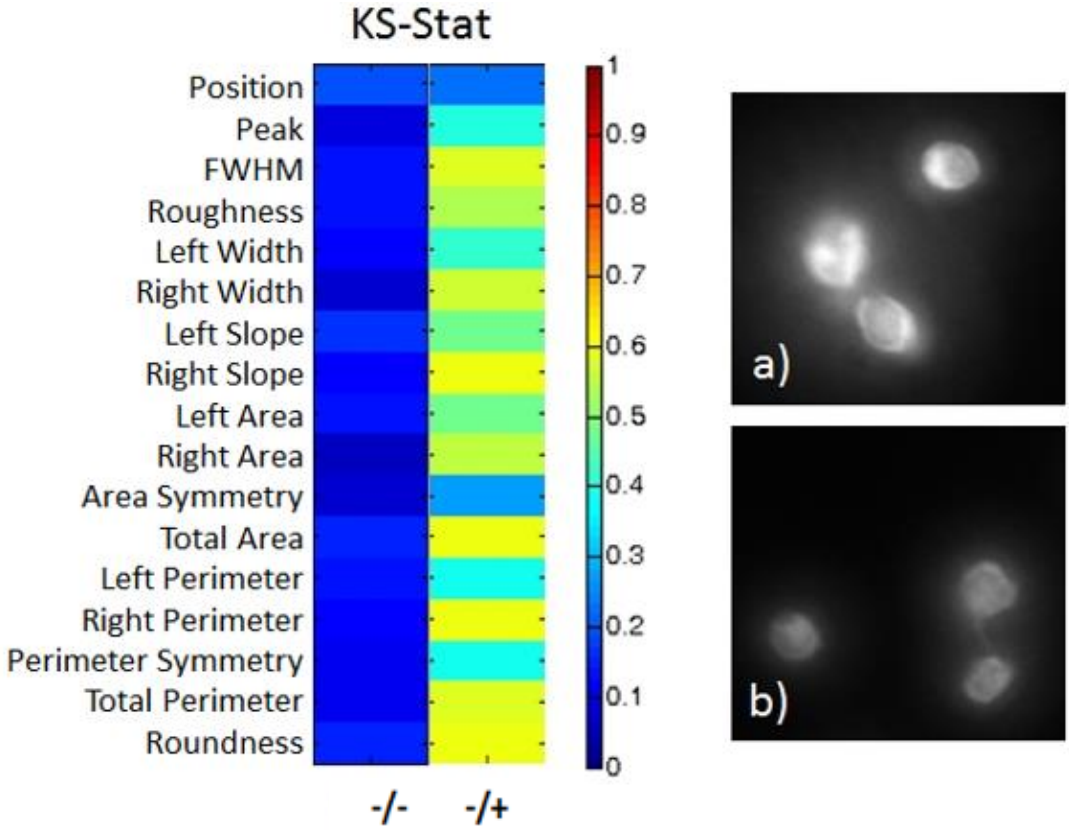

Figure 5-5. PMC data for NF-kB translocation in Jurkats.

Left) KS statistic heatmap for most relevant features. Right) 2-D widefield images using standard fluorescent microscopy (60x, GFP ex/em filter). The upper image is NF-kB at rest. The lower image is NF-kB localization after 30 min. Similar to the data from capping, KS values are visualized as a heatmap. For the (-/+), the negative control at 0 min is compared to the state of NF-kB translocation after 30 min. Surprisingly, the KS values are much higher for all the features when compared to the capping phenotype.

It was initially expected that the width and area features for NF-kB translocation should be lower after 30 min of induction, since in theory, the NF-kB should completely relocate to the nucleus. However, the data showed exactly the opposite. The width (FWHM) of the translocation response actually increased, while overall peak intensity decreased (Figure 5-4). Other features such as area, roundness, and perimeter all showed significant increases in overall values. This change in

phenotype was confirmed with 2-D microscopy (Figure 5-5). It was observed that translocation of NF-kB led to a more uniform concentration of NF-kB across the cytoplasmic and nuclear compartments. After searching the literature, it was found that the cytoplasm to nuclear ratio (C/N) does not go from 1 to 0, but more like 1 to 0.5 (Beg et al. 1993; King et al. 2011). While it is possible that the uniform phenotype we saw could be a result of staining errors, the more likely explanation is that soluble CD3/CD28 induction of NF-kB *in vitro* is weaker than true physiological induction. This makes sense as the protocol does not use antigen-specific TCR ligation, but instead binding to the CD3 peptide chain that is connected to the TCR.

Another interesting observation is that the NF-kB translocation resulted in higher separation between positive and negative phenotypes. This is demonstrated by the larger KS values obtained from the feature distributions (Figure 5-5). One possible reason is that there are many more molecules of NF-kB than TCR receptors. This indicates a higher volume of NF-kB fluorescence compared to TCR fluorescence. In addition, NF-kB is a molecule that is evenly distributed throughout the entire cytoplasmic volume. Volumetric spatial changes should be relatively more pronounced than surface redistribution changes. No matter the underlying cause, these experiments reinforced the choice to use translocation of transcription factors for our functional readout of T cell dynamics.

5.4 Transition into primary cells

Once we confirmed that NF-kB translocation could be strongly detected with the PMC, the next step was to repeat all the experiments in primary cells. TCR capping is not as physiologically relevant for drug response assays, compared to NF-kB translocation, so it was decided that future assays would strictly use NF-kB as the readout. As mentioned in Chapter 2, the use of PBMCs and primary human T cells has additional challenges. Cells purified from peripheral blood are more heterogeneous than cell lines and can have unknown genetic variations from donor to donor. Therefore, it was important to purify as many T cells as possible from a single donor. We decided to isolate both CD4+ and CD8+ T cells from each donor. This allowed for the maximum number of T cells purified from a single donor with minimal effect on heterogeneity. As for the NF-kB induction, T cell activation using CD3/CD28 should be identical in primary T cells.

5.4.1 Methods

Before inducing NF-kB translocation, the first step was to obtain purified primary human T cells. Buffy coat collars were obtained from adult human blood donors from Boston's Children's hospital. RosetteSep CD3+ negative selection enrichment cocktail (Stemcell #15021) was added at a ratio of 50 µL of antibody cocktail to each mL of whole blood then incubated for 30 min at 25˚C. Samples were diluted with equal parts PBS + 2% FBS (Invitrogen #10082-139), then combined with DM-L

density gradient (Stemcell #15705) into 50 mL SepMate tubes. Tubes were centrifuged at 1200*g*, and supernatant was collected. Cells were combined with aluminum chloride for 10 min at 25˚C to lyse red blood cells. Freshly purified cells were frozen immediately in standard freezing media (10% DMSO, 90% FBS) at 2 x 10^7 cells/mL density and maintained in liquid nitrogen.

Cells were characterized to consist of roughly 95% CD3+ cells: 50% of those were CD4+ and the other 50% were CD8+. Cell viability was confirmed to be >95% with trypan blue and a manual hemocytometer (data not shown). On average, 50–150 million purified CD3+ T cells were obtained from each individual donor. Each experimental condition needed about 1 million cells, taking into account cell loss due to staining and washing steps. After performing the assay, each sample could be imaged up to 125 replicates with our reduced PMC volume requirements.

The protocol for NF-kB translocation in primary T cells was nearly identical to that of Jurkats. Cells were resuspended in 1.5-mL tubes in 100 µL of C10 media for 30 min on ice. For the positive controls, a two-step TCR crosslinking was used, 5 µg/mL mouse anti-CD3 OKT3 (eBioscience #16-0037) and 2.5 µg/mL mouse anti-CD28 (eBioscience #16-0289) were added and incubated with the chilled cells for 30 min on ice. We used additional compounds to induce NF-kB translocation. These were substituted in place of the standard CD3/CD28 antibodies: 200 ng/mL of TNFa, 10 µg/mL of Phorbol 12-myristate 13-acetate (PMA) + 10 mM of Ionomycin, 10 µg/mL of Phytohaemagglutinin (PHA), 10 µg/mL Lipopolysaccharide (LPS), and 1 µg/mL Staph Endotoxin B were all tested as NF-kB induction compounds.

Negative controls used unlabeled mouse IgG isotype control in place of primary antibodies. Goat anti-mouse IgG (20 μg/mL, Invitrogen #A16074) was added to all samples and allowed to crosslink for another 30 min on ice. All conditions were incubated in a 37˚C water bath for 0–30 min. To stop the translocation response, cells are removed and fixed by adding 10ul of ice-cold 37% formaldehyde. Cells are stained with a polyclonal anti-NFkB p65 (Abcam #ab16502, 1 μg/mL) overnight. Secondary staining was completed with two colors, anti-rabbit IgG Alexa 488 (Invitrogen #A11008) for the green PMT channel and PI for the red channel. PI and RNase A were added to the mix and incubated for 30 min at 37˚C to serve as a nuclear counterstain to NF-kB. Cells are imaged using widefield fluorescent microscopy. Feature distributions for the highest-ranking features are displayed as cumulative distribution functions.

5.4.2 Results

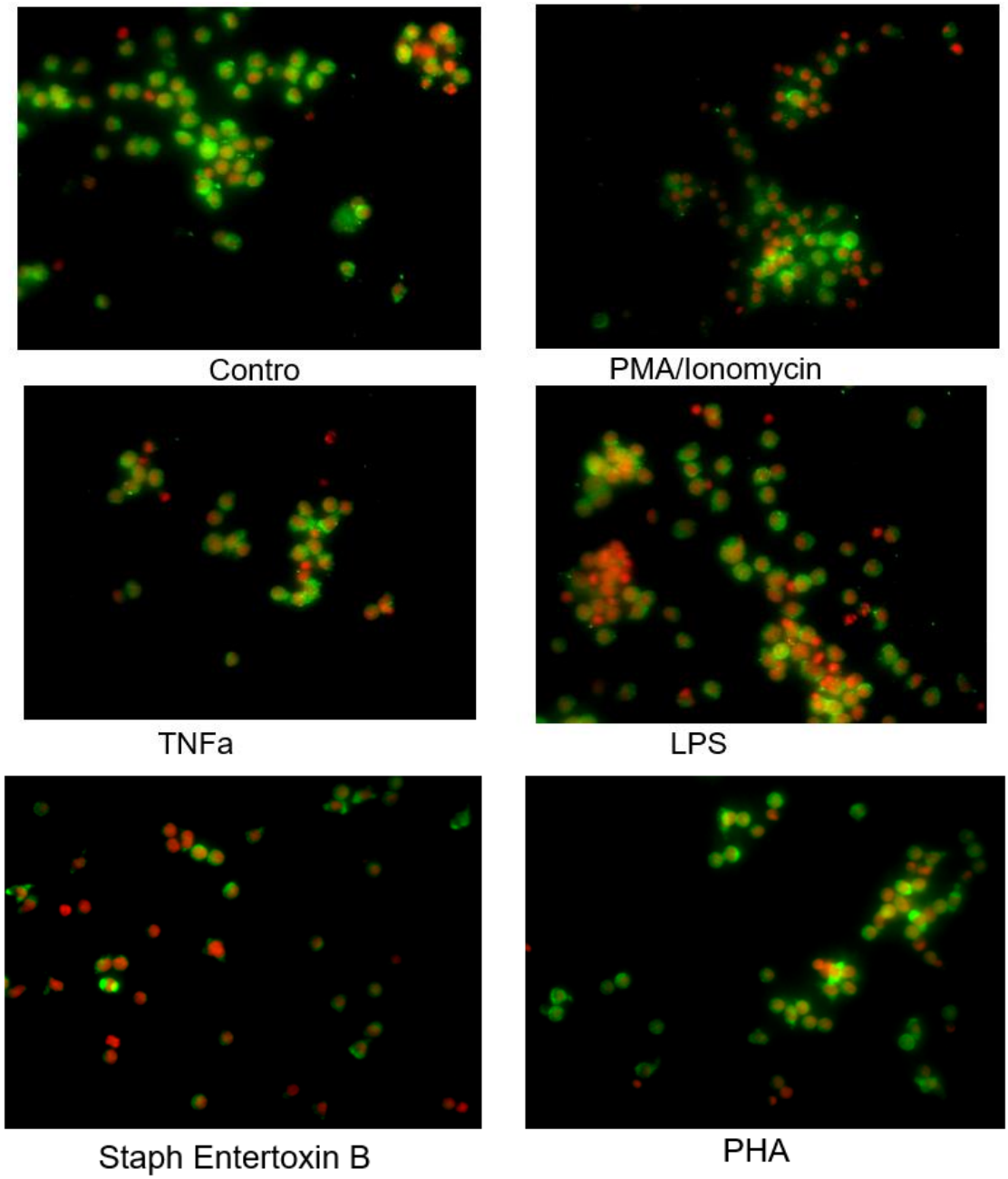

Figure 5-6. 2-D microscope images of various NF-kB induction methods.

The induction stimulus is labeled underneath each image. Control represents NF-kB translocation using standard CD3/C28 antibodies. Green color is anti-NF-kB conjugated to Alexa 488. Red is propidium iodide (PI) for the nuclear stain. The images here shown mainly failed NF-kB translocation in all induction methods. For a successful NF-kB translocation phenotype, the green channel

(NF-kB) should overlap with the red channel (PI) which indicates that the NF-kB p65 homodimer has diffused into the nuclear compartment. In each image, the opposite occurs. The NF-kB remains contained in the cytoplasmic compartment, this can be seen by a large empty circle in the green channel.

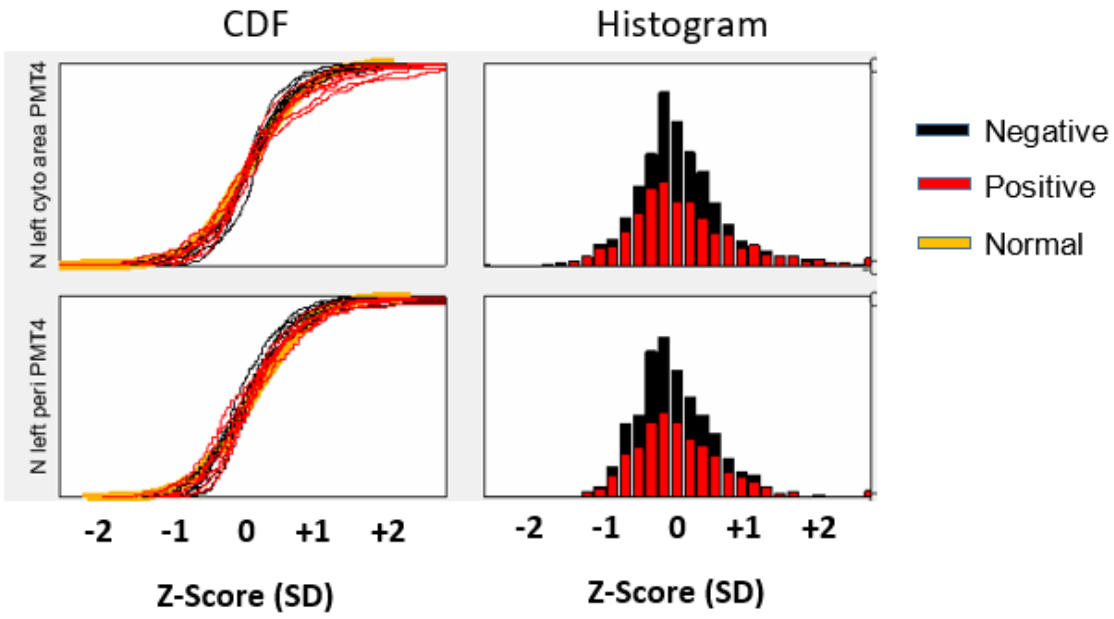

Figure 5-7. Cumulative distribution function and histogram for the highest separated features from NF-kB translocation in primary T cells.

CDFs for the control induction of NF-kB in primary T cells. The two features listed above (Left Cyto Area and Left Perimeter) had the highest difference in mean statistics, but showed no significant changes between negative and positive samples. Each red line is a separate replicate sample from the positive NF-kB induction (30 min). Each black line is a separate replicate sample from the negative NF-kB induction (0 min). A quick glance at the shifts in feature distributions between negative and positive samples shows that NF-kB translocation in primary T cells was minimal. CDFs are represented as histograms on the right for an alternative visual.

Unfortunately, NF-kB translocation did not respond similarly in primary cells when compared to Jurkat cells. Even after testing with multiple induction compounds, none of the primary cells showed any clear translocation response. We performed multiple experiments in an attempt to strengthen the NF-kB translocation response.

For example, we tried expanding the T cells first, and then inducing NF-kB translocation but the results were the same. Microscopy confirmed a lack of observable changes in spatial localization of NF-kB (Figure 5-6). This was also confirmed in the data analysis, the positive and negative feature histograms overlapped completely with almost no separation (Figure 5-7). The CDFs also showed little to no change in the mean statistic. The corresponding KS and p-values were also near zero (data not shown).

The lack of a translocation response was unexpected as other research groups have successfully induced NF-kB translocation in primary T cells and confirmed their results with western blots (Lupino et al. 2012). However, looking closer at the literature, most protocols involve stripping the cytoplasm from the cell, and only measuring nuclear concentration of NF-kB (Beg et al. 1993). It is much more sensitive to measure pure NF-kB accumulation in the nucleus since it starts at zero. Other protocols compare phosphorylated IkB/NF-kB. Since western blots separate proteins based on molecular weight and charge, the difference between IkB-NF-kB and NF-kB is much more pronounced. After talking to colleagues in the Biology department, there was further support that NF-kB translocation is in fact much weaker in primary cells (Gilmore & Gerondakis 2011). The C/N ratio goes from 1 to 0.9, as opposed to Jurkats, where the C/N goes from 1 to 0.5. Because the spatial phenotype is so weak in primary cells, most people avoid using microscopy to measure NF-kB translocation. Since NF-kB translocation spatial phenotype was too subtle to be detected in the PMC, an alternate method had to be found.

5.5 NFAT translocation

Because the NF-kB translocation response was undetectable in primary T cells, we had to find a new biomarker for the PMC assay readout. Nuclear Factor of Activated T cells (NFAT) was chosen for its relevancy in T cell activation (Smith-Garvin 2009). NFAT is also a translocating transcription factor (along with AP-1 and STAT1) that occurs directly after TCR ligation. One crucial difference from NF-kB is that NFAT translocation occurs much faster (Poltorak et al. 2013). NFAT is also not as ubiquitous in other signaling pathways.

5.5.1 Methods

The protocol for NFAT translocation was similar to NF-kB translocation but had some key differences. Two methods were used: the first approach used standard CD3/CD28 antibodies to bind to the TCR as described in 5.3.1, the second approach used PMA/Ionomycin to trigger NFAT translocation. NFAT translocation involves the activation of calcineurin and calcium signaling. Therefore, PMA/Ionomycin can be used to artificially induce NFAT translocation while bypassing the TCR activation pathway. This served as a useful control against the standard CD3/CD28 activation in case unexpected phenotypes occurred.

Cells were incubated on ice as before, but 10 mM of ionomycin (Sigma # I0634) and 1 μg/mL phorbol myristrate acetate (PMA) (Sigma #P8139) were used instead of CD3/CD28 antibodies. The positive sample was similarly placed in a 37˚C water bath for 20 min to induce translocation of NFAT and fixed with the same

protocols. For the primary antibody, rabbit anti-NFAT1 (CST #4389, 2 μg/mL) was added and incubated overnight at 4˚C. Then, secondary anti-rabbit Alexa 488 (Invitrogen #A11008, 10 μg/mL), 1:100 PI, and 20 μg/mL of RNase A were added to the mix and incubated for 30 min at 37˚C. The PI and RNase provide a nuclear counterstain against the single green channel of anti-NFAT Alexa 488. Using a counterstain allows features to be normalized against themselves and is more resistant to differences in staining and biological variance. We specialized to two-color assays from this point on, as we discovered that PMT-to-PMT comparisons are intensity independent and easier to normalize.

During these experiments, we pushed our instrument to higher sample throughput. Lack of sample throughput is a significant limitation that is preventing adoption of 2-D imaging cytometry and primary cell assays in drug screening (Zanella et al. 2010; Eglen & Reisine 2011). With screening libraries up to millions of compounds, a single large scale screen can cost hundreds of millions of dollars for reagents. This is why throughput, volume requirements, data storage are all important when developing a screening assay. Volume and data requirements have already been addressed in previous chapters. One of the goals of the PMC is to help develop screening assays, so the PMC must be adapted to high throughput operation.

Each induction method (PMA/Ionomycin and CD3/CD28) was applied to a large population of naïve primary T cells. Each approach was imaged in the PMC to simulate a 96-well plate: 48 negative controls and 48 positive controls were

obtained for each induction method. This is similar to a standard 50/50 plate assay quality control metric. For this particular data set, only the central 8 lanes were used for all samples. Each chip turnover took about 3 min to finish, 2 min for scanning and 1 min for cleaning.

After collecting all the data from all samples, a separate population of only negative (0 min) and positive (20 min) controls were used to generate the coefficients for the activity score regression model. Instead of generating KS-statistics, activity scores were calculated using those coefficients from the regression model. The activity score represents the relative strength of NFAT translocation compared to the positive and negative controls, and is much more suitable for high-throughput analysis. The selected coefficients (Figure 5-9) were applied to all the samples equally for both induction methods to generate a single activity score for each sample. Z' and SSMD values were used to measure the quality of the induction method and results are presented below. Cells are imaged using widefield fluorescent microscopy for validation.

5.5.2 Results

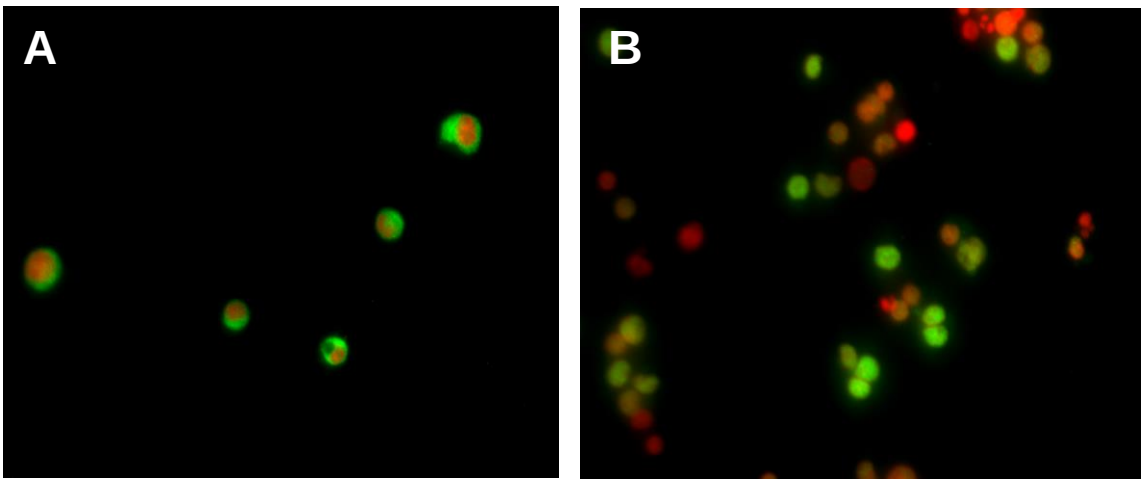

Figure 5-8. 2-D images of NFAT translocation in primary T cells using PMA/Ionomycin induction.

Green is Alexa 488 staining for NFAT1. Red is PI, nuclear counterstain. A) Negative control – Cells at rest (0 min) that have mostly cytoplasmic NFAT. There is a strong distinction between cytoplasmic and nuclear fluorescence. B) Positive control – Cells that have been induced for 20 min. NFAT has diffused into the nuclear compartment so there is more overlap between green and red PMT channels.

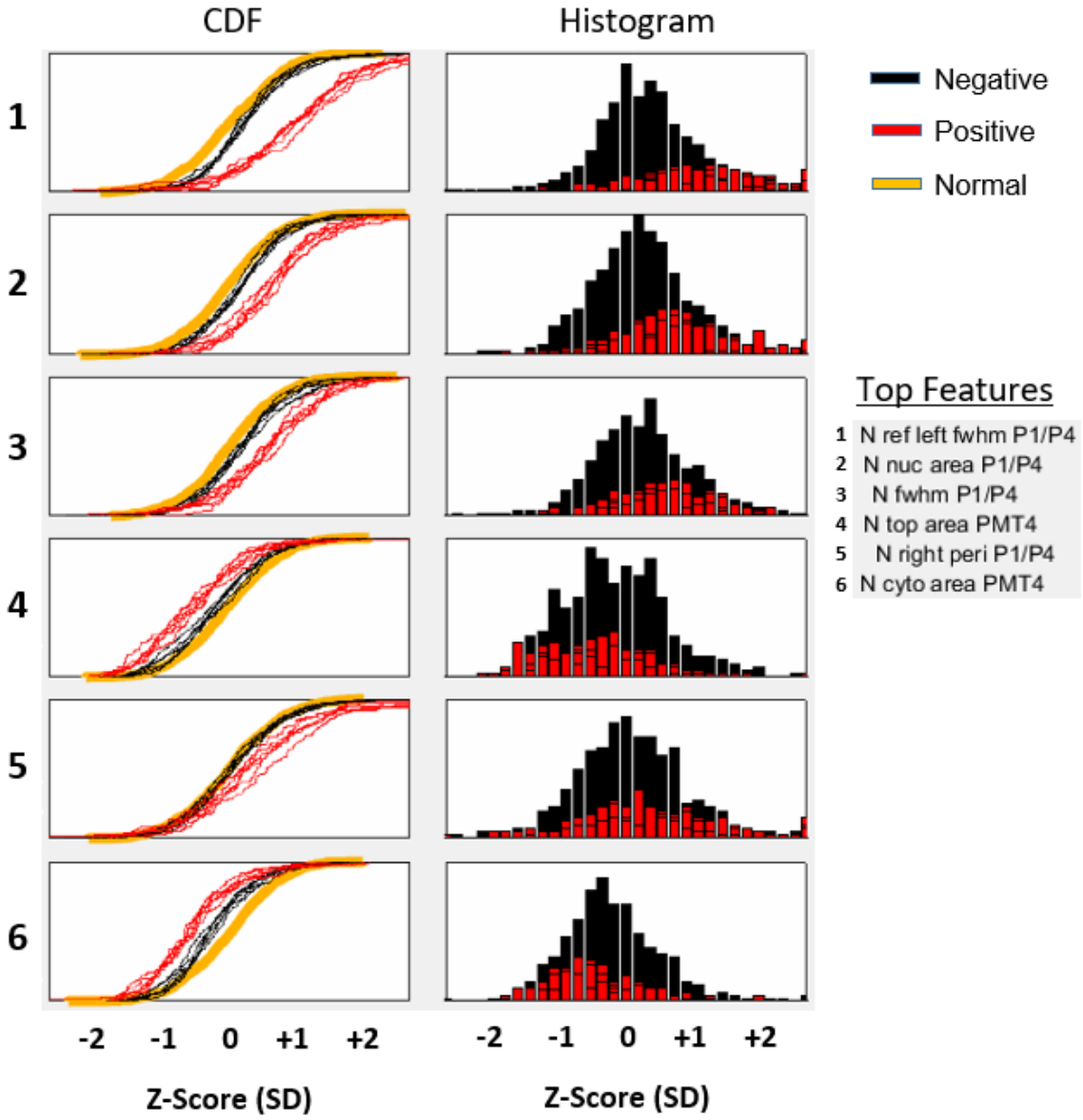

Figure 5-9. CDFs for selected features that are highly separating between negative and positive NFAT translocation in primary T cells.

CDFs and corresponding histograms for the top 6 features as selected by the regression model. Each red line (N=8) is a separate replicate sample from the positive NFAT induction (30 min). Each black line (N=8) is a separate replicate sample from the negative NFAT induction (0 min). The features and their corresponding coefficients were used to create an activity score model and applied to all samples. Visual inspection shows significant shifts in the mean statistic. P1/P4 represents the ratio of the features between the red nuclear channel (PMT1) and the green NFAT channel (PMT4).

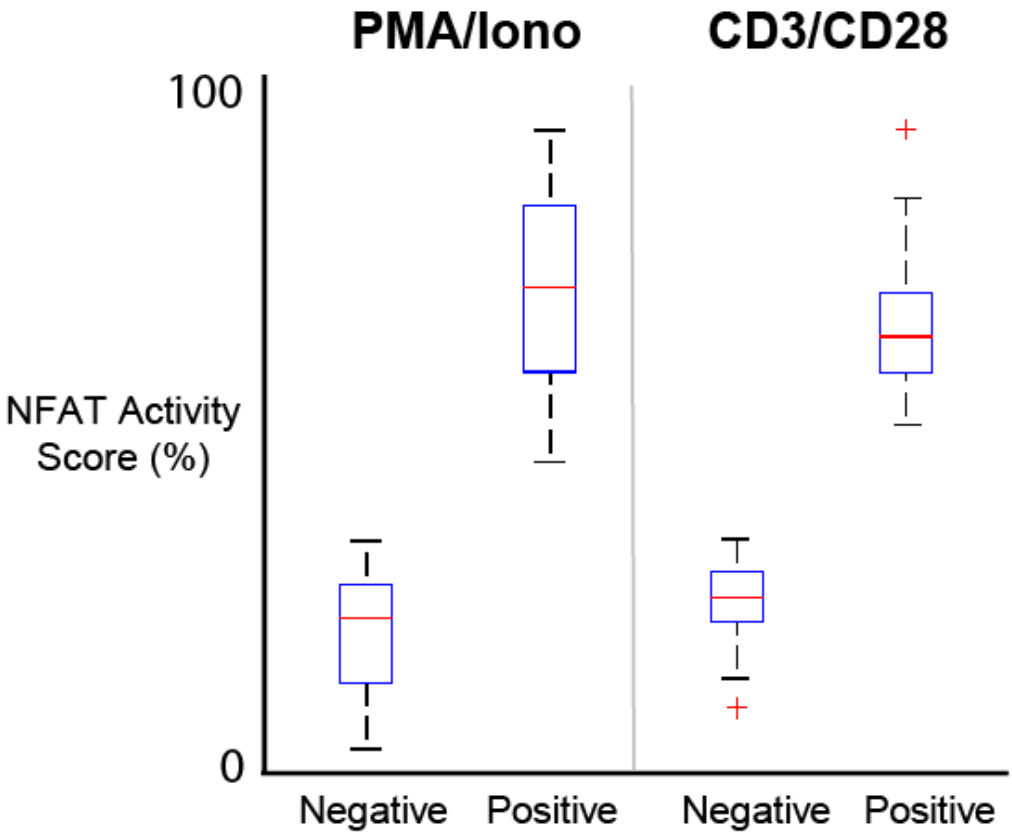

Figure 5-10. Activity score box plots for both PMA/Ionomycin and CD3/CD28 activation of NFAT translocation in primary T cells.

Each box plot contains 48 replicates of the experimental condition. Activity scores are calculated for each replicate using the logistic regression model described in Chapter 4. Negative represents the NFAT translocation phenotype at time 0 min. Positive represents the NFAT translocation phenotype after 20 min. The Y-axis Activity Score is a percentile from 0 to 100th. Image from (Wang & Ehrlich 2017).

We used PMA/ionomycin as a control to CD3/CD28 activation to induce maximal NFAT translocation for a duration of 20 min in primary T cells. The negative control was created by omitting PMA/ionomycin. The cells were imaged and processed using the automated statistical workflow. The top discriminating features are shown in Figure 5-9. These features were selected based on the maximum separation between all the cumulative distribution functions (CDFs) of the negative and

positive controls using the previously described mRMR approach. These features were used as the input to the activity score logistic regression model. The model was then applied to each sample. Each sample produces a single overall 'activity score' which is a linearly weighted combination of the feature means and their corresponding coefficients (Figure 4-8). Activity scores are represented by cumulative box plots shown in Figure 5-10.

Figure 5-8 shows the 2-D fluorescent images of each NFAT sample. It was observed that the NFAT translocation phenotype was qualitatively stronger in primary T cells. The negative NFAT phenotype showed a clear boundary between cytoplasmic NFAT and nuclear PI, indicating a lack of translocation. The positive NFAT phenotype showed the opposite, much more overlap between NFAT and nuclear PI fluorescence.

We evaluated the strength of the NFAT translocation readout using standard assay quality control metrics, the strictly standardized mean difference (SSMD) and Z' were calculated for each induction method. Comparing Z' and SSMD values allows us to analyze the high throughput capabilities of our technology. For the PMA/Ionomycin induction (Figure 5-10 Left), the Z' = -0.39 and the SSMD = 2.92. While these numbers are not strong enough for a large scale primary screen, an SSMD of 3 is still acceptable for assays with weak positive controls (Bray & Carpenter 2004). As mentioned in Chapter 3.1.2, most of our variance comes from reproducible differences between parallel lanes — primarily optical aberrations across the scan field. We redid the analysis but modeled each lane individually. By

treating each lane separately, we remove any effects to lane-to-lane variance. The results are present in Figure 5-11. We achieved an average Z' of 0.55 and SSMD = 12.98, which is very reasonable for a high throughput primary screen.

	PMA/Ionomycin		CD3/CD28	
Lane #	**Z'**	**SSMD**	**Z'**	**SSMD**
All	-0.39	2.92	0.03	4.28
1	0.68	13.17	0.81	19.90
2	0.83	20.89	0.82	22.59
3	0.64	9.70	0.79	18.03
4	0.87	32.09	0.91	52.37
5	0.66	10.00	0.77	18.50
6	0.49	8.36	0.69	11.07
7	0.46	6.27	0.85	28.92
8	-0.20	3.38	0.54	8.13
Mean	0.55	12.98	0.77	22.44
SD	0.31	8.70	0.11	12.81

Figure 5-11. Z' and SSMD values for both PMA/Ionomycin and CD3/CD28 induction of NFAT translocation in primary cells.

The first row contains the Z' and SSMD values calculated by using the entire pooled data set across all eight lanes of the microfluidic device without lane-to-lane variability removed. The next 8 rows show statistics from each individual lane, with controls calculated for each individual lane to reduce the systematic variability between lanes from optical aberrations. The mean and standard deviation (SD) are calculated for all eight lanes to summarize the distribution of Z' and SSMD values. Table from (Wang & Ehrlich 2017).

At the onset, we expected that the more physiological approach using standard CD3/CD28 antibodies would trigger a weaker NFAT translocation phenotype. This is because compared to ionomycin, which directly activates calcium channels and calcineurin, CD3 ligation is an indirect T cell activation method. Anti-CD3 does not

directly bind to the hypervariable region of the TCR and as a result, should be a weaker NFAT induction. Surprisingly, the separation between the positive and negative controls was greater using CD3/CD28 induction (Figure 5-10 Right). Across all lanes, the Z' = 0.03 and SSMD = 4.28. After removing the lane-to-lane variance, the separation is much more pronounced. The average Z' = 0.77 and SSMD = 22.44 (Figure 5-11), which indicates a very high separation between positive and negative controls with the CD3/CD28. These numbers are more than acceptable for a high throughput primary screen.

5.6 Immune checkpoint anergy assay

The experiments discussed up to this point demonstrate the ability of our technology to detect translocation phenotypes of a critical transcription factor (NFAT) during primary T cell activation. The next step was to investigate the immune response of immunotherapy drugs. We needed to establish a method to generate both healthy and immuno-compromised T cells. By obtaining both a population of healthy and immuno-compromised cells, we could then determine the relative drug response from immune checkpoint blockade.

Because we wanted to study anti-PD-1 drug responses, we started by using PD-L1 to create an anergic population of T cells. When PD-L1 binds to the PD-1 receptor, it triggers a cascade of signaling events that inhibits proximal TCR signaling molecules and leads to anergy (Francisco et al. 2010). Blocking the PD-

L1:PD-1 binding event should prevent anergy, or at least recover the cells from anergy.

5.6.1 PD-1 receptor expression (Primed population)

In order to study the immune checkpoint pathway, one first needs the PD-1 receptor. The PD-1 surface receptor is not natively expressed on resting PBMCs. In order for healthy peripheral T cells to express PD-1, priming is necessary. This involves activating the T cells with CD3 to simulate an antigen binding event and initial T cell activation. Purified naïve primary T cells are introduced to a pre-coated petri dish with immobilized anti-CD3 (OKT3 clone, 5 μg/mL). Cells are incubated in the petri dish for 24 hours at 37˚C. After incubation, cells are aspirated, washed and rested in a separate petri dish with C10 media for 72 hours. Creation of the primed population is summarized in Figure 5-14A. PD-1 receptor staining confirmed successful PD-1 expression (data not shown).

After priming the cells, we also had to confirm that NFAT translocation was still a viable phenotype. It was important to repeat NFAT translocation in primed T cells since it is possible that the pathway is compromised or altered. Previous NFAT translocation experiments were conducted with naïve T cells directly purified from peripheral blood. After priming the T cells and resting for 72 hours, the cells were then removed and secondary TCR activation is applied. After 3 days rest, cells were removed from the incubator and placed on ice as before. For the positive control, a two-step TCR crosslinking was used, 5 μg/mL mouse anti-CD3 OKT3 (eBioscience

#16-0037) and 2.5 μg/mL mouse anti-CD28 (eBioscience #16-0289) were added and incubated with the chilled cells for 30 min on ice. Negative controls used unlabeled mouse IgG isotype control in place of primary antibodies. Goat anti-mouse IgG (20 μg/mL, Invitrogen #A16074) was added to both controls and allowed to crosslink for another 30 min on ice. The positive control sample was placed in a 37˚C water bath for 20 min to induce translocation of NFAT and fixed with the same protocols. For the primary antibody, rabbit anti-NFAT1 (CST #4389, 2 μg/mL) was added and incubated overnight at 4˚C. Then, secondary anti-rabbit Alexa 488 (Invitrogen #A11008, 10 μg/mL), 1:100 PI, and 20 μg/mL of RNase A were added to the mix and incubated for 30 min at 37˚C. Cells are prepared in flow buffer and imaged with the PMC. Activity scores are generated as previously described, a single set of coefficients is generated from a small set of positive and negative controls. The results and relevant coefficients are shown in Figure 5-12. These coefficients are then applied to every sample, 8 replicates from the positive control and 8 replicates from the negative control. Activity scores are displayed as boxplots.

Features are recalculated for the activity score regression model as the negative and positive controls are different from standard unprimed NFAT or NF-kB translocation. Both the Z' and SSMD (2.56) confirmed a high degree of separation for NFAT translocation. This indicates that the NFAT translocation pathway is not compromised in primed cells and maintains a strong spatial phenotype for the PMC readout.

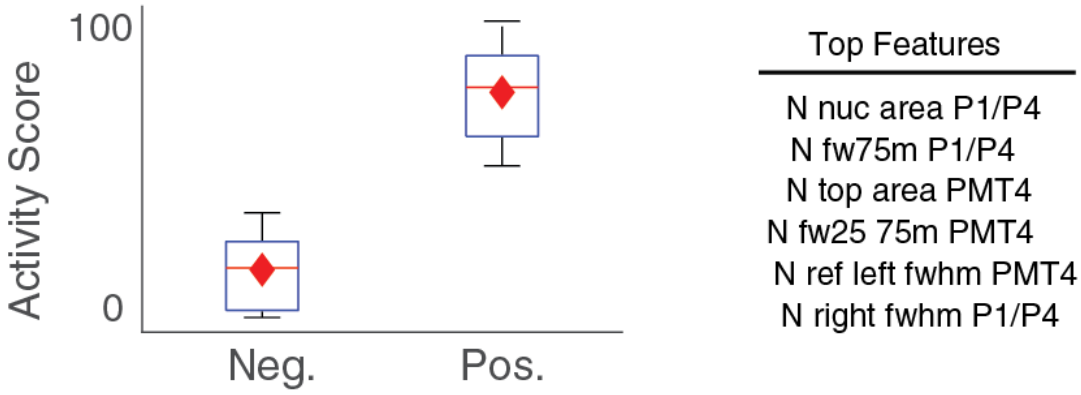

Figure 5-12. Drug activity score box plot for NFAT translocation in primed T cells.

Activity scores (relative %) for NFAT translocation for the primed T cell population. The feature coefficients from the activity score regression model is shown on the right. Each box plot contains 8 replicates. (Neg.) represents the phenotype of resting cells at 0 min. (Pos.) represents the same cells after 20 min induction of NFAT translocation. Red diamond represents the mean, line represents median. SSMD between the negative and positive samples is 2.56 which is reasonable for a weak control.

5.6.2 PD-L1 induction of anergy

After confirming the healthy primed population, the next step was to generate a population of immuno-compromised cells aka the anergic population. Similar to the primed population, cells were incubated in a pre-coated petri dish with immobilized anti-CD3. However, in this case, chimeric PD-L1-Fc (Biolegend #762504, 5 µg/mL) is also immobilized alongside the anti-CD3 (5 µg/mL). Cells are activated and stained identical to the primed population in 5.6.2. After incubation with anti-CD3 and PD-L1-Fc, the T cells are removed and rested for 72 hours. After 3 days rest, cells were removed from the incubator and placed on ice as before. For the positive control, a two-step TCR crosslinking was used, 5 µg/mL mouse anti-CD3 OKT3

(eBioscience #16-0037) and 2.5 μg/mL mouse anti-CD28 (eBioscience #16-0289) were added and incubated with the chilled cells for 30 min on ice. Negative controls used unlabeled mouse IgG isotype control in place of primary antibodies. Goat anti-mouse IgG (20 μg/mL, Invitrogen #A16074) was added to both controls and allowed to crosslink for another 30 min on ice. The positive control sample was placed in a 37˚C water bath for 20 min to induce translocation of NFAT and fixed with the same protocols. For the primary antibody, rabbit anti-NFAT1 (CST #4389, 2 μg/mL) was added and incubated overnight at 4˚C. Then, secondary anti-rabbit Alexa 488 (Invitrogen #A11008, 10 μg/mL), 1:100 PI, and 20 μg/mL of RNase A were added to the mix and incubated for 30 min at 37˚C. Cells are prepared in flow buffer and imaged with the PMC. Cells are imaged in the PMC and activity scores are calculated for each sample.

For the anergic population, the activity score model used the same coefficients generated from the primed population. Since the resulting phenotype is based on similar methods, there is no need to generate a new regression model. Using the same regression model for both primed and anergic populations allows for comparison of relative NFAT translocation between the two populations. The feature selection algorithm is based on the original positive and negative control phenotypes, and is not biased towards any other spatial phenotypes or sample conditions. The addition of PD-L1 in the anergic population should bind to PD-1 receptors and should trigger the immune checkpoint pathway. These T cells should have a functional immune state that resembles anergy when compared to the

activity score NFAT translocation of the primed population. Results are shown in Figure 5-13.

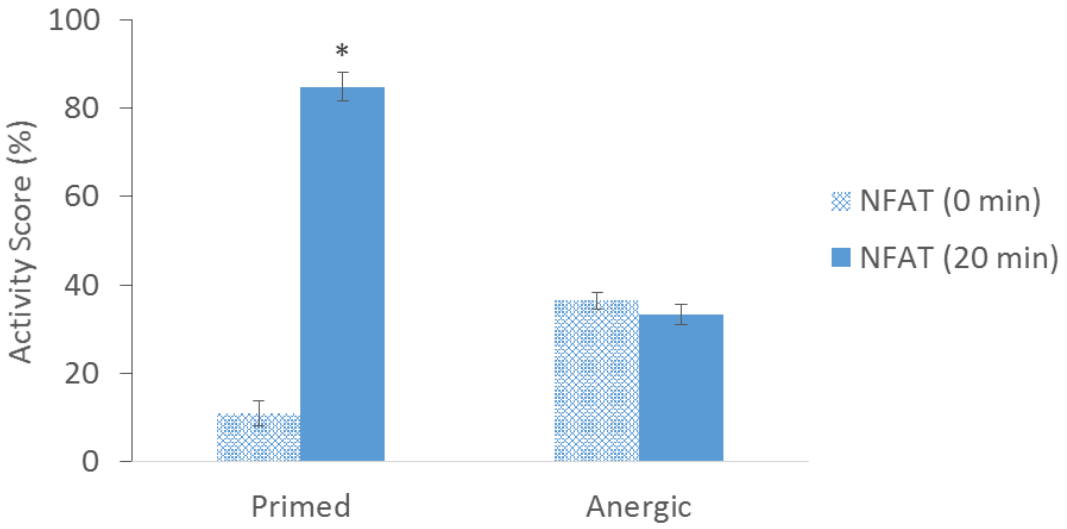

Figure 5-13. Drug activity scores for NFAT translocation in both primed T cells and anergic T cells.

The two bars on the left represent the NFAT translocation response from healthy primed cells (N = 24 each bar). A strong change in phenotype is depicted by the large shift in activity score (normalized to percent activation). Each population is measured at 0 min and 20 min during the NFAT drug response. Bars on the right represent the NFAT translocation response from anergic cells induced with immobilized PD-L1 (N = 24 each). The lack of separation indicates minimal changes NFAT translocation phenotype. *, $p < 0.01$. Error bars indicate standard error.

Anergy is a difficult phenotype to detect functionally as it is a hypo-responsive immune state. Anergy results in the lack of an immune response, signaling pathways such as NFAT/NF-kB are inhibited by the activation of the immune checkpoint pathway. Thus, we needed both primed and anergic T cell populations to measure relative NFAT drug responses.

Figure 5-13 (Anergic) showed that our artificially induced population had insignificant phenotypic changes in NFAT translocation, as indicated by the activity score readout. The results from this experiment provided evidence for the hypothesis that functional immune response is correlated to long term proliferation status. The healthy cell population (Primed) demonstrated a significantly strong NFAT translocation response. A paired student t-Test was applied at $\alpha = 0.01$ to determine significance. Further validation studies are still needed. Verifying with cytokine or cell cycle analysis would help strengthen the hypothesis that NFAT translocation dynamics reflect proliferation status. We repeated the experiment but titrated PD-L1-Fc concentration down to 1 μg/mL. After reducing the PD-L1-Fc concentration, the NFAT translocation phenotype became stronger (data not shown). The results from these experiments provide evidence that T cell activation is correlated to long term proliferation status, as is consistent with the literature (Blackman et al. 1991; Riley 2009).

5.6.3 Drug response relative to Primed and Anergic populations

Now that we have a primed population (healthy cells, positive control) and an anergic population (unresponsive cells, negative control), we began testing the relative drug responses with respect to both controls. A diagram of the three populations is shown in Figure 5-14. This provides the overall structure of the immunotherapy assay.

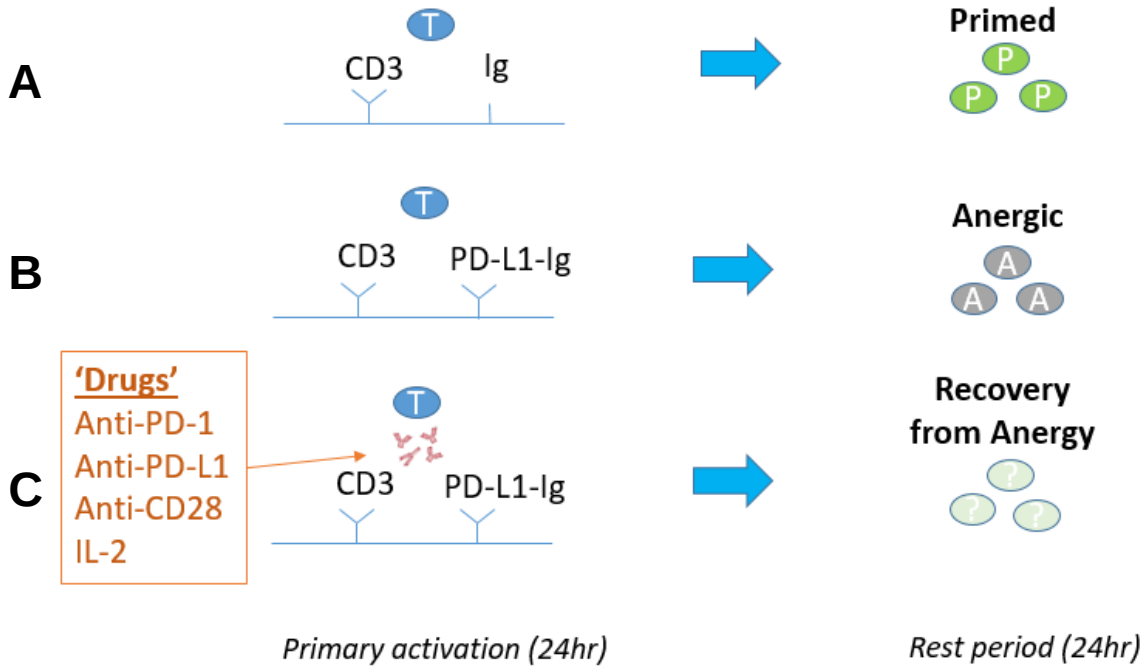

Figure 5-14. Overview of immunotherapy assay setup with primed, anergy, and drug populations.

The creation of each population A, B, and C is described in the methods. The first two populations, primed and anergic, will be used as the positive and negative controls, respectively. A successful drug candidate (C) should recover the cells to resemble healthy cells again (A). Unsuccessful drug candidates will result in a phenotype that is still anergic (B).

The premise of the assay design was as follows: We first established both positive (primed) and negative (anergic) control populations so we could measure the maximum and minimal NFAT translocation response. These two populations were generated exactly as described in the previous two sections. For the third 'drug population, various drugs were added to the population of anergic cells. In this way, one can measure the drug response relative to those two initial control populations (Figure 5-14C).

Similar to the methods from the anergic population, the cells were incubated with immobilized CD3 and PD-L1-Fc. During this time, drug candidates were added simultaneously to the petri dish. Those drug candidates included: anti-PD-1 (J116 clone, 5 μg/mL), anti-CD28 (CD28.2 clone, 2.5 μg/mL), or IL-2 (eBioscience #14-8-29, 500 ng/mL). For anti-CD28, the antibody was immobilized alongside PD-L1-Fc and anti-CD3. For IL-2, the cytokine was added during the 24-hour induction period and refreshed during the 72-hour resting period. Both IL-2 and anti-CD28 candidates have shown to recover/prevent T cells from entering anergy (Shen et al. 2016; Bennett et al. 2003). For anti-PD-1, the antibody drug was added in soluble form at the beginning of the 24 hours incubation. This particular clone J116 has been confirmed to inhibit the PD-1 signaling pathway but does not block the binding of PD-L1 (Dong et al. 2002).

All cells were imaged in the PMC after the 72-hour resting period and analyzed in the PMC. The selected features and regression model are identical from the primed population. The activity score still represents the relative translocation response in comparison to the primed population. For a drug candidate to be determined to have a significant drug response, the NFAT translocation response should resemble a healthy (positive control) population of T cells. Successful drug candidates should either recover immuno-compromised cells from anergy, or prevent anergy from developing in the first place.

5.6.4 Results from IL-2 and anti-CD28

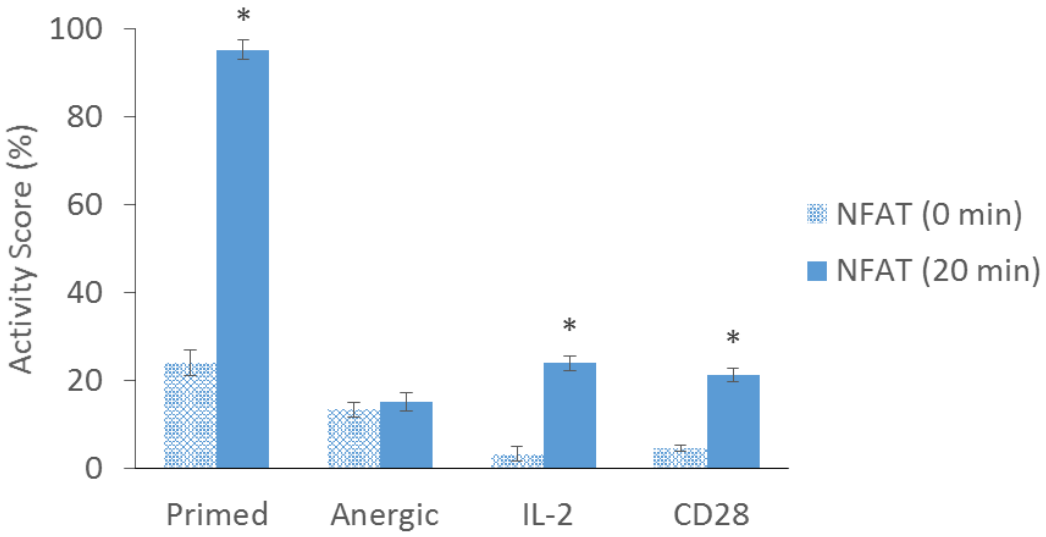

Figure 5-15. NFAT translocation activity scores from IL-2 and anti-CD28 drug responses.

NFAT translocation response from the control drug candidates IL-2 and anti-CD28, relative to the original primed and anergic populations (N = 25). Significant changes between 0 min and 20 min phenotypes are observed in both IL-2 and anti-CD28 drug responses. Activity scores are normalized to percent activation. The first two columns (Primed/Anergic) serve as positive/negative controls to analyze the strength of NFAT translocation respectively. *, $p < 0.01$. Error bars indicate standard error.

Ligands to CD28 act as direct competitors to the PD-1 receptor and can override inhibitory effects from PD-1 ligation. This response is concentration dependent. Large concentrations of IL-2 can also bypass the PD-1 pathway and suppress inhibitory signaling cascades even after successful PD-1 ligation. PD-1 binding can suppress IL-2 production resulting in T cell anergy, and vice versa, increasing IL-2 can prevent induction of anergy (Chikuma et al. 2009).

Looking at Figure 5-15, it can be seen that the NFAT activity score responses from these two drug candidates (IL-2 and anti-CD28) were significantly higher than

the anergic translocation response. However, the NFAT translocation was not as strongly separating as the primed population. This could be a side effect of anergic recovery. Full recovery of the NFAT signaling pathway may require a longer time frame. Although cells rapidly recover from anergy due to IL-2 after a couple days or less, it is typically measured through cell cycle counting or cytokine analysis. Direct effect on the kinetics and strength of transcription factor localization is unknown during anergic recovery. Ligation of the PD-1 receptor leads to an immediate down regulation in TCR expression that recovers slowly over the course of 3 days (Karwacz et al. 2011). Although we rest the cells for 3 days after induction, the NFAT and TCR signaling pathways may still be compromised. Further studies are needed to fully understand the effects on NFAT translocation dynamics during PD-1 drug responses.

We did observe that cells introduced to anti-CD28 and IL-2 were proliferating normally, despite the lower NFAT translocation activity score. Anergic cells are 'sickly' and have lower cell counts than primed cells. It was confirmed that cells with IL-2 and anti-CD28 had higher cell counts and media absorption (Phenol Red shifts to the yellow spectrum after cells secrete waste products). The data suggests that the addition of anti-CD28 and IL-2 were partially successful in recovering from PD-L1 induced anergy.

5.6.5 Results from anti-PD-1

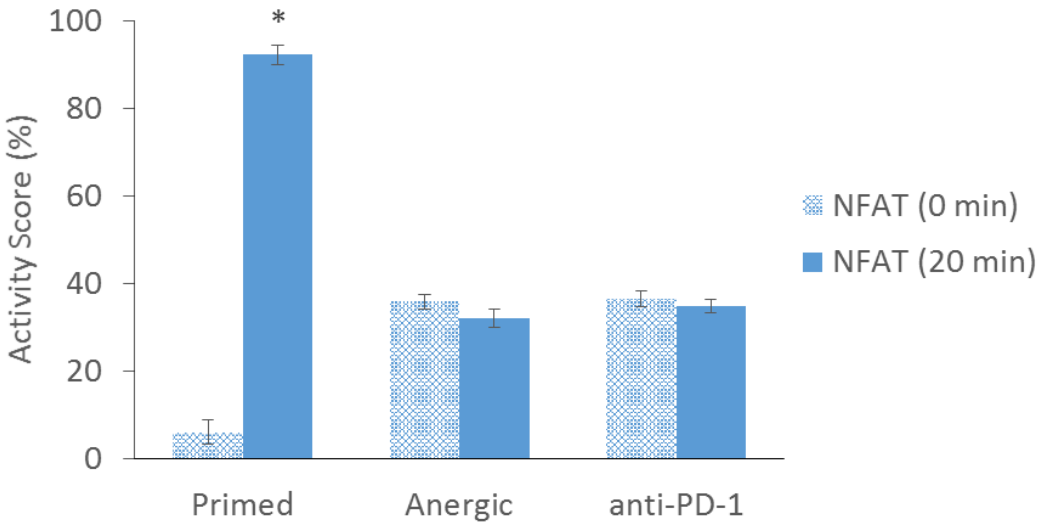

Figure 5-16. NFAT translocation scores from anti-PD-1 drug response.

NFAT translocation response from testing the immune checkpoint blockade antibody drug anti-PD-1 (N = 24). No significant shifts in NFAT translocation phenotype was detected after introducing PD-1 blockade. Activity scores from the anti-PD-1 population resemble the 0 min and 20 min phenotypes from the negative population (Anergic), indicating a lack of drug response activity. *, $p < 0.01$. Error bars indicate standard error.

In theory, the introduction of an antagonistic anti-PD-1 drug (clone J116) should block inhibitory effects from PD-1 ligation. Many research groups have applied various drug candidates to suppress or block the PD-1:PD-L1 interaction and have successfully recovered/prevented cells from anergy (Wong et al. 2007; Okazaki & Honjo 2007; Podojil & Miller 2009). *In vitro* methods used to induce PD-1 related anergy traditionally involve transfecting the PD-L1 ligand into dendritic cells or cell lines. This method is a physiological method of presenting an antigen, such as PD-L1, to T cells, but was not practical in our laboratory. We decided on using immobilized

PD-L1-Fc on petri dishes which has not been attempted previously. There has been one study that used a peptide pool and anti-PD-1 blocking antibodies *in vitro* in petri dishes that was very similar to our approach (Grenga et al. 2016). Further discussion with researchers from Arlene Sharpe's group was encouraging using immobilized PD-L1-Fc but were primarily based on bead immobilization. Due to the difficultly of immobilizing proteins on beads, plastic petri dishes were decided as a compromise.

Looking at Figure 5-16, the data suggests that the introduction of anti-PD-1 did not prevent anergy and did not recover cells back to a healthy proliferation state. NFAT translocation from anti-PD-1 treated cells was undetectable, similar to the drug response from the anergic population. Although our specific PD-1 antibody does not directly bind to the active site on the PD-1 receptor to block ligation, the antibody works by preventing downstream signaling from PD-1 after binding.

We attempted many different methods to replicate the results from clinical trials and literature. We varied incubation periods from 24 hours to 48 hours with the drug candidate, multiplexed with a PD-L1 blocking antibody, titrated multiple concentrations up to 20 μg/mL, tested both soluble and immobilized antibody induction, changed the length of the resting period after drug incubation, and tried an alternate drug induction method. The alternate induction method involved priming the cells with immobilized anti-CD3 first for 24 hours. Then, the cells were transferred to a suspension tube with soluble anti-PD-1. After 30 min, the cells were transferred back to a petri dish with PD-L1-Fc for 12 hours. After probing with PD-

L1-Fc, the cells are finally moved to a culture flask and rested. None of these modifications resulted in a significant or consistent NFAT translocation response. We did observe successful NFAT translocation in some experiments, but those results were deemed to be false positives due to human error or variance from low cell counts.

We have been unable to find any previous reports in which immobilized PD-L1-Fc was used as a means to recover cells from anergy i*n vitro*. It is possible that the anergic state induced in this fashion is permanent, or requires a different sequence, or other factors available *in vivo* for recovery. Steric effects from the petri dish/cell interface may prevent the anti-PD-1 drug from blocking the PD-1 pathway. Another possible source of error is our choice of translocation readout. Most research groups measure anergic recovery using cytokine (IL-2, IFNγ) analysis or surface proliferation markers (CD25/CD69). It is possible that proliferation status was successfully recovered in our experiment from anti-PD-1 blockade, as would be measured by cytokines, but the NFAT translocation state was not restored. Since there is no literature on NFAT translocation strength during anergic recovery, more studies are needed to confirm that our negative result is a true biological result, and not due to failures in experimental design.

5.7 Direct adaptations from HCA

5.7.1 Motivation

It is important to compare our new 1-D imaging cytometry to the existing classical and established methods for drug screening and testing. There are existing standardized and well-established methods for drug screening. We adapted multiple quantitative cross checks to established methods.

5.7.2 Dose response

To test the ability of the PMC to measure dose response curves, NFAT translocation was measured using standard anti-CD3 TCR activation. Two-step TCR crosslinking was used, varying concentrations (0 – 10 μg/mL) of anti-CD3 OKT3 (eBioscience #16-0037) and anti-CD28 (eBioscience #16-0289, CD28.2) were added and incubated with the chilled cells for 30 min on ice. CD28 antibody concentration was half the concentration of the corresponding anti-CD3 concentration. Negative controls used unlabeled mouse IgG isotype control in place of primary antibodies. Goat anti-mouse IgG (20 μg/mL, Invitrogen #A16074) was added and allowed to crosslink for another 30 min on ice. All samples were placed in a 37˚C water bath for 20 min to induce translocation of NFAT and fixed with the same protocols.

Results are presented in Figure 5-17. The NFAT activity score on the y-axis represents the fractional percent translocation of NFAT. The EC50 point for CD3/CD28 activation is indicated with a dashed line at 0.3 μg/mL which is consistent with the literature (Tomkowicz et al. 2015).

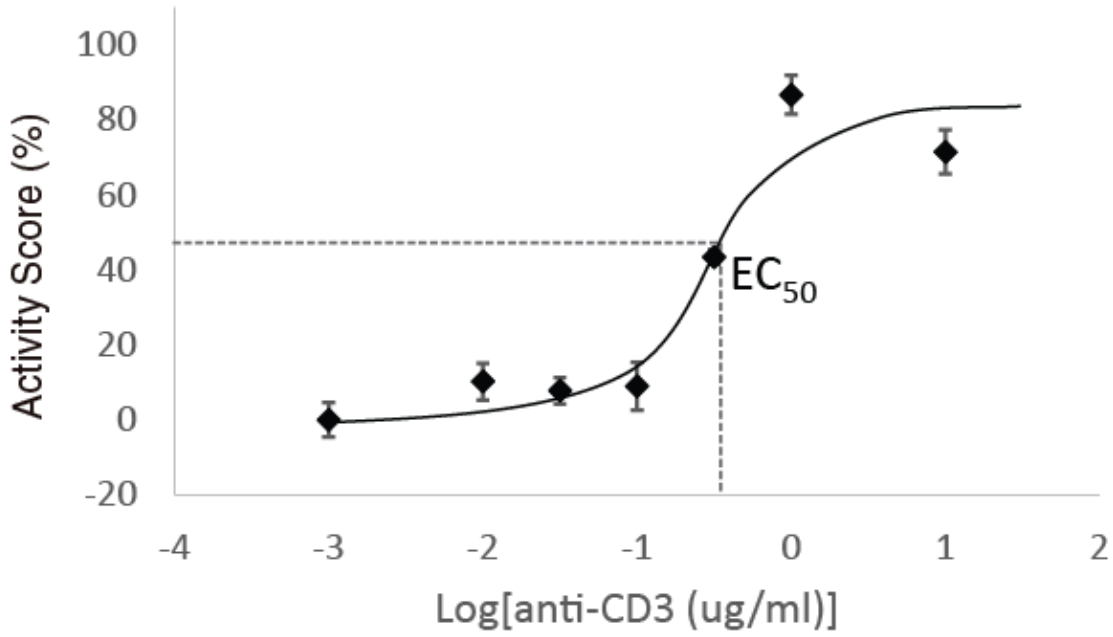

Figure 5-17. EC50 dose response curve for NFAT translocation using anti-CD3/CD28 TCR activation.

NFAT translocation was induced in primary T cells with anti-CD3/CD28 antibodies. Concentration of antibody was varied across 10-fold dilutions. EC50 point was measured to be around 0.3 µg/mL. Each point is the mean of 9 replicates (N=9). Error bars represent standard error (SEM). Y-axis represents relative NFAT translocation to high/low controls.

As a second quantitative test, an IC50 dose response assay was preformed using Cyclosporin A (CsA). Calcineurin is responsible for the de-phosphorylation of the NFAT subsequent nuclear translocation. Since CsA directly binds to calcineurin and inhibits substrate binding, adding increasing concentrations of CsA should lead to lower levels of IL-2 activity (Murphy & Hughes 2002; Leitner et al. 2011). Although the PMC readout uses NFAT translocation as its readout, there should be a strong correlation between NFAT translocation and IL-2 activity.

The IC50 is reported to be in the range of 1 μg/mL to 10 μg/mL in the presence of costimulatory CD28 activation (Leitner et al. 2011; Murphy & Hughes 2002). With ionomycin induction of NFAT, the IC50 of CsA is reported to be in the range of 0.1 μg/mL (Maguire et al. 2013). The immunosuppressive effect of CsA is much less effective with CD28 co-stimulated T cells (Leitner et al. 2011).

Cells were incubated with varying concentrations of CsA (0.005–500 μg/mL with 10-fold dilutions) for 30 min at 37˚C. After incubation with CsA, cells were activated as described previously (CD3/CD28 antibodies) and stained for NFAT translocation. Two-step TCR crosslinking was used, 5 μg/mL of anti-CD3 OKT3 (eBioscience #16-0037) and 2.5 μg/mL anti-CD28 (eBioscience #16-0289, CD28.2) were added and incubated with the chilled cells for 30 min on ice. Negative controls used unlabeled mouse IgG isotype control in place of primary antibodies. Goat anti-mouse IgG (20 μg/mL, Invitrogen #A16074) was added and allowed to crosslink for another 30 min on ice. All samples were placed in a 37˚C water bath for 20 min to induce translocation of NFAT and fixed with the same protocols.

Results are shown in Figure 5-18. The IC50 point was measured to be around 0.1 μg/mL. This concentration is an order of magnitude off compared to results from CD28 co-stimulated cells (Leitner et al. 2011), but is almost identical to the IC50 point obtained using ionomycin induction (Maguire et al. 2013). We suspected the discrepancy was due to differences in readout method and NFAT induction. The strength of NFAT translocation is loosely correlated to the strength of IL-2 upregulation. Each readout method has different mechanisms and dynamics. IL-2

and cell count measurements are bulk measurements, which may not be representative of the individual characteristics of each cell, which our method measures. Another reason for the discrepancy could be that the immunosuppressive effect of CsA is more potent in primary cells, so less CsA is needed. More research needs to be done to correlate the immediate dynamics of NFAT translocation with long term proliferation.

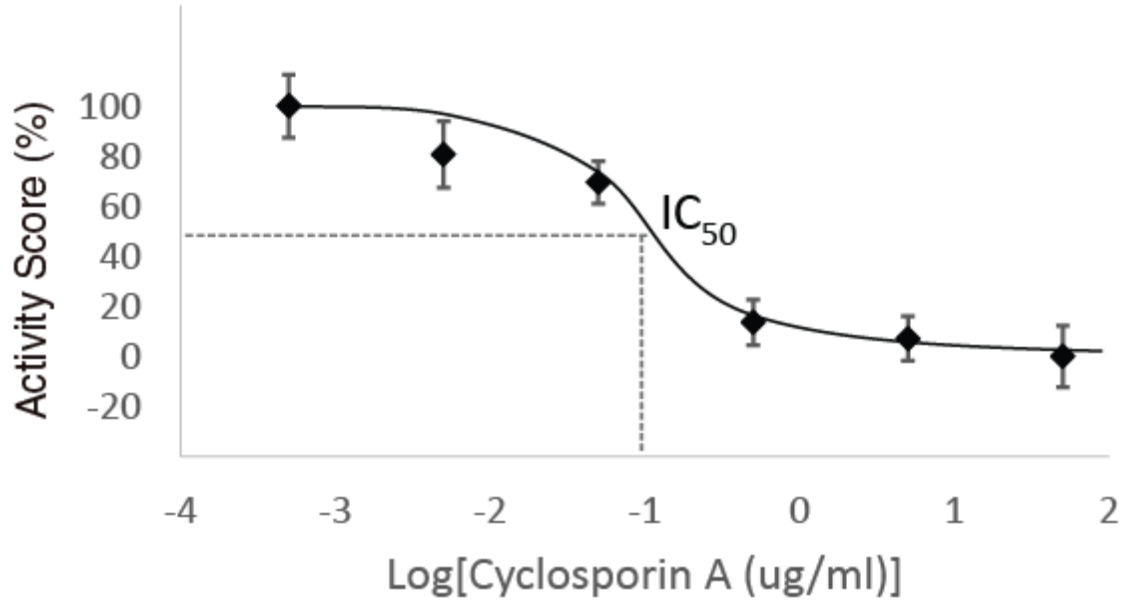

Figure 5-18. Cyclosporin A (CsA) IC50 inhibition dose response curve for NFAT translocation.

NFAT translocation was measured in primary T cells. Cells were induced with identical CD3/CD28 concentrations but were pre-incubated with varying concentrations of CsA at 10-fold dilutions. The IC50 point was measured to be around 0.1 μg/mL. Each point is the mean of 9 replicates (N=9). Error bars represent SEM. Y-axis represents relative NFAT translocation to high/low controls.

5.7.3 Temporal response

One of the initial goals of this work was to test the ability of the PMC to measure transient phenotypes and kinetics within T cells with high temporal resolution. Both NF-kB and NFAT were measured multiple time intervals. Cells were labeled with primary antibodies against CD3 (eBioscience #14-0037, OKT3 clone, 5 μg/mL) and CD28 (eBioscience #16-0289, CD28.2 clone, 2.5 μg/mL), on ice; secondary antibodies are added to crosslink primary antibodies (Invitrogen anti-mouse IgG #A16074, 20 μg/mL). Both NFAT and NF-kB translocation was induced by submerging samples in 37˚C water bath. Cells were removed at 15 min intervals for a total of 60 min as indicated by the graphs. NFAT and NF-kB were stained separately and imaged in the PMC. Temporal response curves were constructed for each transcription factor. As seen in Figure 5-19, the PMC was able to measure temporal dynamics during both NF-kB and NFAT translocation.

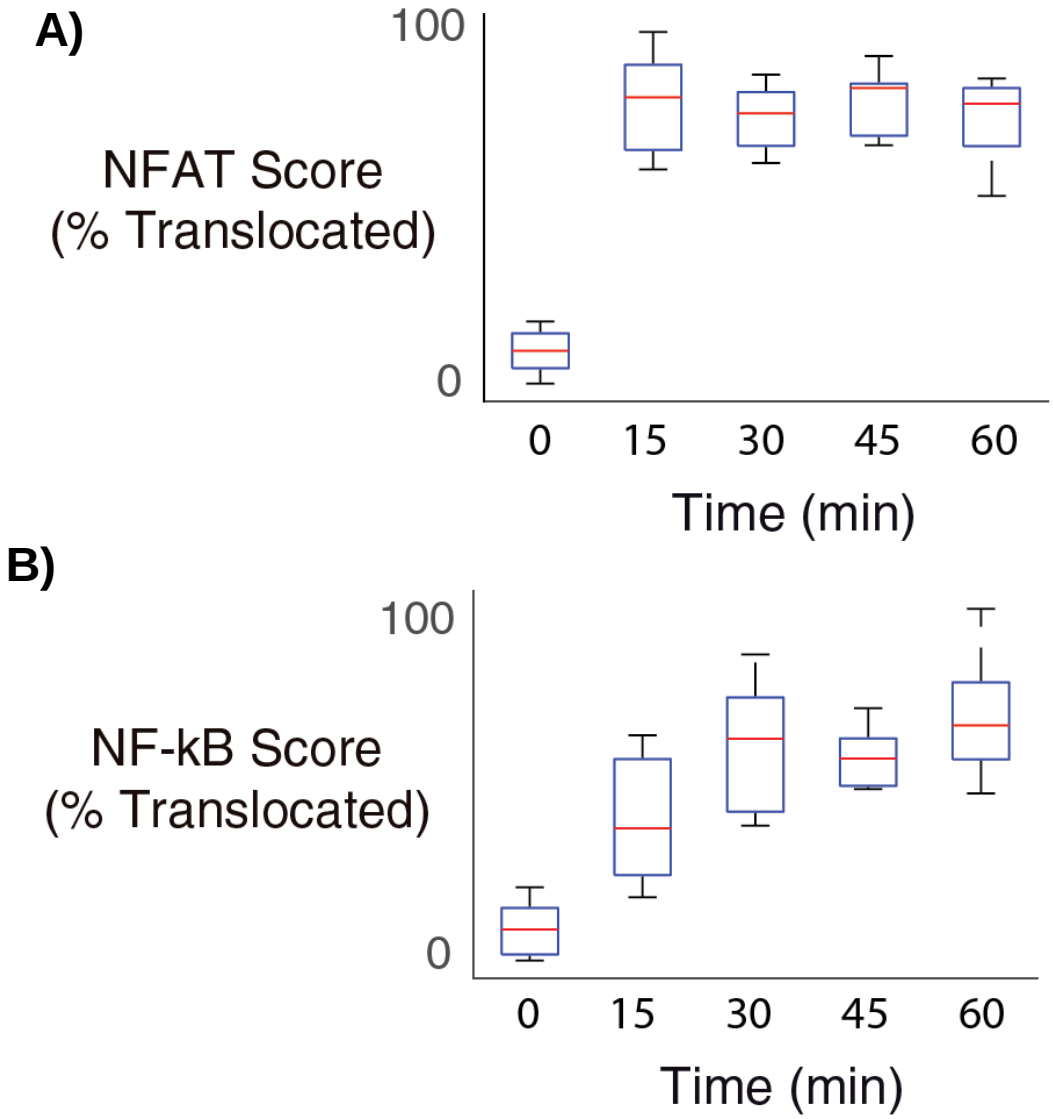

Figure 5-19. NFAT and NF-kB translocation activity scores from 0–60 min.

A) NFAT translocation was induced with PMA/ionomycin (10 µg/mL/10 mM) in a water bath. Samples were taken out and fixed at 15 min intervals to measure the temporal changes in spatial localization over time. Each box plot represents 8 replicates (N=8). B) NF-kB translocation was induced with TNFa (500 ng/mL). Samples were taken out and fixed at 15 min intervals. Each box plot represents 8 replicates (N=8).

As mentioned in section 5.5, NF-kB is a very weakly translocating response and cannot be visually confirmed using 2-D microscopy. Because regression modeling

attempts to maximize the distance between positive and negative phenotypes, even subtle weak phenotypes will be detected by the PMC. We were still able to observe noticeable changes over time in the NF-kB phenotype (Figure 5-19B). The rate of translocation is consistent with kinetic rates in the literature, around maximal translocation around 45 min (Molitor et al. 1990). However, individual variance across replicates for each time point is also much higher for NF-kB. This is a sign that the phenotype is much weaker for NF-kB and the algorithm is not as highly separating.

On the other hand, the temporal curve for NFAT translocation produced much larger separations between temporal phenotypes (Figure 5-19A). However, as evident from the data, NFAT translocation is much more rapid and binary in its translocation response. The rate of translocation is consistent with the literature, maximal NFAT translocation occurs around 20 to 30 min (Torgerson et al. 1998).

To further investigate the rapid translocation response, we looked NFAT translocation with higher temporal resolution. Cells were removed at 1 min intervals instead of 15 min intervals. Intermediate phenotypes were detected and confirmed (Figure 5-20).

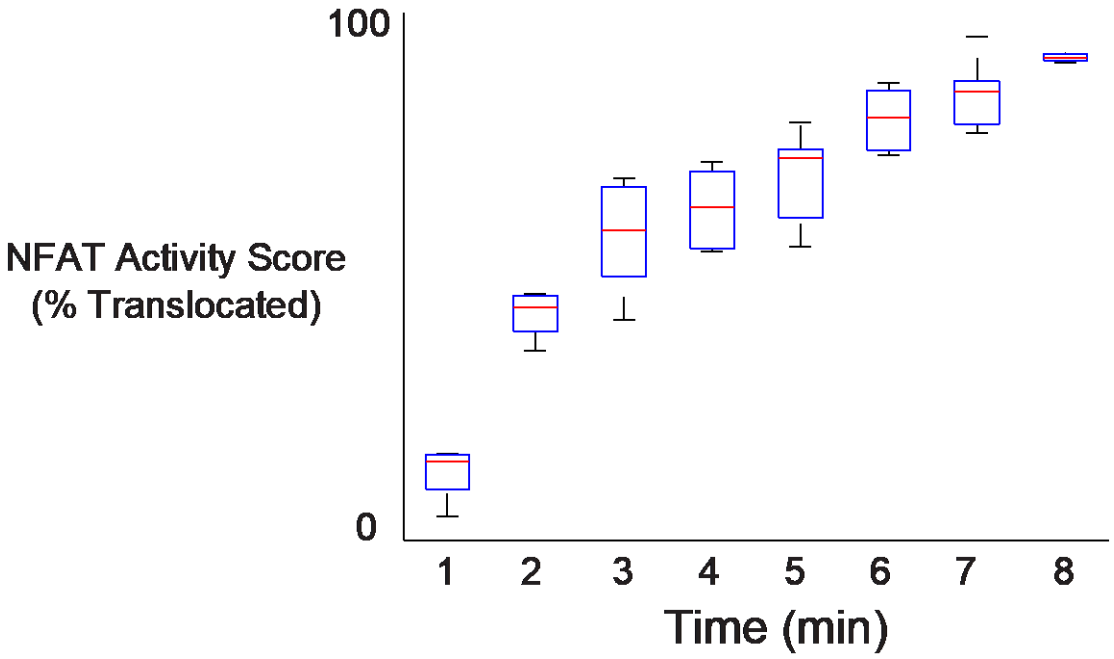

Figure 5-20. Temporal response curves for NFAT translocation from 0–8 min.

NFAT translocation was induced with PMA/ionomycin using the same methods in Figure 5-19. However, samples were taken out and fixed at 1 min intervals for a total of 8 min. Each box plot represents 8 replicates (N=8).

The data presented above show the ability of the PMC to measure intermediate phenotypes. The intermediate phenotypes are consistent with the standard temporal kinetics as described in the literature. Looking at subtle spatial phenotypes as a function of time is similar to studying kinetics of signaling pathways. This kind of data can be very useful in understanding the true mechanisms of drug interactions, and how drugs would affect the kinetic signatures of signaling pathways within T cells.

Unfortunately, it is impractical to measure full kinetic curves for each experiment. Most of our assays use a single time point at 20–40 min to determine

the strength of the translocation response. Although they are of considerable scientific interest, at the moment these kinetic studies are not practical as a new approach for high-content screening. Differences in slope, time constant, magnitude of response, or duration could in the future elucidate new or subtle differences in the strength of a translocation response. This would help understand the mechanism of actions for new drugs, and could become practical with a professional level of optimization of our PMC technology, even with high throughput applications. More research would be needed to understand how these kinetic signatures correspond to mechanisms of drug action.

Chapter 6 - Conclusions

6.1 Summary of Aims

One of the main advantages to using 1-D cytometry as a screening tool is the speed and objectiveness of decision making. Our technology is well-suited for rapid assay development due to its automated and unsupervised statistical workflow. Combined with the data efficiency of 1-D imaging and low sample consumption, high throughput high content cytometric analysis is possible with primary T cells. Although protein localization is not resolved to the accuracy of 2-D microscopy, our activity score model infers relative spatial and temporal cellular phenotypes with nearly the same accuracy and much higher data efficiency. Overall, the goal of this work was to improve and develop 1-D cytometry as a viable method for high throughput screening. In addition, we developed primary T cell assays using the PMC technology to study the drug responses by probing the immune checkpoint pathway.

In aim 1, improvements to the instrumentation and reliability of the PMC signal were conducted. Optical sensitivity and SNR were investigated and optimized through sample digitalization, optical filters, and better mechanical alignment. Lane-to-lane variance was minimized with algorithmic normalization and by using better control samples. Microfluidics and operational protocols were modeled and optimized for continuous high throughput operation. This is key for screening applications that require assay stability and speed in both imaging and analysis.

Data storage and sample volume requirements were both minimized to highlight the efficiency possible with the PMC platform.

In aim 2, we designed a hands-off method of automated statistical analysis of 1-D imaging data. Current 2-D HCS requires highly trained expert operators to develop assays. Often, this requires subjective gating steps and 'intuitive' decisions to determine physiological phenotypes. Our method was focused on unbiased assay development. We designed automated algorithms to isolate the most statistically significant features obtained from our 1-D images. We used the most relevant features to build an 'sample-blind' regression model which outputs a single activity score without any expert input (except for labeling of positive and negative controls). The activity score model allows users to quickly measure drug responses during a high throughput screening assay.

In aim 3, we applied the improved PMC hardware and statistical analysis to developing an immunotherapy assay using primary T cells. NFAT and NF-kB translocation were studied as possible functional readouts for determining the state of internal signaling pathways. NFAT was determined to be the more informative and reliable readout. The first step was to validate the ability of the PMC to differentiate between subtle spatial phenotypes within T cells. After successful implementation of the algorithms, the next step was to use NFAT translocation to measure the functional state of the immune checkpoint pathway. Our main goal was to correlate short-term T cell activation dynamics with long term proliferation to validate our approach. We made significant progress in constructing an assay using

primed and anergic cell populations as positive and negative controls. Drug responses from IL-2, CD28, anti-PD-1, and anti-PD-L1 were studied. By investigating the ability of drug candidates to prevent or recover cells from anergy, we hoped to prove the PMC platform for immunotherapy drug screening. IL-2 and CD28 did partially recover cells from anergy and served as a control for the immune checkpoint blockade antibody drugs. Unfortunately, we could not achieve a consistent recovery from anergy using anti-PD-1. Further work is needed to optimize experimental methods and validate with cytokine analysis.

6.1.1 Future directions

If resources permit, we would want to conduct an immunotherapy drug screen against a real and useful library of candidate compounds. Testing known drug candidates that have predictable drug responses is much different from a blind screening assay, where drug responses are unknown. It is possible that alternate phenotypes may occur from small molecule interactions, and it would be a good exercise to validate our 'sample-blind' approach. Ideally, we would use a library of mAbs or peptides that are presumed to interact with the PD-1 receptor as an agonist or antagonist.

While the current throughput of our technology is sufficient for small screening assays, we project that our system can be expanded even further. Drug discovery applications may require hundreds of thousands or millions of

compounds. In previous publications, we were able to show our digitalization rates and signal-to-noise ratios are consistent with a throughput of ten 384-well plates per hour (McKenna et al. 2011). A more current ADC (analog-to-digital converter, Vertilon IQSP518) with a maximum 390 kHz digitalization rate will increase our current sampling rate by 8-fold. Combined with improved twin-device switching, as used in a previous DNA sequencing system (Aborn et al. 2005), we can eliminate nearly 100% of the refresh time of sample loading and microfluidic recycling. With the updated 96-lane chip design, the system should be able to image across all parallel channels every 25 seconds resulting in a throughput of ten 384-well plates every 17 minutes. Our statistical workflow can be applied at this speed for "on-the-fly" continuous operation with minimal data buffering. This would allow screening of more than 350,000 compounds per day on a single instrument. This is an order of magnitude improvement over the current throughput of present commercial 2-D HCS instruments.

The assay we presented in this work uses a dual color 1-D image to detect localization of a single biomarker (NFAT). However, during the cellular processes of the immune checkpoint pathway, many parallel and downstream signaling events also occur. We would like to multiplex our readout with multiple readouts of different signaling markers. Signaling proteins such as ERK, STAT, AP-1, and AKT have separate localization dynamics which are downstream of T cell activation and the immune checkpoint pathway.

We envisioned the PMC for use with clinical applications as well. For

personalized medicine, it would be credible to conduct a pilot test using actual patient samples with immuno-compromised T cells. Predictably, there is an incentive to study the drug response of patient samples to immunotherapy drugs. As mentioned in the background chapter, some immunotherapies are only effective in certain patients with specific mutations. Peripheral T cells have also been shown to reflect the tumor state from a patient. The immunotherapy assay we designed could easily be modified to act as an alternative preliminary screen to predict patient drug response. A method to directly test *ex vivo* functional drug responses could be useful in clinical applications. Since primary cell samples from patients would be limited, the PMC's volume efficiency allows assays to be performed even in clinical settings.

6.1.2 Conclusions

Our technology occupies a middle ground between classical flow cytometry and 2-D imaging. The results presented place the PMC platform as an unbiased objective approach to drug screening. The unbiased approach is extremely important to eliminate subjective manual gating approaches of current cytometric methods. Having an automated statistical analysis reduces the need for trained expert operators that rely on intuition and experience. These methods are prone to errors in human judgement and confirmation bias. Our automated unsupervised approach also vastly reduces the time needed for assay development.

High throughput operation is optimized and scalable with our technology. This is especially important in drug discovery applications that screen for thousands

or millions of drug candidates. Using human primary T cells in large-scale screening assays has been previously impossible due to the limited volume requirements of primary cell samples. Adoption of physiological relevant assays in drug discovery will only improve the reliability and accuracy. Our low volume and efficient handling of primary cell samples allows for thousands of experimental conditions from a single donor. In addition, our efficient and rapid analysis of human primary T cells has great potential for personalized medicine and clinical studies.

We should add that anergy has also been extremely difficult to study to this point due to its inert nature. Although impractical for high-throughput, the ability to probe drug interactions on anergic cells will help study the biological mechanisms of immune checkpoint blockade drugs and also lead to advancements in better screening assays. This is important as there is a huge trend in developing antibody drugs that target the immune checkpoint pathway, many of which are poorly characterized and understood. There also exists the potential for personalized medicine in probing anergic cells taken from patients. Many patients are tested for genetic markers that determine eligibility for a drug study. Testing the efficacy of drugs on patient blood samples could be a useful non-invasive method to measure drug response.

The significant points presented here highlight the advantages of 1-D imaging. We demonstrate that 1-D imaging provides many new ways to characterize and study primary T cells, and encourages future research directions in both high-throughput drug screening and anergic T cell analysis.

APPENDIX

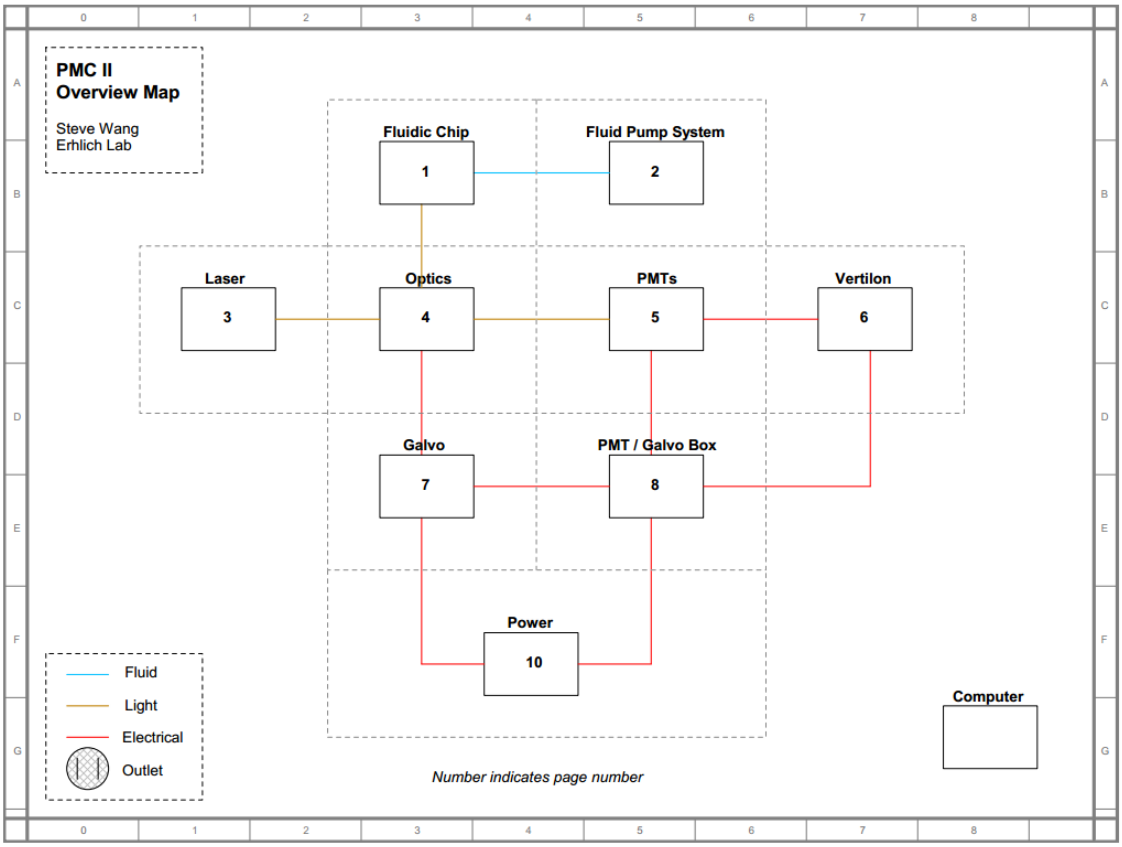

Figure 1. Full layout and wiring/connecting diagram for integrated PMC prototype with automated fluidics and robotic pipettors. Following pages contain individual layouts for each numbered subsection. Custom written programs controlled the drivers and microchip Input/Output. Additional controller software used custom protocols to run assays with minimal operator interaction.

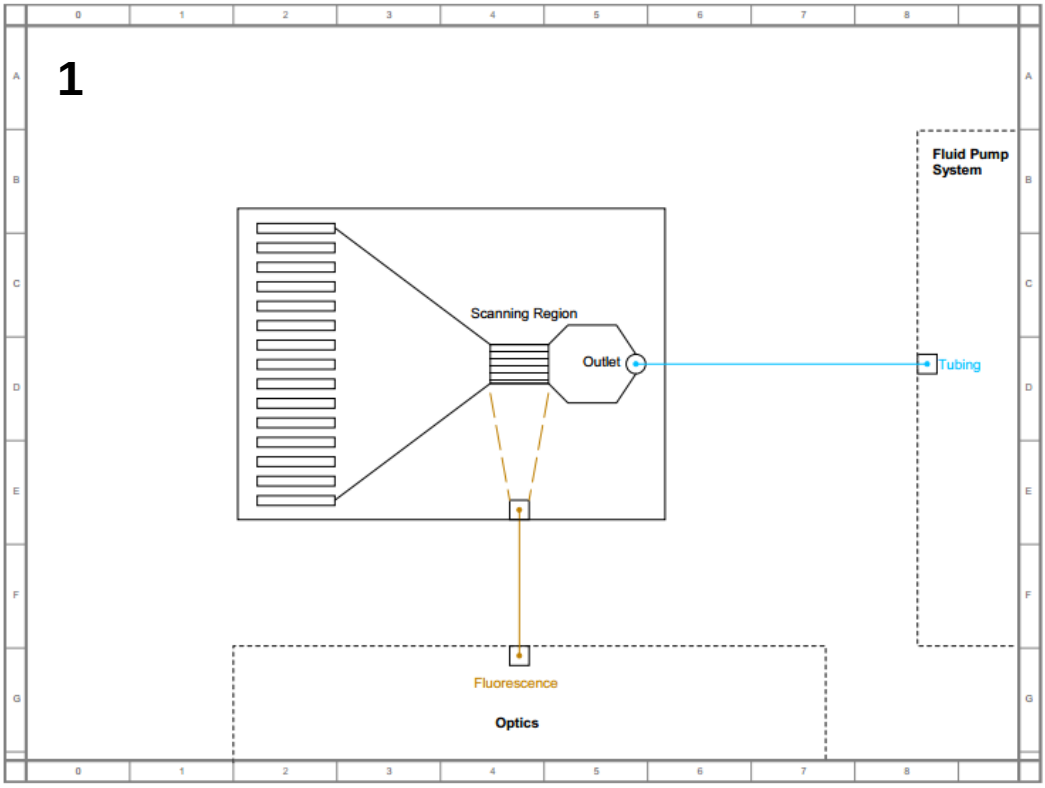
1
Fluid Pump System
Scanning Region
Outlet
Tubing
Fluorescence
Optics

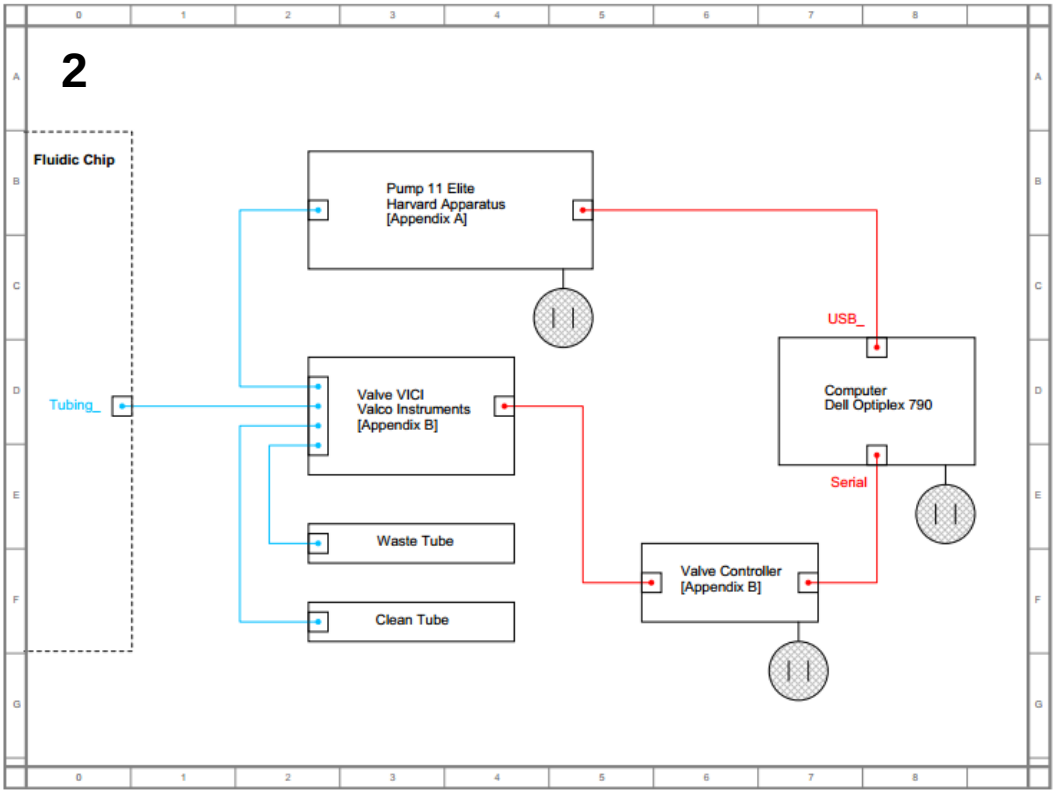
2
Fluidic Chip
Pump 11 Elite
Harvard Apparatus
[Appendix A]
USB_
Tubing_
Valve VICI
Valco Instruments
[Appendix B]
Computer
Dell Optiplex 790
Serial
Waste Tube
Valve Controller
[Appendix B]
Clean Tube

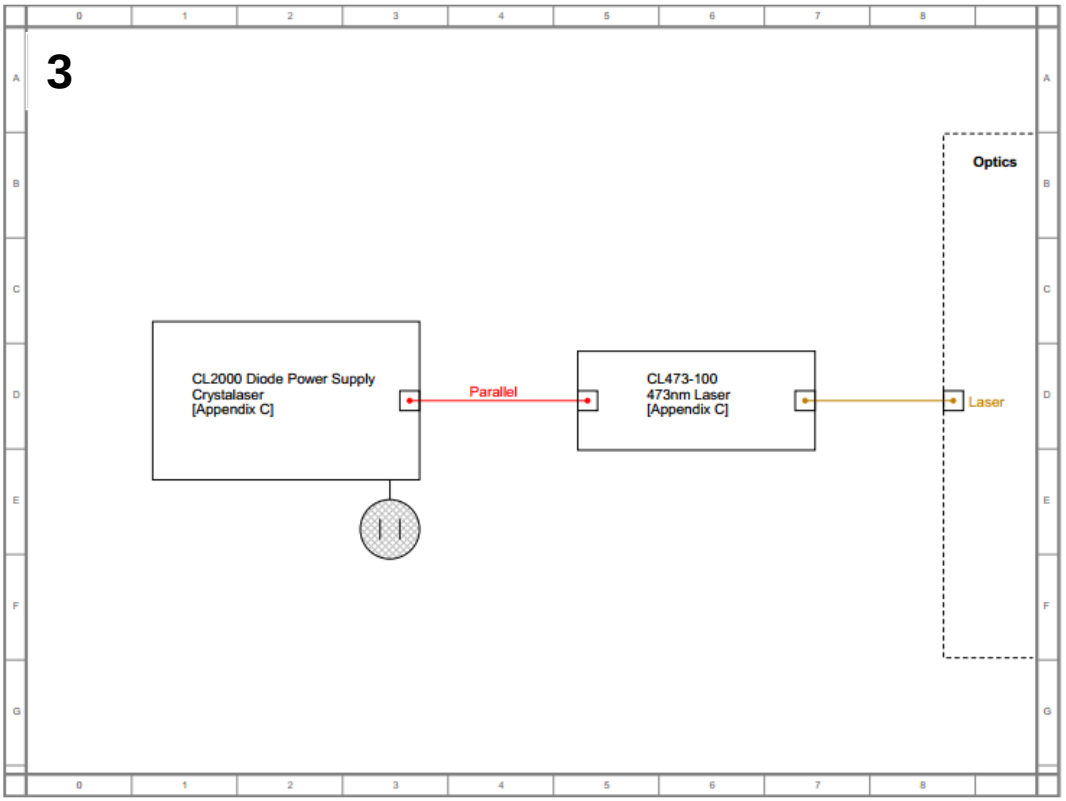
3
Optics
CL2000 Diode Power Supply
Crystalaser
[Appendix C]
Parallel
CL473-100
473nm Laser
[Appendix C]
Laser

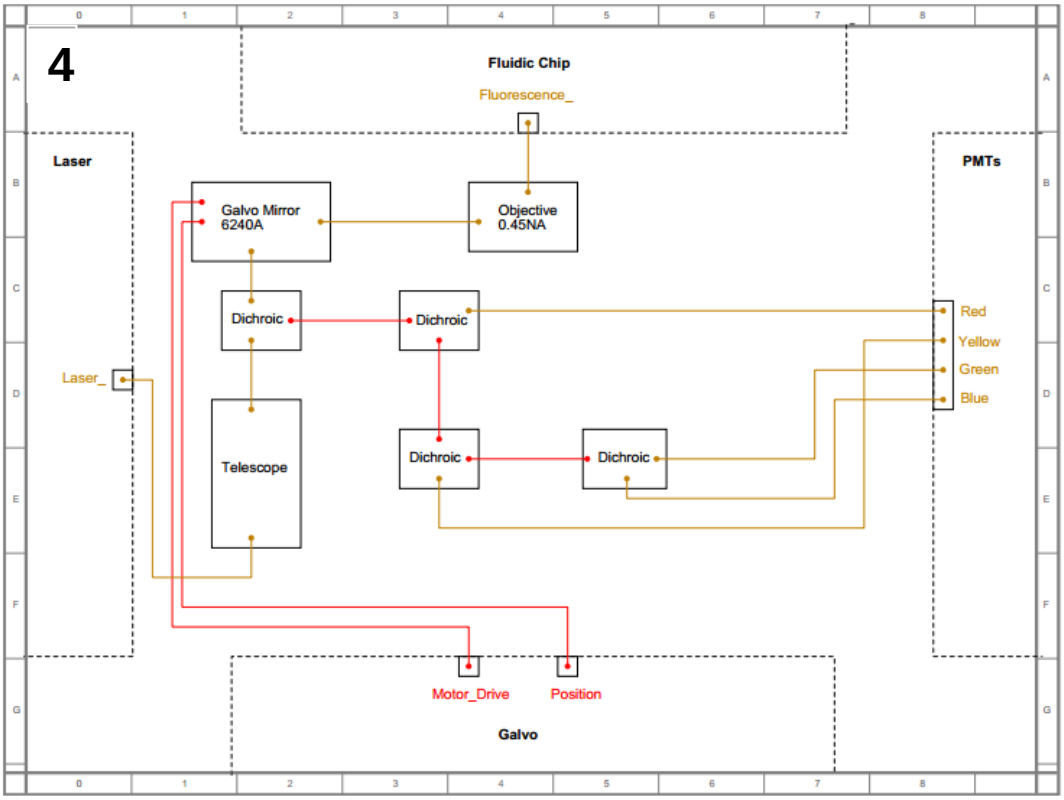
4
Fluidic Chip
Fluorescence_
Laser
PMTs
Galvo Mirror
6240A
Objective
0.45NA
Dichroic
Dichroic
Laser_
Telescope
Dichroic
Dichroic
Red
Yellow
Green
Blue
Motor_Drive
Position
Galvo

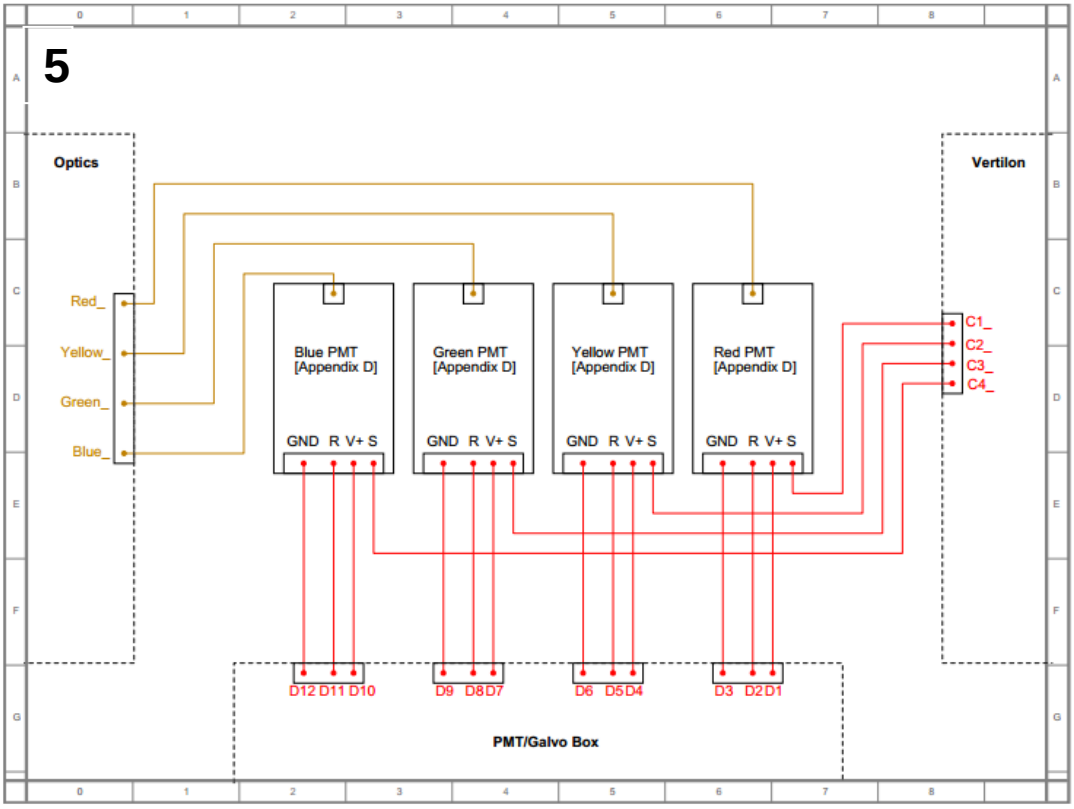
5
Optics
Vertilon
Red_
Yellow_
Green_
Blue_
Blue PMT
[Appendix D]
Green PMT
[Appendix D]
Yellow PMT
[Appendix D]
Red PMT
[Appendix D]
GND R V+ S
C1_
C2_
C3_
C4_
D12 D11 D10
D9 D8 D7
D6 D5 D4
D3 D2 D1
PMT/Galvo Box

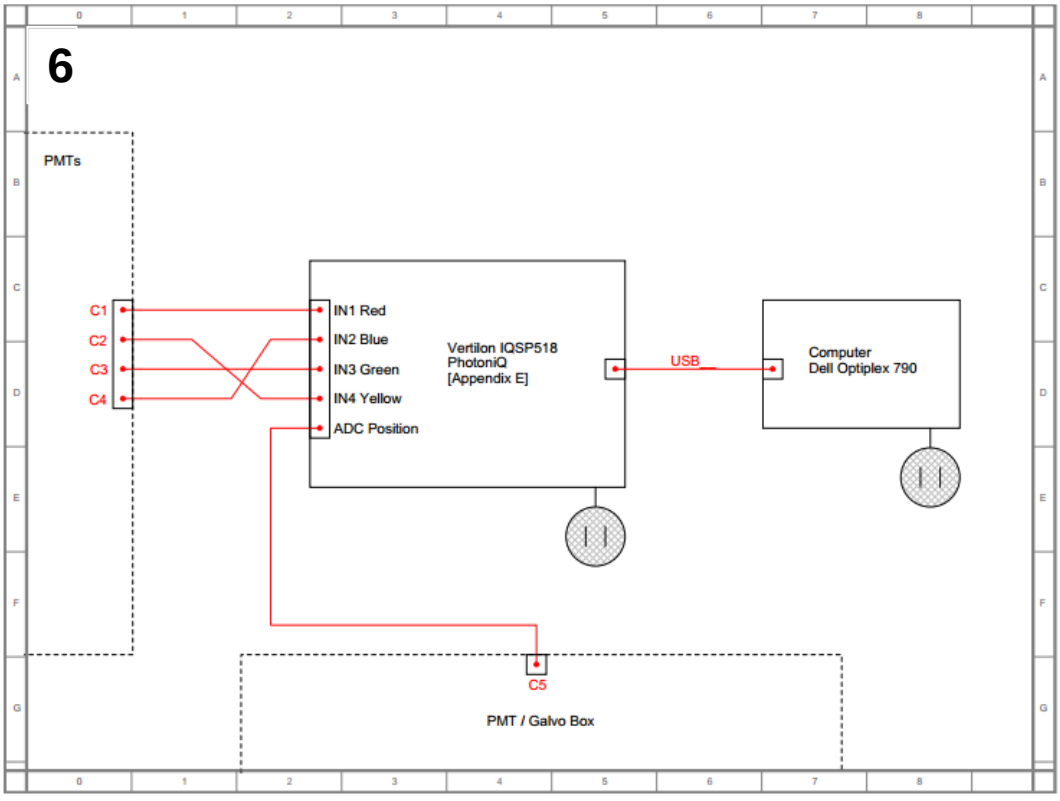
6
PMTs
C1
C2
C3
C4
IN1 Red
IN2 Blue
IN3 Green
IN4 Yellow
ADC Position
Vertilon IQSP518
PhotoniQ
[Appendix E]
USB
Computer
Dell Optiplex 790
C5
PMT / Galvo Box

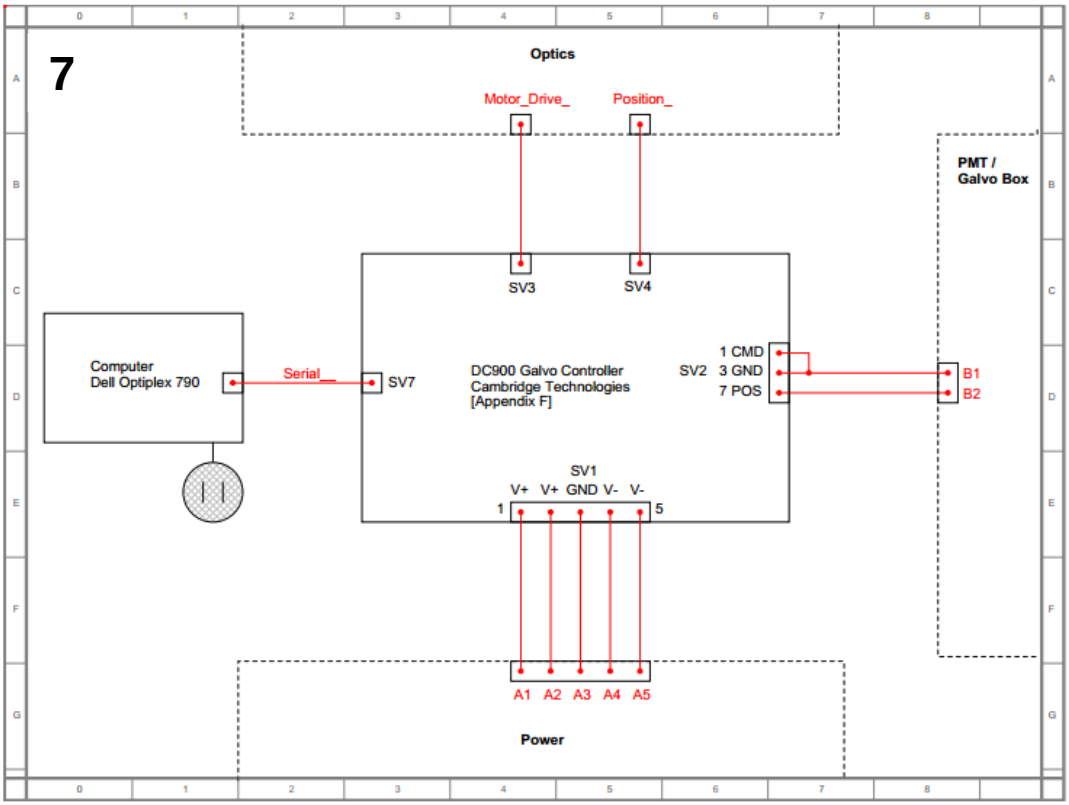
7
Optics
Motor_Drive_
Position_
PMT /
Galvo Box
SV3
SV4
Computer
Dell Optiplex 790
Serial_
SV7
DC900 Galvo Controller
Cambridge Technologies
[Appendix F]
1 CMD
SV2 3 GND
7 POS
B1
B2
SV1
V+ V+ GND V- V-
1
5
A1 A2 A3 A4 A5
Power

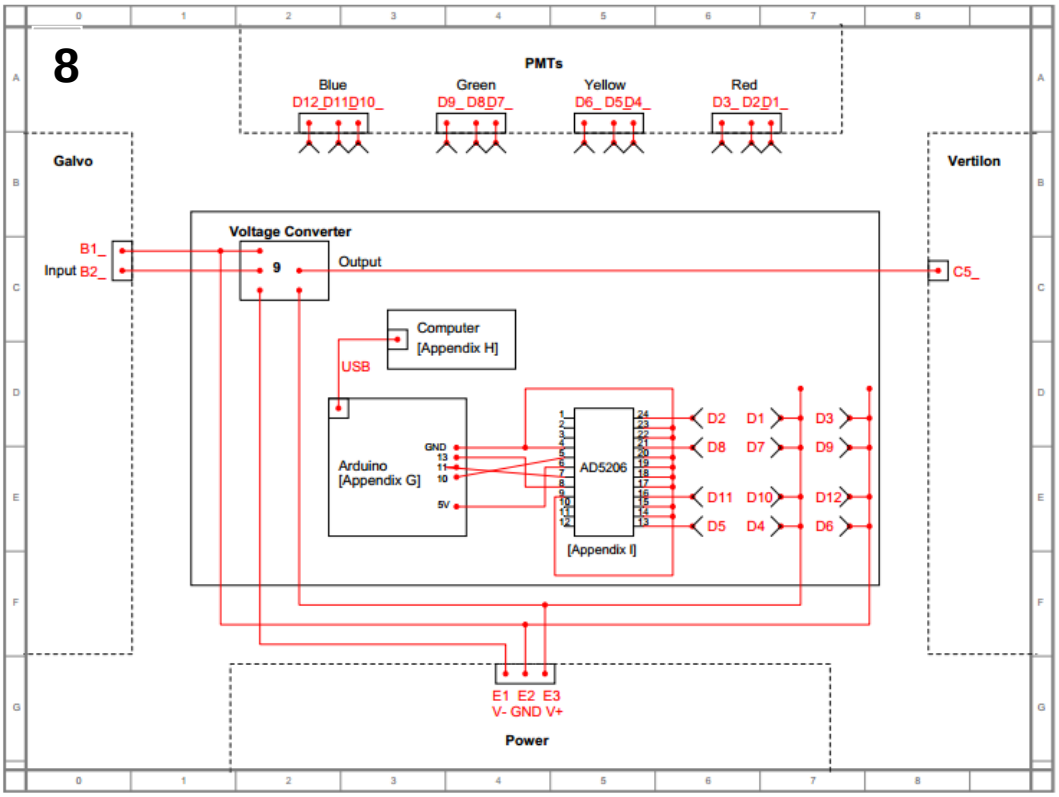
8
PMTs
Blue
D12 D11 D10_
Green
D9_ D8 D7_
Yellow
D6_ D5 D4_
Red
D3_ D2 D1_
Galvo
Vertilon
Voltage Converter
B1_
Input B2_
9
Output
C5_
Computer
[Appendix H]
USB
Arduino
[Appendix G]
GND
13
11
10
5V
AD5206
[Appendix I]
D2
D1
D3
D8
D7
D9
D11
D10
D12
D5
D4
D6
E1 E2 E3
V- GND V+
Power

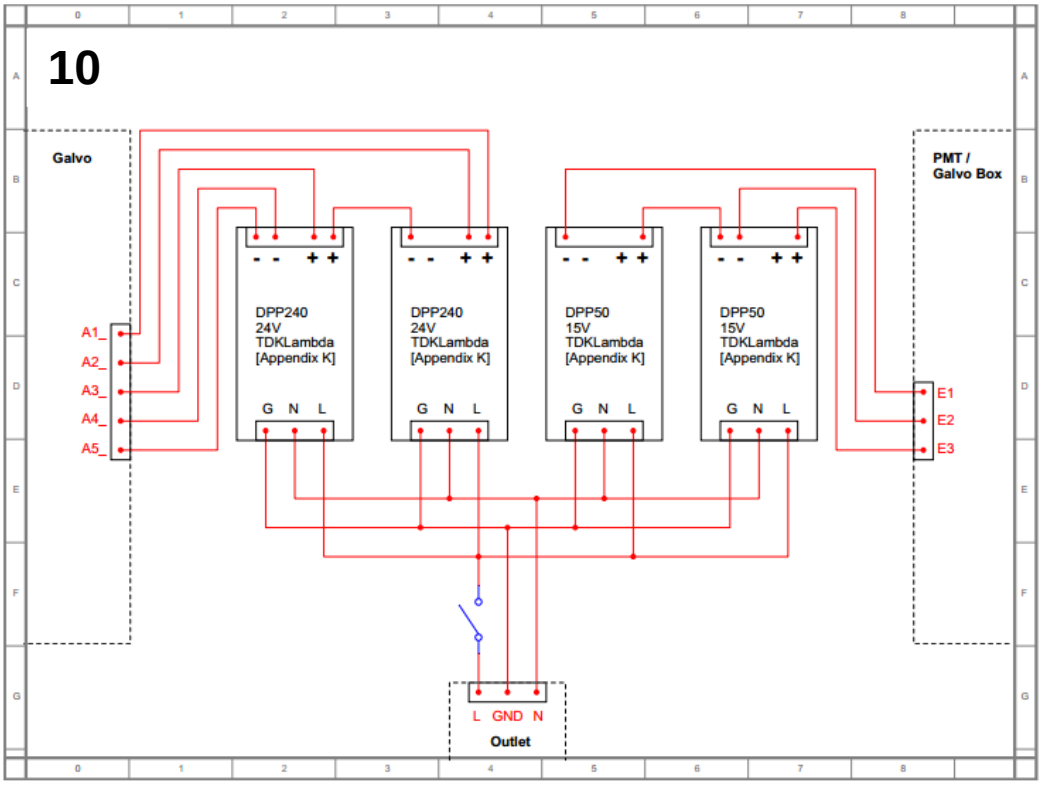
10
Galvo
PMT /
Galvo Box
A1_
A2_
A3_
A4_
A5_
DPP240
24V
TDKLambda
[Appendix K]
DPP240
24V
TDKLambda
[Appendix K]
DPP50
15V
TDKLambda
[Appendix K]
DPP50
15V
TDKLambda
[Appendix K]
G N L
G N L
G N L
G N L
E1
E2
E3
L GND N
Outlet

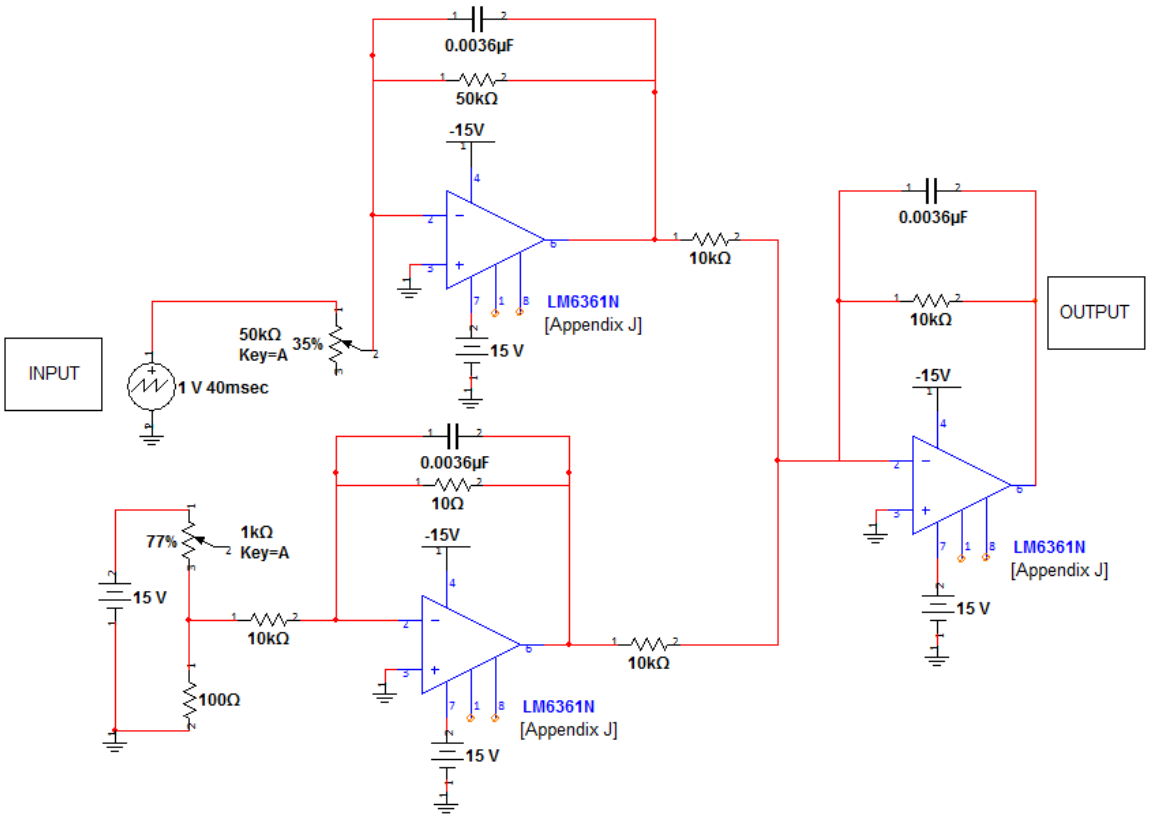

Figure 2. Custom conditioning circuit. Low pass op-amps filters are used to amplify and modulate a triangle wave. Integrator adds a DC voltage to the wave. Resistance and capacitors are chosen to filter out 60 Hz noise.

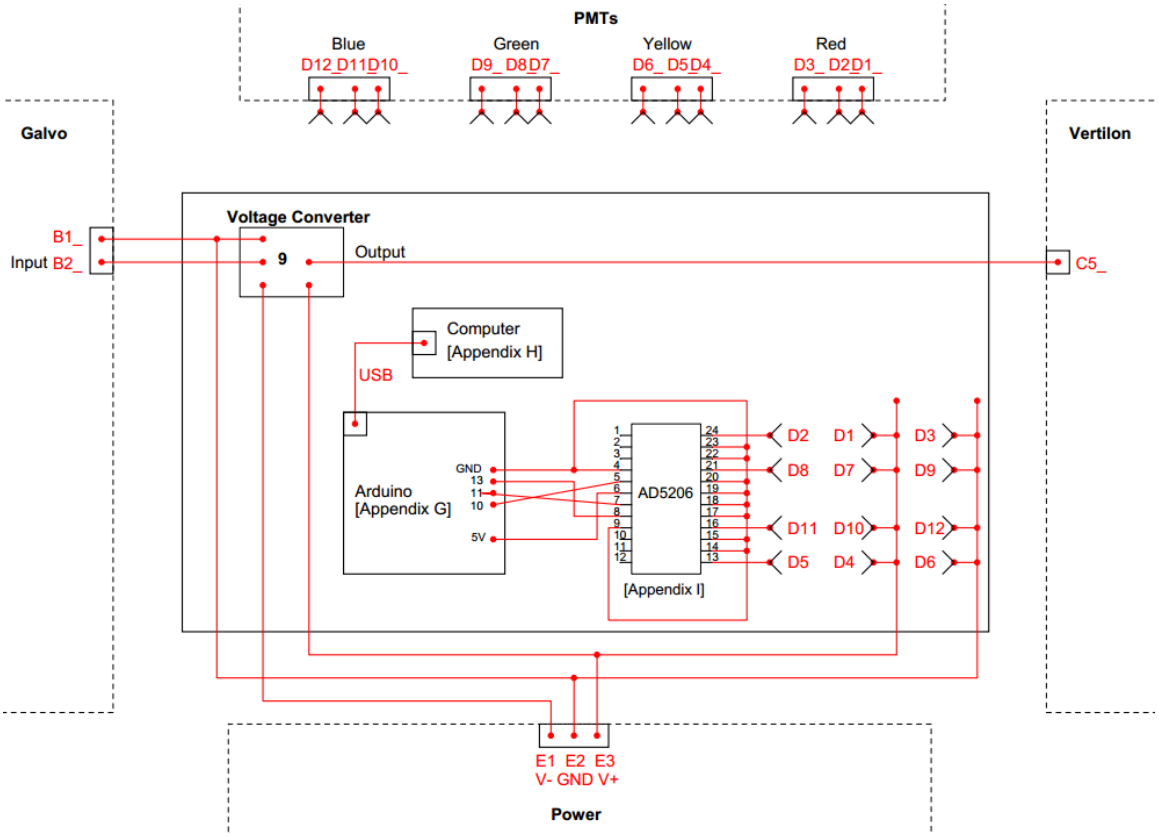

Figure 3. Arduino circuit to control PMT gains through a serial port. AD5206 is a 6 channel potentiometer to control resistance on PMT. Red lines indicates wiring connections between inputs/outputs.

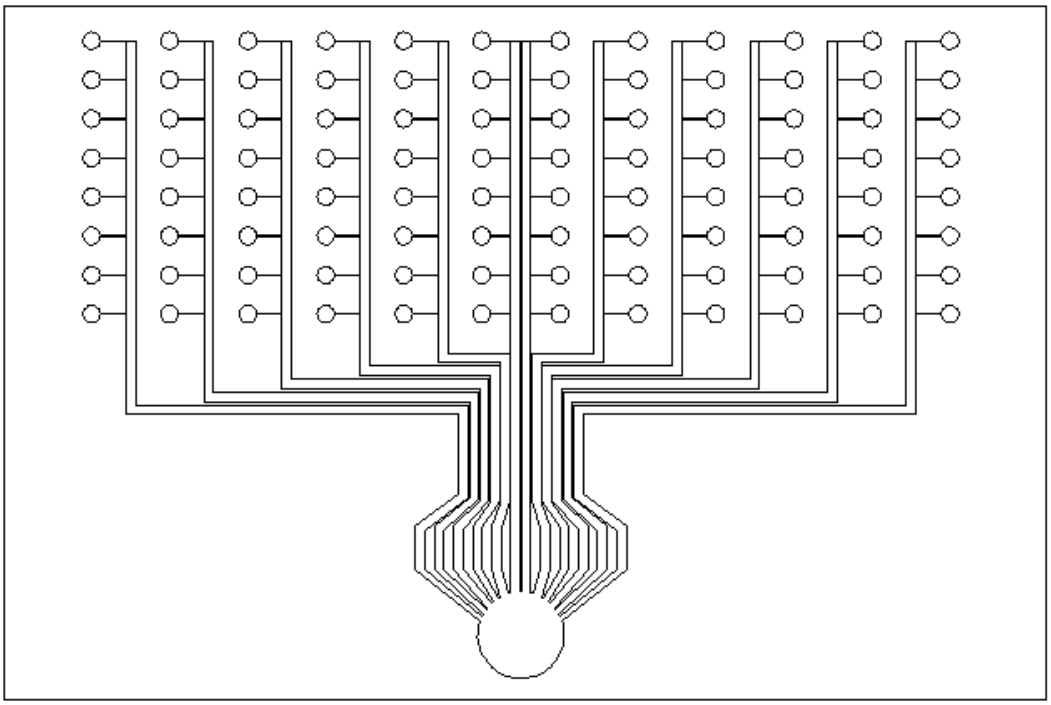

Figure 4. AutoCAD design for a 96-well microfluidic chip. 96 parallel wells would allow for even higher throughput. Input wells align with a standard 96-well plate.

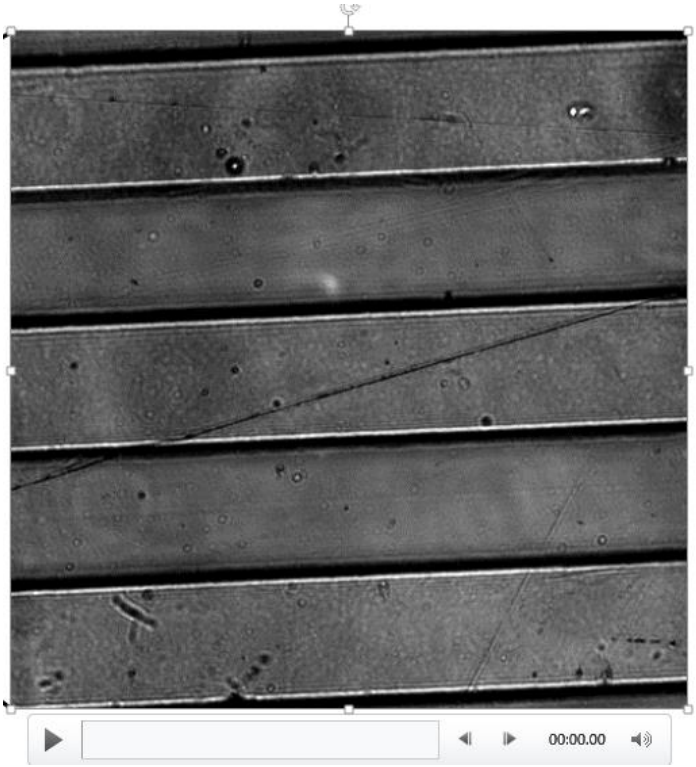

Figure 5. Video still frame of beads flowing through chip. Velocity is calculated by tracking beads frame by frame. Individual bead data is shown in Figure 6.

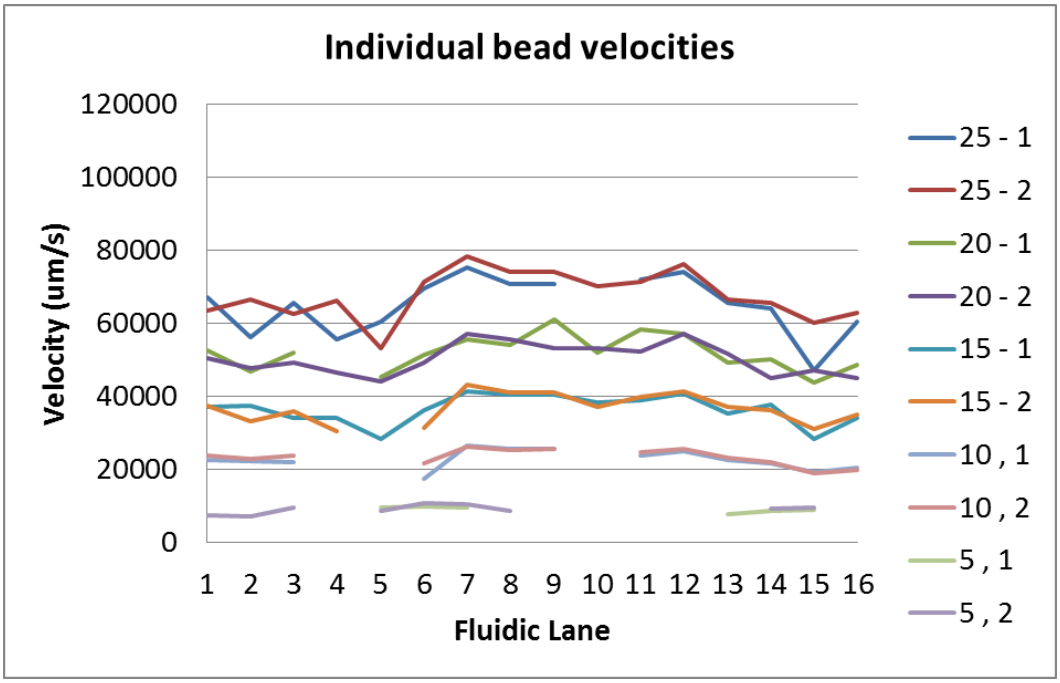

Figure 6. Individual bead tracking velocities.

xpos	Position for well location (x-axis)
linenum	Tracking time (y axis)
r_noise_std_pmt1	Noise
r_maxpeak_pmt1	Peak Intensity
r_snr_pmt1	
r_smoothed_std_pmt1	Smoothness
r_left_fwhm_pmt1	Width
r_right_fwhm_pmt1	
r_lr_fwhm_pmt1	
r_ref_left_fwhm_pmt1	
r_ref_right_fwhm_pmt1	
r_ref_lr_fwhm_pmt1	
r_fwhm_pmt1	
r_fw75m_pmt1	
r_fw25m_pmt1	
r_fw25m_fw75m_pmt1	
r_left_top_slope_pmt1	Slope
r_left_mid_slope_pmt1	
r_left_bot_slope_pmt1	
r_left_avg_slope_pmt1	
r_right_top_slope_pmt1	
r_right_mid_slope_pmt1	
r_right_bot_slope_pmt1	
r_right_avg_slope_pmt1	
r_lr_slope_pmt1	
r_left_area_pmt1	Area
r_right_area_pmt1	
r_lr_area_pmt1	
r_ref_left_area_pmt1	
r_ref_right_area_pmt1	
r_ref_lr_area_pmt1	
r_top_area_pmt1	
r_bot_area_pmt1	
r_bt_area_pmt1	
r_total_area_pmt1	
r_left_peri_pmt1	Perimeter
r_right_peri_pmt1	
r_lr_peri_pmt1	
r_ref_left_peri_pmt1	

r_ref_right_peri_pmt1	
r_ref_lr_peri_pmt1	
r_total_peri_pmt1	
r_roundness_pmt1	Perimeter/Area
s_num_peak_pmt1	Repeat for Smoothed Curve
s_center_pmt1	
s_left_fwhm_pmt1	
s_right_fwhm_pmt1	
s_lr_fwhm_pmt1	
s_ref_left_fwhm_pmt1	
s_ref_right_fwhm_pmt1	
s_ref_lr_fwhm_pmt1	
s_fwhm_pmt1	
s_fw75m_pmt1	
s_fw25m_pmt1	
s_fw25m_fw75m_pmt1	
s_left_top_slope_pmt1	
s_left_mid_slope_pmt1	
s_left_bot_slope_pmt1	
s_left_avg_slope_pmt1	
s_right_top_slope_pmt1	
s_right_mid_slope_pmt1	
s_right_bot_slope_pmt1	
s_right_avg_slope_pmt1	
s_lr_slope_pmt1	
s_left_area_pmt1	
s_right_area_pmt1	
s_lr_area_pmt1	
s_ref_left_area_pmt1	
s_ref_right_area_pmt1	
s_ref_lr_area_pmt1	
s_top_area_pmt1	
s_bot_area_pmt1	
s_bt_area_pmt1	
s_total_area_pmt1	
s_left_peri_pmt1	
s_right_peri_pmt1	
s_lr_peri_pmt1	
s_ref_left_peri_pmt1	

s_ref_right_peri_pmt1	
s_ref_lr_peri_pmt1	
s_total_peri_pmt1	
s_roundness_pmt1	
s_left_cyto_area_pmt1	
s_right_cyto_area_pmt1	
s_lr_cyto_area_pmt1	
s_cyto_area_pmt1	
s_nuc_area_pmt1	
s_cytonuc_area_pmt1	
s_diff_cytonuc_area_pmt1	
n_left_fwhm_pmt1	Repeat for Normalized Curves
n_right_fwhm_pmt1	
n_lr_fwhm_pmt1	
n_ref_left_fwhm_pmt1	
n_ref_right_fwhm_pmt1	
n_ref_lr_fwhm_pmt1	
n_fwhm_pmt1	
n_fw75m_pmt1	
n_fw25m_pmt1	
n_fw25_75m_pmt1	
n_left_top_slope_pmt1	
n_left_mid_slope_pmt1	
n_left_bot_slope_pmt1	
n_left_avg_slope_pmt1	
n_right_top_slope_pmt1	
n_right_mid_slope_pmt1	
n_right_bot_slope_pmt1	
n_right_avg_slope_pmt1	
n_lr_slope_pmt1	
n_left_area_pmt1	
n_right_area_pmt1	
n_lr_area_pmt1	
n_ref_left_area_pmt1	
n_ref_right_area_pmt1	
n_ref_lr_area_pmt1	
n_top_area_pmt1	
n_bot_area_pmt1	
n_bt_area_pmt1	

n_total_area_pmt1	
n_left_peri_pmt1	
n_right_peri_pmt1	
n_lr_peri_pmt1	
n_ref_left_peri_pmt1	
n_ref_right_peri_pmt1	
n_ref_lr_peri_pmt1	
n_total_peri_pmt1	
n_roundness_pmt1	
n_left_cyto_area_pmt1	Segmentation into thirds, outer third
n_right_cyto_area_pmt1	
n_lr_cyto_area_pmt1	
n_cyto_area_pmt1	
n_nuc_area_pmt1	Inner third
n_cytonuc_area_pmt1	
n_diff_cytonuc_area_pmt1	Area difference between cyto/nuc
g_sigma_pmt1	Gaussian fitted features
g_fwhm_pmt1	
g_center_pmt1	
g_peak_pmt1	
g_R2_pmt1	
g_left_area_pmt1	
g_right_area_pmt1	
g_lr_area_pmt1	
g_total_area_pmt1	
g_left_peri_pmt1	
g_right_peri_pmt1	
g_lr_peri_pmt1	
g_total_peri_pmt1	

Figure 7. Table of features for a single PMT channel. This list is repeated for each color. For a 2-color assay, each feature is also compared between PMTs (not included). Caption: R = raw, S = smoothed, N = normalized, G = Gaussian fitted curve, lr = left/right, bt = bottom/top, ref = feature is calculated using reference channel, 25 = 25% height from peak, 75% height from peak.

REFERENCES

Aborn, J.H. et al., 2005. A 768-lane microfabricated system for high-throughput DNA sequencing. *Lab on a chip*, 5(6), pp.669–674. Available at: http://www.ncbi.nlm.nih.gov/pubmed/15915260.

Abraham, R.T. & Weiss, A., 2004. Jurkat T cells and development of the T-cell receptor signalling paradigm. *Nature reviews. Immunology*, 4(4), pp.301–308. Available at: http://www.ncbi.nlm.nih.gov/pubmed/15057788.

Abraham, Y., Zhang, X. & Parker, C.N., 2014. Multiparametric Analysis of Screening Data: Growing Beyond the Single Dimension to Infinity and Beyond. *Journal of biomolecular screening*, 19(5), pp.628–639. Available at: http://www.ncbi.nlm.nih.gov/pubmed/24598104.

Anderson, D.E., Sharpe, A.H. & Hafler, D.A., 1999. The B7 – CD28 / CTLA-4 costimulatory pathways in autoimmune disease of the central nervous system. *Current opinion in immunology*, 1(11), pp.677–683.

Andorsky, D.J. et al., 2011. Programmed death ligand 1 is expressed by non-hodgkin lymphomas and inhibits the activity of tumor-associated T cells. *Clinical Cancer Research*, 17(13), pp.4232–4244. Available at: http://www.ncbi.nlm.nih.gov/pubmed/21540239.

Baine, I., Abe, B.T. & Macian, F., 2009. Regulation of T-cell tolerance by calcium/NFAT signaling. *Immunological Reviews*, 231, pp.225–240.

Beg, A.A. et al., 1993. Tumor necrosis factor and interleukin-1 lead to phosphorylation and loss of I kappa B alpha : a mechanism for NF-kappa B activation . Tumor Necrosis Factor and Interleukin-1 Lead to Phosphorylation and Loss of IKBoL : a Mechanism for NF-idB Activation. *Molecular and cellular biology*, 13(6), pp.3301–3310.

Blackman, M.A. et al., 1991. Altered antigen receptor signaling in anergic T cells from self-tolerant T-cell receptor a-chain transgenic mice. *Proceedings of the National Academy of Sciences if the United States of America*, 88(August), pp.6682–6686.

Bray, M.-A. et al., 2012. Workflow and metrics for image quality control in large-scale high-content screens. *Journal of biomolecular screening*, 17(2), pp.266–274. Available at: http://www.pubmedcentral.nih.gov/articlerender.fcgi?artid=3593271&tool=pmcentrez&rendertype=abstract [Accessed July 8, 2013].

Bray, M.-A. & Carpenter, A.E., 2004. Advanced Assay Development Guidelines for Image-Based High Content Screening and Analysis. *Assay guidance manual*. Available at: http://europepmc.org/abstract/MED/23469374 [Accessed September 25, 2013].

Brown, M. & Wittwer, C., 2000. Flow cytometry: principles and clinical applications in hematology. *Clinical chemistry*, 46(8 Pt 2), pp.1221–1229. Available at: http://www.ncbi.nlm.nih.gov/pubmed/10926916.

Carpenter, A.E. et al., 2006. CellProfiler: image analysis software for identifying and quantifying cell phenotypes. *Genome biology*, 7(10), p.R100.

Chen, Z., Zhang, L. & Chen, G., 2010. A spring-driven press device for hot embossing and thermal bonding of PMMA microfluidic chips. *Electrophoresis*, 31(15), pp.2512–2519. Available at: http://www.ncbi.nlm.nih.gov/pubmed/20665912 [Accessed July 25, 2012].

Cheung, M.C. et al., 2015. Image-based cell-resolved screening assays in flow. *Cytometry Part A*, 87(6), pp.541–548. Available at: http://www.ncbi.nlm.nih.gov/pubmed/25515084.

Chikuma, S. et al., 2009. PD-1-mediated suppression of IL-2 production induces CD8+ T cell anergy in vivo. *J Immunol*, 182(11), pp.6682–6689. Available at: http://www.jimmunol.org/content/182/11/6682.full.pdf.

Covert, M.W., 2011. Single-cell NF-κB dynamics reveal digital activation and analog information processing in cells. , 466(7303), pp.267–271.

Crisan, M. et al., 2008. A Perivascular Origin for Mesenchymal Stem Cells in Multiple Human Organs. *Cell Stem Cell*, 3(3), pp.301–313. Available at: http://www.ncbi.nlm.nih.gov/pubmed/18786417 [Accessed July 20, 2012].

Diaz-Quijada, G. a et al., 2007. Surface modification of thermoplastics--towards the plastic biochip for high throughput screening devices. *Lab on a chip*, 7(7), pp.856–862. Available at: http://www.ncbi.nlm.nih.gov/pubmed/17594004.

Diebold, E.D. et al., 2013. Digitally-synthesized beat frequency multiplexing for sub-millisecond fluorescence microscopy. *Optics in the Life Sciences (2013), paper JW3B.3*, 7(10), p.JW3B.3. Available at: http://www.opticsinfobase.org/abstract.cfm?URI=BODA-2013-JW3B.3%5Cnpapers3://publication/doi/10.1364/BODA.2013.JW3B.3.

Dong, H. et al., 2002. Tumor-associated B7-H1 promotes T-cell apoptosis: A potential mechanism of immune evasion. *Nature medicine*, 8(4), pp.793–800.

Dragiev, P., Nadon, R. & Makarenkov, V., 2011. Systematic error detection in experimental high-throughput screening. *BMC bioinformatics*, 12(1), p.25. Available at: http://www.scopus.com/inward/record.url?eid=2-s2.0-78651499200&partnerID=tZOtx3y1.

Edwards, B.S. & Sklar, L.A., 2015. Flow Cytometry: Impact on Early Drug Discovery. *Journal of biomolecular screening*, 20(6), pp.689–707. Available at: http://www.ncbi.nlm.nih.gov/pubmed/25805180.

Eglen, R. & Reisine, T., 2011. Primary cells and stem cells in drug discovery: emerging tools for high-throughput screening. *Assay and drug development technologies*, 9(2), pp.108–124. Available at: http://www.ncbi.nlm.nih.gov/pubmed/21186936.

Francisco, L.M., Sage, P.T. & Sharpe, A.H., 2010. The PD-1 pathway in tolerance and autoimmunity. *Immunological reviews*, 236, pp.219–242. Available at: http://www.pubmedcentral.nih.gov/articlerender.fcgi?artid=2919275&tool=pmcentrez&rendertype=abstract.

Freeley, M. et al., 2010. A high-content analysis toolbox permits dissection of diverse signaling pathways for T lymphocyte polarization. *Journal of biomolecular screening*, 15(5), pp.541–555. Available at: http://www.ncbi.nlm.nih.gov/pubmed/20460253 [Accessed August 29, 2013].

Gerondakis, S. & Siebenlist, U., 2010. Roles of the NF-kB Pathway in Lymphocyte Development and Function. *Cold Spring Harbor Perspectives in Biology*, (2), pp.1–29.

Gilmore, T.D. & Gerondakis, S., 2011. The c-Rel Transcription Factor in Development and Disease. *Genes and Cancer*, 2(7), pp.695–711.

Giuliano, K. a, Haskins, J.R. & Taylor, D.L., 2003. Advances in high content screening for drug discovery. *Assay and drug development technologies*, 1(4), pp.565–577.

Goda, K., Tsia, K.K. & Jalali, B., 2009. Serial time-encoded amplified imaging for real-time observation of fast dynamic phenomena. *Nature*, 458(7242), pp.1145–1149. Available at: http://www.nature.com/doifinder/10.1038/nature07980.

Godin, J. et al., 2008. Microfluidics and photonics for Bio-System-on-a-Chip: a review of advancements in technology towards a microfluidic flow cytometry chip. *Journal of biophotonics*, 1(5), pp.355–376. Available at: http://www.pubmedcentral.nih.gov/articlerender.fcgi?artid=2746115&tool=pmcentrez&rendertype=abstract [Accessed March 2, 2012].

Gorthi, S.S., Schaak, D. & Schonbrun, E., 2013. Fluorescence imaging of flowing cells using a temporally coded excitation. *Optics express*, 21(4), pp.5164–5170. Available at: http://www.ncbi.nlm.nih.gov/pubmed/23482050.

Grenga, I. et al., 2016. A fully human IgG1 anti-PD-L1 MAb in an in vitro assay enhances antigen-speci fi c T-cell responses. *Clinical and translational immunology*, 5(5), pp.e83. Available at: http://dx.doi.org/10.1038/cti.2016.27.

Hamid, O. et al., 2013. Safety and tumor responses with lambrolizumab (anti-PD-1) in melanoma. *The New England journal of medicine*, 369(2), pp.134–144. Available at: http://www.ncbi.nlm.nih.gov/pubmed/23724846 [Accessed July 9, 2014].

Han, Y. et al., 2016. Review: imaging technologies for flow cytometry. *Lab on a Chip*, 16, pp.4639–4647. Available at: http://dx.doi.org/10.1039/C6LC01063F%5Cnhttp://xlink.rsc.org/?DOI=C6LC01063F.

Hapter, C., Freeman, G.J. & Sharpe, A.H., 2003. PD-1 : PD-1 Ligand Pathway.

V. Hessel, A., Renken, J.C. Schouten, J.I.Y., 2009. *Micro Process Engineering, Vol. 1*, Available at: http://cdn.intechweb.org/pdfs/28981.pdf.

Huang, A.C. et al., 2017. T-cell invigoration to tumour burden ratio associated with anti-PD-1 response. *Nature*, 545, pp.60–65. Available at: http://dx.doi.org/10.1038/nature22079.

Huang, X. et al., 2017. Stable gene transfer and expression in human primary T cells by the Sleeping Beauty transposon system. *Blood*, 107(2), pp.483–492.

Hughes, J.P. et al., 2011. Principles of early drug discovery. *British journal of pharmacology*, 162(6), pp.1239–1249. Available at: http://www.pubmedcentral.nih.gov/articlerender.fcgi?artid=3058157&tool=pmcentrez&rendertype=abstract.

Ilani, T. et al., 2007. Immune synapse formation requires ZAP-70 recruitment by ezrin and CD43 removal by moesin. *The Journal of cell biology*, 179(4), pp.733–746. Available at: http://www.pubmedcentral.nih.gov/articlerender.fcgi?artid=2080902&tool=pmcentrez&rendertype=abstract.

Intlekofer, A.M. & Thompson, C.B., 2013. At the bench: preclinical rationale for CTLA-4 and PD-1 blockade as cancer immunotherapy. *Journal of leukocyte biology*, 94(1), pp.25–39. Available at:

http://www.pubmedcentral.nih.gov/articlerender.fcgi?artid=3685017&tool=pmcentrez&rendertype=abstract [Accessed November 8, 2014].

Iwai, Y. et al., 2002. Involvement of PD-L1 on tumor cells in the escape from host immune system and tumor immunotherapy by PD-L1 blockade. *Proceedings of the National Academy of Sciences of the United States of America*, 99(19), pp.12293–12297. Available at: http://www.pubmedcentral.nih.gov/articlerender.fcgi?artid=129438&tool=pmcentrez&rendertype=abstract.

Kammer, G.M., Smith, J. a & Mitchell, R., 1983. Capping of human T cell specific determinants: kinetics of capping and receptor re-expression and regulation by the cytoskeleton. *Journal of immunology*, 130(1), pp.38–44. Available at: http://www.ncbi.nlm.nih.gov/pubmed/6600189.

Karwacz, K. et al., 2011. PD-L1 co-stimulation contributes to ligand-induced T cell receptor down-modulation on CD8 + T cells. *EMBO Molecular Medicine*, 3(10), pp.581–592.

King, C.C. et al., 2011. The rate of NF-κB nuclear translocation is regulated by PKA and A kinase interacting protein 1. *PloS one*, 6(4), p.e18713. Available at: http://www.pubmedcentral.nih.gov/articlerender.fcgi?artid=3083391&tool=pmcentrez&rendertype=abstract [Accessed August 24, 2014].

Kozak, K. et al., 2009. Data Mining Techniques in High Content Screening: A Survey. *Journal of Computer Science & Systems Biology*, 2(4), pp.219–239. Available at: http://www.omicsonline.com/ArchiveJCSB/2009/August/03/JCSB2.219.php [Accessed October 30, 2012].

Kümmel, A. et al., 2011. Comparison of multivariate data analysis strategies for high-content screening. *Journal of biomolecular screening*, 16(3), pp.338–47. Available at: http://www.ncbi.nlm.nih.gov/pubmed/21335595.

Leitner, J. et al., 2011. The effects of Cyclosporine A and azathioprine on human T cells activated by different costimulatory signals. *Immunology Letters*, 140(1–2), pp.74–80. Available at: http://dx.doi.org/10.1016/j.imlet.2011.06.010.

Longo, D.M. et al., 2012. Single-cell network profiling of peripheral blood mononuclear cells from healthy donors reveals age- and race-associated differences in immune signaling pathway activation. *Journal of immunology*, 188(4), pp.1717–1725. Available at: http://www.jimmunol.org/cgi/doi/10.4049/jimmunol.1102514 [Accessed January 24, 2014].

Lupino, E., Ramondetti, C. & Piccinini, M., 2012. IκB kinase β is required for activation of NF-κB and AP-1 in CD3/CD28-stimulated primary CD4(+) T cells. *Journal of immunology*, 188(6), pp.2545–2555. Available at: http://www.ncbi.nlm.nih.gov/pubmed/22331067.

Maguire, O. et al., 2013. Nuclear translocation of nuclear factor of activated T cells (NFAT) as a quantitative pharmacodynamic parameter for tacrolimus. *Cytometry. Part A*, 83(12), pp.1096–1104. Available at: http://www.ncbi.nlm.nih.gov/pubmed/24136923 [Accessed September 17, 2014].

Marincola, F.M. et al., 2003. Tumors as elusive targets of T-cell-based active immunotherapy. *Trends in Immunology*, 24(6), pp.334–341. Available at: http://linkinghub.elsevier.com/retrieve/pii/S1471490603001169 [Accessed February 4, 2013].

Mathur, a. et al., 2009. Characterisation of PMMA microfluidic channels and devices fabricated by hot embossing and sealed by direct bonding. *Current Applied Physics*, 9(6), pp.1199–1202. Available at: http://linkinghub.elsevier.com/retrieve/pii/S1567173909000273 [Accessed November 29, 2011].

Mckenna, B.K. et al., 2009. 384-Channel Parallel Microfluidic Cytometer for Rare-Cell Screening. *Lab on a chip*, 9(2), pp.305–310. Available at: http://www.ncbi.nlm.nih.gov/pubmed/19107289 [Accessed May 22, 2014].

McKenna, B.K. et al., 2011. A parallel microfluidic flow cytometer for high-content screening - Supplemental. *Nature Methods*, 8(5), pp.401–403.

Millipore, 2017. ImageStream®X Mark II - FAQ. Available at: http://www.emdmillipore.com/US/en/life-science-research/cell-analysis/amnis-imaging-flow-cytometers/imagestreamx-Mark-ii-imaging-flow-cytometer/VaSb.qB.QokAAAFLzRop.zHe,nav.

Molitor, J. a et al., 1990. NF-kappa B: a family of inducible and differentially expressed enhancer-binding proteins in human T cells. *Proceedings of the National Academy of Sciences of the United States of America*, 87(24), pp.10028–10032. Available at: http://www.pubmedcentral.nih.gov/articlerender.fcgi?artid=55308&tool=pmcentrez&rendertype=abstract.

Murphy, L.L.S. & Hughes, C.C.W., 2002. Endothelial Cells Stimulate T Cell NFAT Nuclear Translocation in the Presence of Cyclosporin A: Involvement of the wnt/Glycogen Synthase Kinase-3 ᴺᴸ Pathway 1. *Journal of Immunology*, 169(28),

pp.3717–3725.

Narasimhan, J. & Papautsky, I., 2004. Polymer embossing tools for rapid prototyping of plastic microfluidic devices. *Journal of Micromechanics and Microengineering*, 14(1), pp.96–103. Available at: http://stacks.iop.org/0960-1317/14/i=1/a=013?key=crossref.7bfc7b6dc2a01dca4f98554f270c1eb6 [Accessed August 3, 2011].

Nardozzi, J.D., Lott, K. & Cingolani, G., 2010. Phosphorylation meets nuclear import: a review. *Cell communication and signaling*, 8(1), p.32. Available at: http://www.pubmedcentral.nih.gov/articlerender.fcgi?artid=3022542&tool=pmcentrez&rendertype=abstract.

Ng, A.Y.J. et al., 2010. A cell profiling framework for modeling drug responses from HCS imaging. *Journal of biomolecular screening*, 15(7), pp.858–868. Available at: http://jbx.sagepub.com/cgi/doi/10.1177/1087057110372256 [Accessed June 20, 2013].

Nicholson, J.K., Hubbard, M. & Jones, B.M., 1996. Use of CD45 fluorescence and side-scatter characteristics for gating lymphocytes when using the whole blood lysis procedure and flow cytometry. *Cytometry*, 26(1), pp.16–21. Available at: http://www.ncbi.nlm.nih.gov/pubmed/8809476.

Nirschl, C.J. & Drake, C.G., 2013. Molecular Pathways: Co-Expression of Immune Checkpoint Molecules: Signaling Pathways and Implications for Cancer Immunotherapy. *Clinical cancer research*, 19(18), pp.4917–4924 . Available at: http://www.ncbi.nlm.nih.gov/pubmed/23868869 [Accessed August 25, 2013].

Okazaki, T. et al., 2013. A rheostat for immune responses : the unique properties of PD-1 and their advantages for clinical application. *Nature Immunology*, 14(12), pp.1212–1218. Available at: http://dx.doi.org/10.1038/ni.2762.

Okazaki, T. & Honjo, T., 2007. PD-1 and PD-1 ligands: from discovery to clinical application. *International immunology*, 19(7), pp.813–824. Available at: http://www.ncbi.nlm.nih.gov/pubmed/17606980 [Accessed October 2, 2014].

Parry, R. V et al., 2005. CTLA-4 and PD-1 Receptors Inhibit T-Cell Activation by Distinct Mechanisms. *Molecular and Cellular Biology*, 25(21), p.9543.

Peng, H.C., Long, F.H. & Ding, C., 2005. Feature selection based on mutual information: Criteria of Max-Dependency, Max-Relevance, and Min-Redundancy. *IEEE Transactions on Pattern Analysis and Machine Intelligence*, 27(8), pp.1226–1238.

Podojil, J.R. & Miller, S.D., 2009. Molecular mechanisms of T-cell receptor and costimulatory molecule ligation/blockade in autoimmune disease therapy. *Immunological reviews*, 229(1), pp.337–355. Available at: http://www.pubmedcentral.nih.gov/articlerender.fcgi?artid=2845642&tool=pmcentrez&rendertype=abstract.

Poltorak, M. et al., 2013. TCR activation kinetics and feedback regulation in primary human T cells. *Cell communication and signaling*, 11(1), p.4. Available at: http://www.pubmedcentral.nih.gov/articlerender.fcgi?artid=3842781&tool=pmcentrez&rendertype=abstract [Accessed September 17, 2014].

Powles, T. et al., 2014. MPDL3280A (anti-PD-L1) treatment leads to clinical activity in metastatic bladder cancer. *Nature*, 515(7528), pp.558–562. Available at: http://www.nature.com/doifinder/10.1038/nature13904%5Cnhttp://www.ncbi.nlm.nih.gov/pubmed/25428503.

Prieto, P. a et al., 2012. CTLA-4 blockade with ipilimumab: long-term follow-up of 177 patients with metastatic melanoma. *Clinical cancer research*, 18(7), pp.2039–2047. Available at: http://www.pubmedcentral.nih.gov/articlerender.fcgi?artid=3319861&tool=pmcentrez&rendertype=abstract [Accessed September 13, 2013].

Richardson, G.M., Lannigan, J. & Macara, I.G., 2015. Does FACS perturb gene expression? *Cytometry Part A*, 87(2), pp.166–175. Available at: http://www.ncbi.nlm.nih.gov/pubmed/25598345 [Accessed January 22, 2015].

Riley, J.L., 2009. PD-1 signaling in primary T cells. *Immunological Reviews*, 229(1), pp.114–125.

Riley, R.S., Idowu, M., *Principles and Applications of Flow Cytometry*. Hematology/oncology lymph node seminar for Medical II students. Department of Pathology, Medical College of Virginia/VCU Health Systems Virginia, Virginia Commonwealth University: Richmond, VA. Available at: http://www.flowlab-childrens-harvard.com/yahoo_site_admin/assets/docs/PRINCIPLESANDAPPLICATION.29464931.pdf

Robert, C. et al., 2014. Anti-programmed-death-receptor-1 treatment with pembrolizumab in ipilimumab-refractory advanced melanoma: a randomised dose-comparison cohort of a phase 1 trial. *Lancet*, 384, pp.1109–1117. Available at: http://www.ncbi.nlm.nih.gov/pubmed/25034862 [Accessed September 3, 2014].

Roederer, M., 2001. Spectral compensation for flow cytometry: visualization artifacts, limitations, and caveats. *Cytometry*, 45(3), pp.194–205. Available at: http://www.ncbi.nlm.nih.gov/pubmed/11746088.

Schonbrun, E., Gorthi, S.S. & Schaak, D., 2012. Microfabricated multiple field of view imaging flow cytometry. *Lab on a chip*, 12(2), pp.268–273. Available at: http://www.ncbi.nlm.nih.gov/pubmed/22037643.

Schreiner, G.F. & Unanue, E.R., 2011. Opinions : Capping and the Lymphocyte : Models for Membrane Reorganization. *Journal of Immunology,* 119(5), pp.1549–1551

Schwartz, R.H., 2003. T Cell Anergy. *Annual Review of Immunology*, (21), pp.305–334.

Shapiro, H.M., 2003. *Practical flow cytometry*, Available at: http://books.google.com/books?hl=en&lr=&id=JhSyimPKuJwC&oi=fnd&pg=PR7&dq=PRACTICAL+FLOW+cytometry&ots=OPDVxPVPMF&sig=ovuTqS5cRjypdhFlm6R8eyMk7yc.

Shariff, A. et al., 2010. Automated image analysis for high-content screening and analysis. *Journal of biomolecular screening*, 15(7), pp.726–734. Available at: http://www.ncbi.nlm.nih.gov/pubmed/20488979 [Accessed June 4, 2013].

Shen, X.-J., Pan, L.-W. & Lin, L., 2002. Microplastic embossing process: experimental and theoretical characterizations. *Sensors and Actuators A: Physical*, 97–98, pp.428–433. Available at: http://linkinghub.elsevier.com/retrieve/pii/S0924424702000298.

Singh, S., Carpenter, A.E. & Genovesio, A., 2014. Increasing the Content of High-Content Screening: An Overview. *Journal of biomolecular screening*, 19(5), pp.640–650. Available at: http://www.pubmedcentral.nih.gov/articlerender.fcgi?artid=4230961&tool=pmcentrez&rendertype=abstract.

Skora, A.D. et al., 2015. PD-1 Blockade in Tumors with Mismatch-Repair Deficiency. *New England Journal of Medicine*, 372, pp.2509–2520.

Smith-Garvin, J.E., 2009. T cell activation. *Annual review of immunology*, 27, pp.591–619. Available at: http://www.ncbi.nlm.nih.gov/pmc/articles/PMC2740335/ [Accessed September 13, 2013].

Srivastava, R., Burbach, B.J. & Shimizu, Y., 2010. NF-kappaB activation in T cells requires discrete control of IkappaB kinase alpha/beta (IKKalpha/beta)

phosphorylation and IKKgamma ubiquitination by the ADAP adapter protein. *The Journal of biological chemistry*, 285(15), pp.11100–11105. Available at: http://www.pubmedcentral.nih.gov/articlerender.fcgi?artid=2856986&tool=pmcentrez&rendertype=abstract [Accessed February 24, 2015].

Starkuviene, V. & Pepperkok, R., 2007. The potential of high-content high-throughput microscopy in drug discovery. *British journal of pharmacology*, 152(1), pp.62–71. Available at: http://www.pubmedcentral.nih.gov/articlerender.fcgi?artid=1978277&tool=pmcentrez&rendertype=abstract.

Suni, M. a, Maino, V.C. & Maecker, H.T., 2005. Ex vivo analysis of T-cell function. *Current opinion in immunology*, 17(4), pp.434–440. Available at: http://www.ncbi.nlm.nih.gov/pubmed/15950444 [Accessed August 26, 2011].

Tomkowicz, B. et al., 2015. TIM-3 suppresses anti-CD3/CD28-induced TCR activation and IL-2 expression through the NFAT signaling pathway. *PLoS One*, 10(10), pp.1–21.

Torgerson, T.R. et al., 1998. Regulation of NF-κB, AP-1, NFAT, and STAT1 Nuclear Import in T Lymphocytes by Noninvasive Delivery of Peptide Carrying the Nuclear Localization Sequence of NF-kappa B p50. *Journal of Immunology*, 161(11), pp.6084–6092. Available at: http://www.ncbi.nlm.nih.gov/pubmed/9834092.

Tsao, C.-W.W. & DeVoe, D.L., 2008. Bonding of thermoplastic polymer microfluidics. *Microfluidics and Nanofluidics*, 6(1), pp.1–16. Available at: http://link.springer.com/10.1007/s10404-008-0361-x [Accessed September 24, 2013].

Vittinghoff, E. & Mcculloch, C.E., 2007. Original Contribution Relaxing the Rule of Ten Events per Variable in Logistic and Cox Regression. *American Journal of Epidemiology*, 165(6), pp.710–718.

Wang, S.S. & Ehrlich, D.J., 2017. Image-Based Phenotypic Screening with Human Primary T Cells Using One- Dimensional Imaging Cytometry with Self- Tuning Statistical-Gating Algorithms. *SLAS Discovery: Advancing Life Sciences R&D*, 22(8), pp.985–994.

Wang, Z.K. et al., 2011. Improving surface smoothness of laser-fabricated microchannels for microfluidic application. *Journal of Micromechanics and Microengineering*, 21(9), p.95008. Available at: http://stacks.iop.org/0960-1317/21/i=9/a=095008?key=crossref.5820d5def88ccab1e407dc224ee9e782.

Wong, R.M. et al., 2007. Programmed death-1 blockade enhances expansion and functional capacity of human melanoma antigen-specific CTLs. *International Immunology,* 19(10), pp.1223–1234.

Yamanaka, Y.J., Gierahn, T.M. & Love, J.C., 2013. The dynamic lives of T cells : new approaches and themes. *Trends in Immunology*, 34(2), pp.59–66. Available at: http://dx.doi.org/10.1016/j.it.2012.10.006.

Yi, C. et al., 2006. Microfluidics technology for manipulation and analysis of biological cells. *Analytical Chimica Acta*, 560, pp.1–23.

Zanella, F., Lorens, J.B. & Link, W., 2010. High content screening: seeing is believing. *Trends in biotechnology*, 28(5), pp.237–245. Available at: http://www.ncbi.nlm.nih.gov/pubmed/20346526 [Accessed April 30, 2014].

Zhang, J.-H., Chung, T.D.Y.Y. & Oldenburg, K.R., 1999. A Simple Statistical Parameter for Use in Evaluation and Validation of High Throughput Screening Assays. *Journal of Biomolecular Screening*, 4(2), pp.67–73. Available at: http://jbx.sagepub.com/content/4/2/67.abstract [Accessed January 21, 2014].

Zhang, X.D., 2007. A pair of new statistical parameters for quality control in RNA interference high-throughput screening assays. *Genomics*, 89(4), pp.552–561.

Zuba-Surma, E.K. et al., 2007. The ImageStream System: a key step to a new era in imaging. *Folia histochemica et cytobiologica*, 45(4), pp.279–290. Available at: http://www.ncbi.nlm.nih.gov/pubmed/18165167.

CURRICULUM VITAE